INFORMATION TO USERS

This manuscript has been reproduced from the microfilm master. UMI films the text directly from the original or copy submitted. Thus, some thesis and dissertation copies are in typewriter face, while others may be from any type of computer printer.

The quality of this reproduction is dependent upon the quality of the copy submitted. Broken or indistinct print, colored or poor quality illustrations and photographs, print bleedthrough, substandard margins, and improper alignment can adversely affect reproduction.

In the unlikely event that the author did not send UMI a complete manuscript and there are missing pages, these will be noted. Also, if unauthorized copyright material had to be removed, a note will indicate the deletion.

Oversize materials (e.g., maps, drawings, charts) are reproduced by sectioning the original, beginning at the upper left-hand corner and continuing from left to right in equal sections with small overlaps. Each original is also photographed in one exposure and is included in reduced form at the back of the book.

Photographs included in the original manuscript have been reproduced xerographically in this copy. Higher quality 6" x 9" black and white photographic prints are available for any photographs or illustrations appearing in this copy for an additional charge. Contact UMI directly to order.

UMI

A Bell & Howell Information Company
300 North Zeeb Road, Ann Arbor MI 48106-1346 USA
313/761-4700 800/521-0600

μSR Studies of Crippled HTSC Cuprates: Charge and Spin Inhomogeneities in the CuO_2 Plane

Benjamin E. Nachumi

Submitted in partial fulfillment of the
requirements for the degree
of Doctor of Philosophy
in the Graduate School of Arts and Sciences.

COLUMBIA UNIVERSITY

1999

Abstract

μSR Studies of Crippled HTSC Cuprates: Charge and Spin Inhomogeneities in the CuO_2 Plane

Benjamin E. Nachumi

I present muon spin rotation (μSR) measurements of the zero-field magnetic order, and of the superconducting magnetic response, in $La_{2-x}(Sr/Ba)_xCuO_4$ and $YBa_2Cu_3O_{6.63}$ cuprates for which the superconducting transition temperature T_C has been suppressed by the substitution of interplanar Nd or planar Zn. A stripe-like, modulated magnetic order occurs in the $La_{1.6-x}Nd_{0.4}(Ba/Sr)_xCuO_4$ material, and I explore its magnetic properties (ordered moment size, transition temperature) as well as its superconducting response in μSR. The latter measurements imply the microscopic coexistence of superconductivity and magnetism in this magnetic phase. Zn substitution in the CuO_2 plane markedly suppresses T_C in $La_{2-x}Sr_xCuO_4$ and $YBa_2Cu_3O_{6+x}$ systems. Here I discuss the T_C reduction in concert with the reduction in the superconducting carrier density/effective mass ratio n_s/m^*, which puts extra constraints on pair-breaking and localization models.

Contents

List of Figures

And you may ask yourself,
My god! What have I done?
–Talking Heads,
Once in a Lifetime

Chapter 1

Introduction

1.1 General Background of the Hole-Doped Cuprates

The initial discovery of the first cuprate high-temperature (high-T_C) superconductor[1] seems to have been an inspired hunch on the parts of J. G. Bednorz and K. A. Müller. Eleven years after their seminal discovery, the pairing interaction of the cuprates, and the stability of their superconducting (SC) phases, remain a mystery—though perhaps not as much of a mystery as they were eleven years ago. The diversity of materials and their various normal-state and superconducting properties have become the subject of an astounding number of experiments and theories. Part of the experimmental effort has been directed at engineering new compounds with still higher T_C's; the remainder has been devoted to understanding the properties of the extant materials.

The cuprate high-T_C materials are a family of copper-oxide-based, inorganic compounds with extremely high superconducting transition temperatures (T_C's). Most elemental superconductors have maximal T_C's in the range of 1-5 K, and prior to the 1986 discovery of the first cuprate material, the highest T_C of any known material stood at 22.3K for Nb_3Ge [2]. In 1986, Bednorz and Müller discovered superconductivity in the first series of the cuprates, $La_{2-x}Ba_xCuO_4$, at 35K. The crystal structure of this cuprate is shown in Fig. 1.1. Layered CuO_2 planes are separated by octahe-

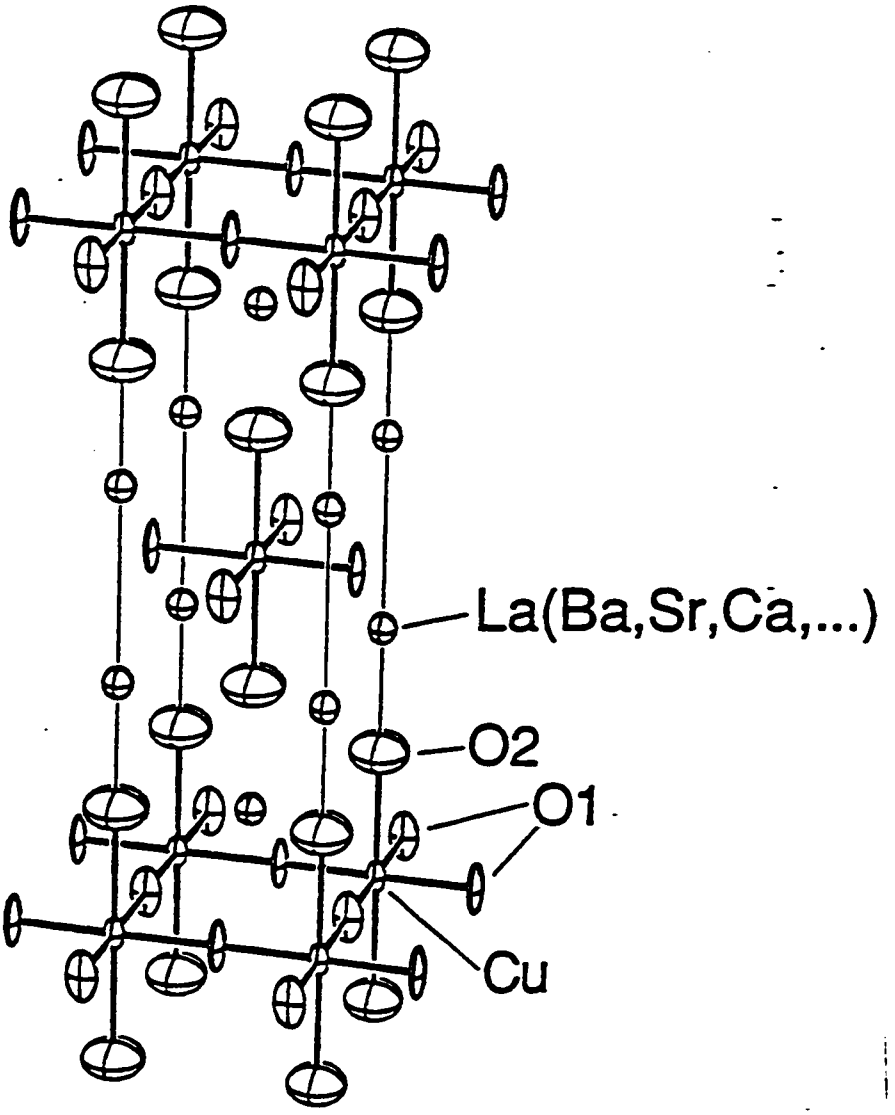

Figure 1.1 Unit cell of the "214" cuprate $La_{2-x}(Ba/Sr)_xCuO_4$ from ref. [3].

drally coordinated oxygen anions and (La/Ba) cations, in the perovskite structure. Soon thereafter, Sr substitution at the La site raised the T_C to 40K.

Subsequently, intensive experimental effort has uncovered several other cuprate series. All of these materials share the CuO_2 plane as a structural element; they differ in the number of planes per unit cell, and the interplanar constituents. $YBa_2Cu_3O_{6+x}$ was the first series discovered to become superconducting (for some doping levels) above the temperature of liquid N_2. The structure of this material is shown in Fig. 1.2. In addition to the CuO_2 planes, this compound contains CuO chains. The current record-holder for the highest T_C (164K) is the $HgBa_2Ca_{n-1}Cu_nO_{2n+2+x}$ series with

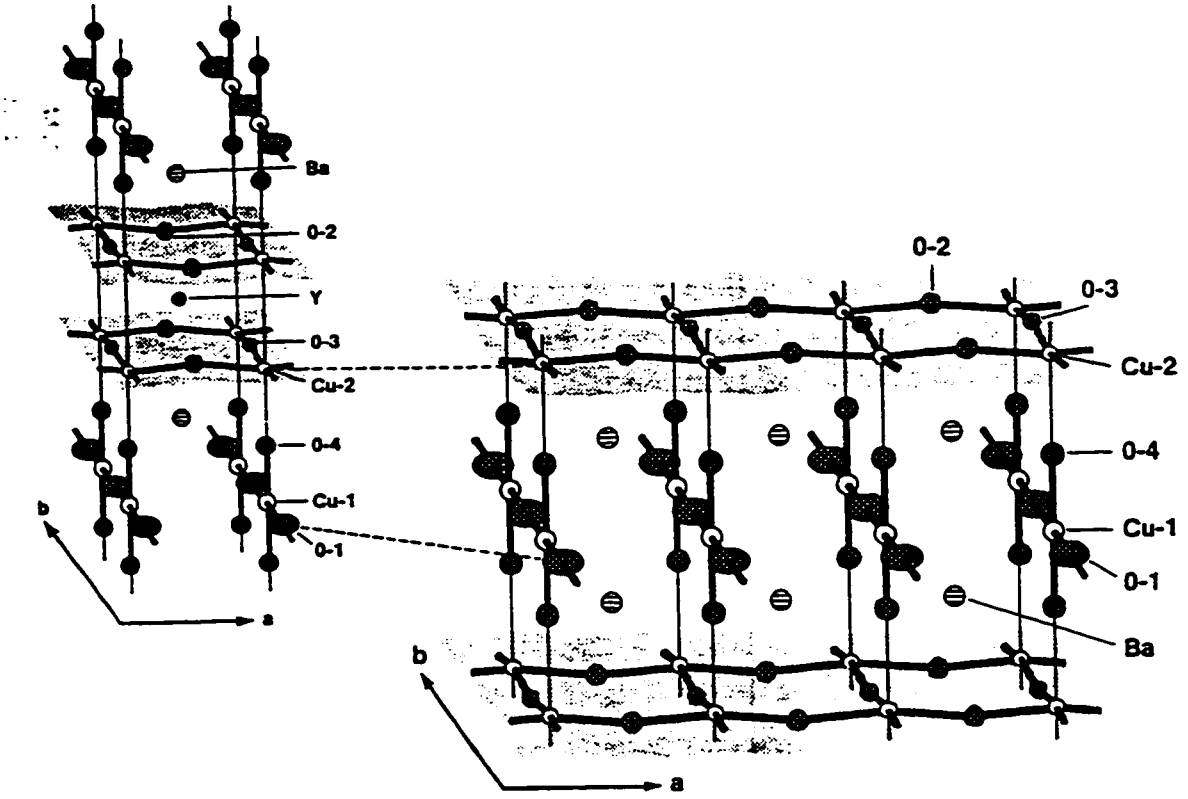

Figure 1.2 Unit cell of the "123" cuprate $YBa_2Cu_3O_{6+x}$
from ref. [3].

n=3, under high pressure.

The HTSC cuprates are derived from the antiferromagnetic (AF) cuprates. In these materials, the Cu-3d band is only half-filled, but the materials are insulating because the band is split by strong Coulomb repulsion between the electrons. The localized spins become ordered via the 180-degree Cu-O-Cu exchange interaction; the magnetic order is well-described by a quasi-2-dimensional Heisenberg model.

The AF materials are dopable by interplanar substitution of the cation, or by variation of the oxygen content. The doping process in almost all cases oxidizes

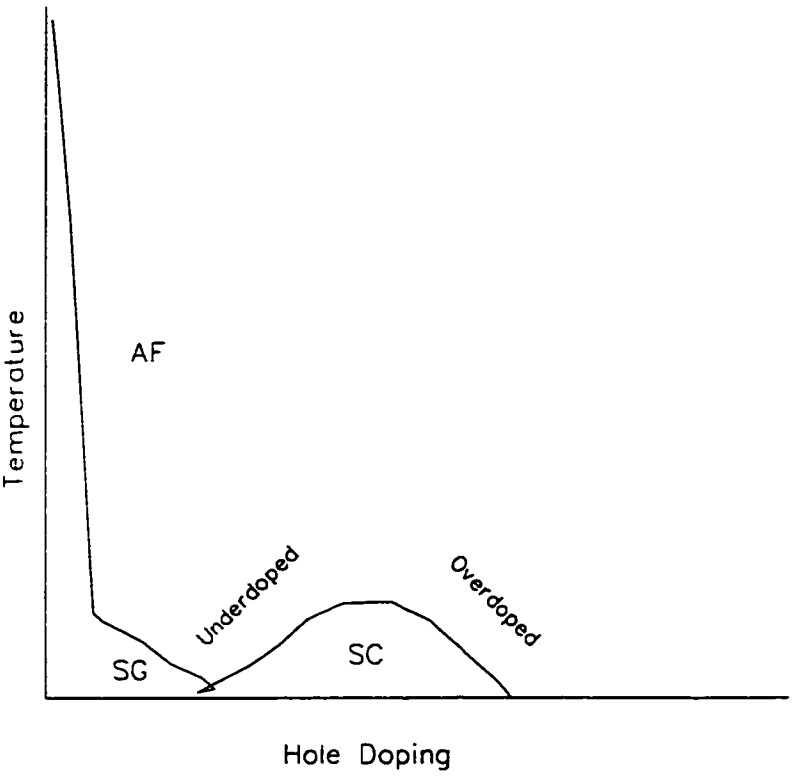

Figure 1.3 Electronic phase diagram as a function of temperature and doping x for a "generic cuprate."

the CuO_2 plane: the vast majority of the cuprate family are hole-doped. Hole-doped HTSC's share a somewhat generic phase diagram as a function of temperature and doping x. When holes are doped into the CuO_2 plane, the AF state is rapidly destroyed. The reduction in T_N is much faster than one would expect from simple dilution of the spins, suggesting that frustration effects are important. At a lower critical doping level, the ground state becomes SC. With increasing x, T_C of the SC state rises to $T_{C;Max}$ saturates, and falls again. Call the dopant concentration at which T_C for a given series attains its highest value x_{Max}. Where $x < x_{Max}$ the system is "underdoped"; where $x > x_{Max}$ the system is "overdoped." The generic phase diagram for the HTSC cuprates is sketched in Fig. 1.3. It is widely believed that the generic superconducting properties of the cuprates, as well as their AF properties, originate in the CuO_2 plane.

1.2 What makes these materials so interesting?

1.2.1 Brief Review of BCS Theory

The famous BCS theory of superconductivity, and its subsequent variations, admirably predict the behaviors of what are nowadays referred to as "classical" superconductors—well-understood elemental superconductors like Al and Pb, as well as some more complicated alloys. BCS theory proceeds from a Fermi liquid with attractive 2-point interactions. The starting Hamiltonian has the general structure [4]

$$\hat{H} = \int d\vec{r}\{-\hbar^2/2m\hat{\psi}^\dagger(\vec{r})\nabla^2\hat{\psi}(\vec{r}) + \frac{1}{2}\int d\vec{r}'\hat{\psi}^\dagger(\vec{r})\hat{\psi}^\dagger(\vec{r}')V(\vec{r}-\vec{r}')\hat{\psi}(\vec{r}')\hat{\psi}(\vec{r})\},$$

where $\hat{\psi}^\dagger, \hat{\psi}$ are the fermion creation and annihilation operators. Cooper [5] showed that a net attractive interaction between Fermions creates a pairing instability for electrons near the Fermi surface when the characteristic frequency of the interaction,

$\omega_B \ll E_F$, the Fermi energy. The full BCS solution predicts that below T_C, this instability is self-supporting–all of the electrons within ω_B of E_F scatter around the Fermi surface as correlated "Cooper pairs."

The BCS method is to assume that the ground state of the superconductor is such that the electrons are paired. In momentum space, the Hamiltonian then becomes

$$\hat{H} = \hat{H}_{Kinetic} + \sum_{\vec{k}\vec{k}'} V_{\vec{k}\vec{k}'} \hat{a}^{\dagger}_{\vec{k}\uparrow} \hat{a}^{\dagger}_{-\vec{k}\downarrow} \hat{a}_{\vec{k}'\downarrow} \hat{a}_{-\vec{k}'\uparrow}.$$

BCS then make use of a mean-field approximation, in which the product of four field operators is replaced by a single-particle operator (two field operators) multiplied by an expectation value–the "pairing field" $\Delta = \langle \hat{a}_{\vec{k}\downarrow} \hat{a}_{-\vec{k}\uparrow} \rangle$[4, 6]. By assuming an interaction in $\vec{K}$-space $V_{\vec{k}\vec{k}'} = g$, a constant, for energies $\leq \omega_B$, and zero outside of this range. BCS theory yields a self-consistent equation for the new field Δ, which may be identified with the superconducting condensate below T_C.

Note that the mean-field BCS Hamiltonian does not conserve particle number: the condensate tends to mix states with different numbers of electrons, *i. e.* scattering from the condensate will mix particles and holes[7]. Because of this phenomenon, an energy gap develops at the Fermi surface in the Fermion density of states[4, 8]:

$$E_{\vec{k}} \rightarrow \sqrt{E^2_{\vec{k}} + |\Delta|^2}.$$

The new quasiparticles are excitations of the condensate–members of broken Cooper pairs which, depending on their energy, have either a hole-like or electron-like character. The typical temperature scale for superconductivity is therefore Δ; the BCS value for Δ is $0.88 k_B T_C$, where k_B is Boltzmann's constant. The BCS $T_C = 1.14 \hbar\omega_B \times \exp(-1/N(E_F)g)$, where $N(E_F)$ is the density of states at the Fermi

level[4. 8].

The fundamental lengthscales of superconductivity are the *penetration depth* and the *coherence length.* I now briefly discuss the significance and origins of these lengthscales. Due to the gap in the excitation spectrum of the superconducting state, the wavefunction becomes "rigid"[9, 10] with respect to perturbation by weak magnetic fields. When this condition is combined with Maxwell's equations and a quantum-mechanical operator for the electron current, one finds that the superconductor tends to expell a weak applied magnetic field (the Meissner effect) over a penetration depth, or screening length λ. In pure materials with large mean-free paths and very short coherence lengths, λ is just the "London penetration depth" $\lambda_L = \sqrt{m^* c^2/4\pi n_s q^2}$, where n_s is the density of superconducting carriers, m^* is the effective mass, and q is the charge of the carriers (this value is derived in Chapter 3).

When the density of states is approximately constant[8] (a quasi-two-dimensional situation [4] which occurs, e. g. when $\omega_B \ll E_F$) the attractive interaction between two fermions naively leads to a bound state wavefunction (Cooper pair) with a characteristic size $\sim \xi$. The correlation lengthscale persists in the full-blown BCS calculation of the superconducting response to applied electric and magnetic fields. This correlation length ξ enters the theory as the length over which the condensate reponds coherently to the fields. If the fields vary on a shorter lengthscale, then the composite particles of the condensate begin to respond to the field independently of one another.

In a very qualitative sense, the ratio ξ/λ defines the "granularity" of the superconducting state. In an applied magnetic field, when $\xi > \lambda$ (in a "type I superconductor"), the superconducting wavefunction Δ tends to a constant value far inside

the superconductor (so long as the energy required to expell the field does not exceed the condensation energy). On the other hand, when $\xi < \lambda$ (in a "type II superconductor"), the magnetic field penetrates in quantized units of flux known as "fluxoids" or "flux tubes," each of which is associated with a quantum of flux $\phi_0 = hc/2e$. This qualitative distinction results from the change in sign of the surface energy of a normal-superconducting interface when $\xi/\lambda \sim 1$[11].

The general reason for the flux intrusion is that, for $\lambda_L/\xi > 1$, the surface energy of a normal-superconducting interface becomes negative. This negative surface energy must be balanced against the kinetic energy of the screening currents. At fields higher than a lower critical field H_{C1}, the surface-energy term wins, and the flux begins to penetrate. The quantization of the fluxoids results from the necessity that the superconducting wavefunction be single-valued. The phase of the superconducting wavefunction may only change by integral multiples of 2π around any normal hole which threads the superconductor; the total phase is proportional to the magnetic flux through the hole. One might think of a type-I superconductor as a big, many-body Cooper-pair, all of which prefers to be in the same phase; and a type-II superconductor as a system of overlapping Cooper pairs whose phase may vary regularly from one to the next.

1.2.2 BCS-Like Theories

Subsequent theories have sought to modify the BCS calculation for more general interactions which are time-dependent and which may depend on the angle between $\vec{k}$ and $\vec{k}'$. The time dependence arises when the pairing frequency is not negligibly small compared to the Fermi energy. This corresponds to the "strong coupling" limit of the BCS theory[12]. Typical strong coupling superconductors which are well-

described by this modification are lead and mercury. An angular dependence of the pairing interaction leads to an angular dependence of Δ and the energy gap. When the Fermi surface is spherical and V is not proportional to a spherical harmonic, there may also be several superconducting phases.

1.2.3 T_C, λ, and the Gap Structure

I now examine the fundamental parameters of superconductivity in the cuprates. T_C, λ, and ξ all imply that the cuprates are unusual as compared to previously known superconductors.

Within BCS theory, electrons are paired via a mediating boson (in real BCS materials, this boson is typically a phonon). When we can neglect the effect of the bosons on the electronic density of states (the weak-coupling scenario) $T_C \propto \omega_B$, the typical phonon energy. In a weak coupling case, a high T_C implies a large frequency for the mediating boson. However, the "smoking gun" for a phononic mechanism, *e. g.* the isotope effect on T_C, is relatively weak in the cuprates[13, 14, 15]. Interestingly, in the strong-coupling limit, one may work backward from the superconducting properties, to find the properties of the pairing interaction[16]. This sort of analysis suggests a much stronger interaction than a typical electron-phonon one[3].

When the Fermi surface becomes gapped, the excitations are frozen out at low temperature–by the Boltzmann factor, the number of excitations decreases exponentially with decreasing temperature. Measurements of the temperature dependence of λ thereby diagnose the gap structure $\Delta(\theta, \phi)$ about the Fermi surface. Common BCS superconductors have an s-wave (isotropic) gap. If the gap has nodes, then

down to the lowest temperatures there will still be some quasiparticle excitations which will deplete n_s. In typical phonon-coupled superconductors, the gap has no nodes, and hence λ tends to saturate at finite temperatures below T_C. Microwave[17] and μSR measurements on high-quality single crystals of $YBa_2Cu_3O_{6.6}$[18], as well as μSR experiments on single-crystals of $La_{2-x}S_xCuO_4$, indicate that λ shows no sign of saturation, suggesting a d-wave gap with nodes. The gap symmetry relates directly to the symmetry of the superconducting wavefunction and the pairing interaction. Non-s-wave gap symmetry may therefore imply an exotic pairing mechanism in the high-T_C cuprates.

1.2.4 λ,ξ, and the BCS-Bose Crossover Picture

Systematic measurements of λ in ceramic samples of various cuprate series have shown that $T_C \propto n_s/m^*$[19, 20, 21]. This approximate proportionality, known as "Uemura's relation," is satisfied by all of the hole-doped cuprates in the underdoped regime of the SC phase. Because n_s/m^* also represents the Fermi energy of a quasi-2D system, Uemura *et al.*[21] were led to propose that the Cooper pairing in the HTSC cuprates involves an interaction with a characteristic energy which is comparable to the Fermi energy for the doped holes–oposite to the case in the canonical BCS theory. It is interesting to note that, even with $\omega_B \sim E_F$, Cooper's weak-coupling calculation for the existence of Cooper pairs will go through for a sufficiently anisotropic material, where the density of states is quasi two-dimensional.

The idea of a large ω_B, and the short coherence lengths observed in the HTSC cuprates, also provoke comparisons between the SC transition in the HTSC's and Bose condensation. As mentioned above, if the magnetic field in a superconductor varies on a length larger than ξ, then the paired electrons respond to it in unison.

On the other hand, in the field variation occurs on a smaller lengthscale, then the pairing breaks down. In type-II superconductors, this occurs at the upper critical field H_{C2}, where the cores of the fluxoids begin to overlap. Hence, H_{C2} determines ξ. For the cuprates, the values of ξ estimated in this fashion are extremely short–on the order of 10Å–compared to those in typical phonon-coupled superconductors, where $\xi \sim 1000$Å. One possible signature of the Bose-like nature of the transition is the $T > T_C$ "pseudogap" observed in the $T > T_C$ spin and charge excitations of the underdoped cuprates with various methods [22]. Such a gapped excitation spectrum is what one would expect from the formation of pairs above T_C. Figure 1.4 compares the pseudogap, determined from tunneling measurements in $La_{2-x}Sr_xCuO_4$, with the T_C of these materials. Recent work by Uemura and by Tchernyshyov [23, 24, 25] has emphasized that a pseudogap will form if the magnitude of Δ fluctuates with nonzero momenta above T_C. Phenomenologically, this represents the intermediate case between the a mean-field BCS-like and Bose-like types of condensation, and this approach to the underdoped cuprate HTSC's is known as the "BCS-Bose crossover" picture.

1.3 Structure of This Thesis

The data in this thesis were all taken with the various μSR spectrometers at TRIUMF in Vancouver, British Columbia. Chapters 2 and 3 introduce the techniques and tools of μSR.

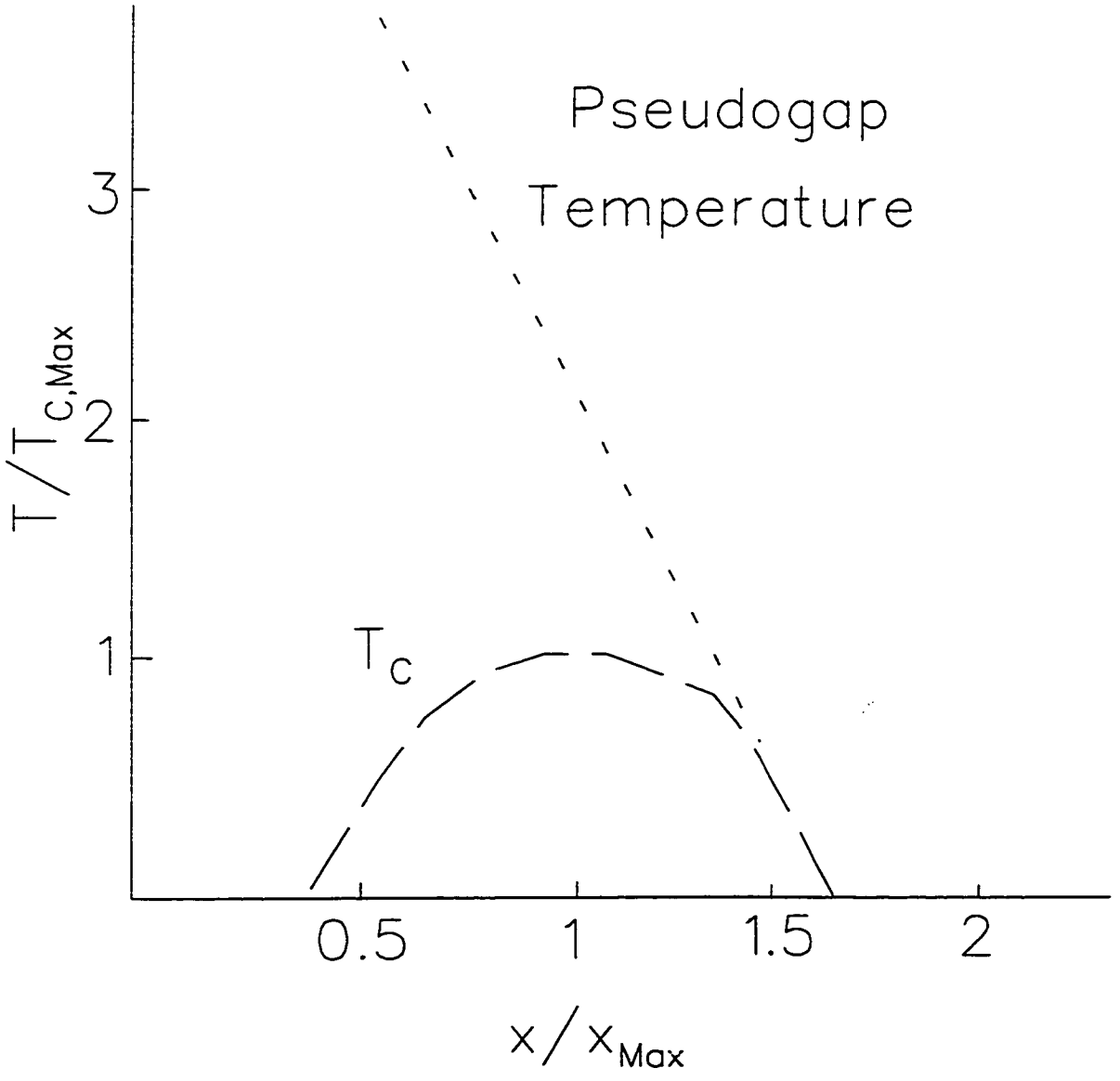

Figure 1.4 A comparison of the pseudogaps and T_C measured in $La_{2-x}Sr_xCuO_4$ (After [22].

1.3.1 Chapters 4–6: Striped Charge Inhomogeneity

At least three of the cuprates: $La_{2-x}(Sr/Ba)_xCuO_4$, $YBa_2Cu_3O_{6+x}$, and $Bi_2Sr_2CaCu_2O_{8+\delta}$, show a remarkable instability of the spin and/or charge degrees of freedom in the normal and superconducting states, which seems to have a stripe-like or modulated structure. In $La_{2-x}Sr_xCuO_4$, this phenomenon has been variously interpreted as incipient Fermi-surface nesting, and the effect of frustrated phase separation of doped holes in an antiferromagnetic background. The tendency toward phase separation or clumping of doped holes would arise because several holes in close proximity break fewer AF bonds in the CuO_2 plane than if these holes were widely separated.

$La_{2-x}(Sr/Ba)_xCuO_4$ is by far the most studied of the stripe systems. The stripes, which were first identified as dynamical modulations of the spin density below T_C, are stabilized by the substitution of Nd at the La site. It has been hypothesized that these stripes are related to the spontaneous suppression of T_C in $La_{2-x}(Sr/Ba)_xCuO_4$ without Nd at $x \sim 0.125$, and the magnetic order which arises when the superconductivity is suppressed. In Chapter 4, I report measurements in which the μSR techniques are used to probe the magnetic order in both $La_{1.875}Ba_{0.125}CuO_4$ and $La_{1.6-x}Nd_{0.4}Sr_xCuO_4$. These measurements allow an estimate of the ordered magnetic moment and magnetic ordering temperature–which are nearly the same for all of the La-based materials for $x = 0.125, 0.15$.

The identification of the stripes has prompted intuitively pleasing speculations on the competition between the stripe phases and superconductivity: a resurgence of the background antiferromagnetism (in altered form) at the expense of the superconducting order parameter. However, magnetic susceptibility measurements suggest that, even below the static stripe ordering temperature, the static stripe materials

have a superconducting component. The relative magnitudes of the magnetic and superconducting volumes of $La_{1.6-x}Nd_{0.4}Sr_xCuO_4$ form the subject of Chapter 5. In chapter 6. I air some speculations about the interplay between the magnetic/charge order and the superconductivity.

1.3.2 Chapter 7: Zn Impurity Effects, Local Depletion of the Condensate

One way to probe the superconductivity in the cuprates is to measure the effects of impurities on the superconductivity. The motivation for this class of experiments derives in part from Anderson's theorem, which predicts the effects of impurities on a BCS superconductor. According to Anderson's theorem[6], a nonmagnetic impurity will have little effect on the T_C of a superconductor with an isotropic "s-wave" energy gap. Conversely, a magnetic impurity kills superconductivity comparitively efficiently in an s-wave superconductor. Extensions of Anderson's theorem to the case of a superconductor with interactions where the sign of Δ changes around the Fermi surface show that, in this case, the roles of magnetic and nonmagnetic impurities are reversed. Naively, for the cuprates, Zn is an ideal candidate for such a mission: Zn has the same nominal valence as Cu, but has a filled 3d-shell and no free moment. However, the presence of the antiferromagnetic background complicates the interpretation of these experiments: Zn seems to induce a magnetic moment on or around itself in the doped CuO_2 plane. The results of microwave experiments on high-quality single crystals of $YBa_2Cu_3O_{6+x}$ substituted with Zn seem qualitatively consistent with a gap with a "d-wave" symmetry (e. g. for which the gap parameter Δ changes sign like a d-wave around the Fermi surface) if Zn acts as a nonmagnetic scatterer.

With μSR, one may measure both the T_C and the condensate density n_s. Chapter 7, presents such measurements on $La_{2-x}Sr_xCuO_4$ and $YBa_2Cu_3O_{6.63}$ systems which

have been substituted with Zn at the planar Cu site. The reduction in the condensate density is consistent with a "Swiss Cheese" model for which the superconductivity is destroyed in a radius ξ around each impurity. The combined reduction in T_C and n_s are inconsistent with the extant theory of pair-breaking scattering in a superconductor with a d-wave gap; this theory depends on a homogeneous description of the charge density in the SC plane.

Chapter 2

Experimental Techniques

2.1 The Muon Decay

Muon spin rotation/relaxation (μSR) is a powerful method of determining the local (microscopic) magnetic field, with applications to magnets and superconductors. Although the methods vary slightly depending upon what one wants to measure, all of the measurements depend upon the magnetic and decay properties of the muon. The muon is a spin-1/2, positively (μ^+) or negatively (μ^-) charged lepton, with a gyromagnetic ratio $\gamma_\mu/2\pi = 13.5534kHz/G$. With a rest mass m_μ 207 times greater than that of an electron, the muon is unstable with lifetime $\tau_\mu = 2.197\mu s$. It decays via the weak interaction into an electron and two neutrinos:

$$\mu^+ \rightarrow e^+ + \nu_e + \bar{\nu}_\mu,$$

$$\mu^- \rightarrow e^- + \bar{\nu}_e + \nu_\mu.$$

The crucial feature of this decay for the purposes of μSR is that it violates parity conservation. In the rest frame of the muon, the probability $d\Gamma$ of seeing a decay electron in an element of solid angle, $d\Omega$, is correlated with the direction of the muon spin at the time of decay, according to the rule:

$$d\Gamma/d\Omega = \frac{\exp(-t/\tau_\mu)dt}{\tau_\mu} \times \frac{1 + I(\epsilon)\cos\theta}{4\pi} \times \rho(\epsilon)d\epsilon,$$

with θ measured from the direction of the muon spin,

$$I(\epsilon) = (2\epsilon - 1)/(3 - 2\epsilon),$$

the intinsic asymmetry of the decay,

$$\rho(\epsilon) = 2(3 - 2\epsilon)\epsilon^2,$$

the density of final states factor, and where ϵ is the energy of the decay electron scaled by its maximum possible energy. Neglecting the electron and neutrino masses, the theoretical maximum electron energy is approximately $m_\mu c^2/2$, corresponding to the case for which the two neutrinos move along the same direction, and the electron moves in the opposite direction. The minimum electron kinetic energy is zero, corresponding to the electron at rest and the two neutrinos travelling in opposite directions.

2.2 Basic Principles of the μSR Measurement

The decay anisotropy enables the statistical measurement of the spin direction of a large number of identically prepared muons. Because the muons posess a magnetic moment, they will precess in a magnetic field according to the Bloch equation:

$$\frac{d\langle\vec{S}\rangle}{dt} = \gamma_\mu \langle\vec{S}\rangle \times \vec{B},$$

where $\vec{S}$ is the spin direction, $\vec{B}$ is the magnetic field, and the angled brackets denote the quantum mechanical expectation value. Implanting many muons into a sample and histogramming the electron directions as a function of time allows the reconstruction of the muon spin direction as a function of time, and hence of the magnetic field the muons experienced.

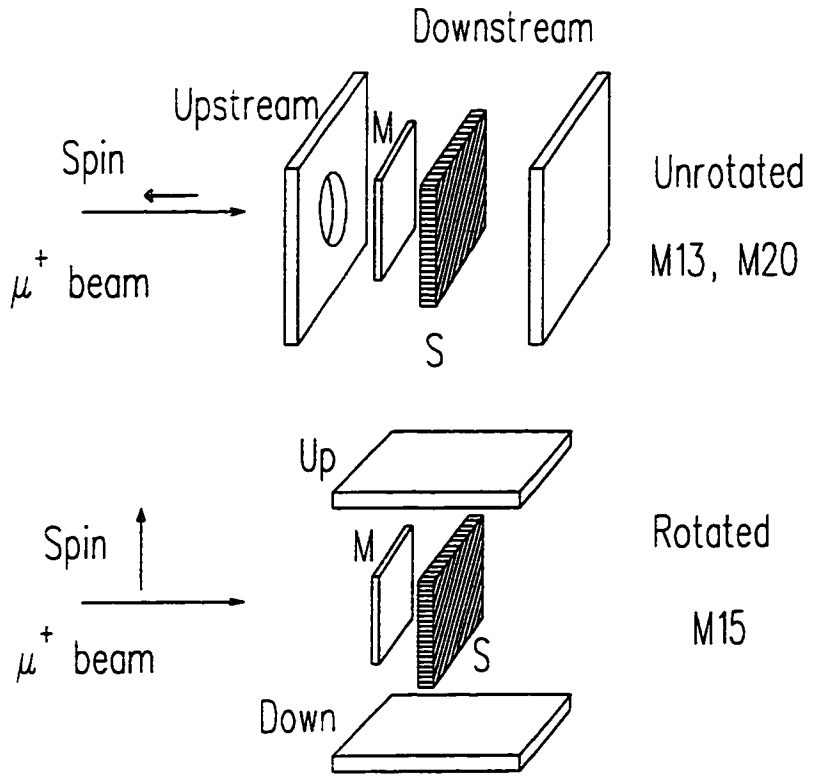

Figure 2.1 Cartoon version of a typical μSR experiment at TRIUMF in Vancouver, BC. M represents the thin muon counter which signals the entrance of the muon. S represents the sample. The detector geometries shown are appropriate for the indicated muon beamlines at TRIUMF.

A convenient way to determine the spin direction is to form the asymmetry between the numbers of positrons emitted parallel and antiparallel to the original muon polarization direction $\hat{P}_\mu$. Figure 1 shows a schematic of such a μSR apparatus. The number of positron counts through each detector is histogrammed as a function of time. The histograms have the general form $N(t) = N_0 e^{-t/\tau_\mu}(1 + CaG(t)) + B$. Here N_0 is the total number of decay positrons in the histogram which would be seen in the absence of any initial polarization. N_0 is proportional to the total number of muons stopped, to the averaged energy acceptance of each detector, and to the solid

angle of each detector. C is the projection of $\hat{P}_\mu$ onto the line connecting the center of the sample with the center of the detector and is equal to ± 1 for typical zero-field (ZF) measurements. The quantity a is the intrinsic asymmetry of the muon counter. This is the asymmetry of the muon decay I as a function of energy, averaged over the energy acceptance and solid angle of the detector. Finally, B is the background in the detector, which for now I will assume to be zero (the background subtraction mechanism for the actual experiments is detailed below).

The normalized polarization function, $G(t)$, contains all of the information related to the magnetic field in the sample. In what follows, a is assumed to be constant (that is, the detectors are identical in their response to positrons of a given energy). The quantity

$$\frac{N_+(t) - N_-(t)}{N_+(t) + N_-(t)}$$

defines the experimental asymmetry $A_{\rm exp}(t)$. If we normalize by the N_0 for one of the detectors, then we may write

$$A_{\rm exp}(t) = \frac{1 - \alpha + (1+\alpha) I G(t)}{1 + \alpha + (1-\alpha) a G(t)},$$

where $\alpha = N_{0,+}/N_{0,-}$. We invert the expression for $A_{\rm exp}(t)$ to obtain the "corrected asymmetry" $A(t)$, where

$$A(t) = aG(t) = \frac{A_{\rm exp}(t)(1+\alpha) + \alpha - 1}{1 + \alpha + A_{\rm exp}(t)(\alpha - 1)}.$$

2.3 How the Muons are Prepared

The muons in the experiments of this thesis were produced at the TRIUMF meson facility in Vancouver, BC. There, an enormous cyclotron bombards a production target (typically Be or C) with 500MeV protons. The ensuing nuclear collisions

produce copious quantities of positive and negative pions, which then decay via the weak interaction into muons and muon neutrinos:

$$\pi^+ \rightarrow \mu^+ + \nu_\mu,$$

$$\pi^- \rightarrow \mu^- + \bar{\nu}_\mu.$$

Because the neutrinos are 100% spin-polarized (there are no right-handed neutrinos), the muons produced in this fashion are also 100% spin polarized to conserve angular momentum. The positive muon spin points in the direction opposite its momentum. Both negative and positive muons can be used for μSR experiments. However, negative muons in matter occupy a very low orbital within the electron cloud, and are subject to extensive depolarization as they thermalize in the sample. In addition, negative muon capture by nuclei introduces spurious lifetimes into μ^-SR measurements. Positive muons, on the other hand, tend to remain outside the electron cloud and may often be thought of as localized, point-like probes sitting atop an atom. The μ^+SR experiments described in this thesis use those muons which decay from pions which are at rest at the surface of the target. These so-called "surface muons" have a definite momentum of 29.8 MeV/c, and are therefore easily selected by crossed electric and magnetic fields. With collimation, a beam of muons which are approximately 100% polarized in a particular direction with respect to the lab z-axis is brought to the sample position. The typical surface-muon stopping range is about 170 mg/cm^2, which means that surface muons stop well within the sample surface, and are appropriate for bulk measurements of the local magnetic field.

2.4 Some Details of the Apparatus

The apparatus used in simple μSR experiments falls into four classes: beamlines, temperature control, detection, and electronics. Here I outline only the latter three processes. As for the beamlines, all of this information is extremely site-specific, and anyone reading this document would be better-served by simply reading the TRIUMF documentation.

2.4.1 Temperature Control

For the measurements presented in this thesis, the refrigerator is often a garden-variety Janis ^{4}He gas-flow cryostat. This cryostat consists of two nested Dewars and a central vacuum space, where the sample resides. The outermost reservoir is filled with l-N_2; the inner reservoir is filled with l-He. A small flow of l-He is allowed to throttle through a large thermal mass (the "diffuser") into the sample space. Pumping on the sample space thereby draws He gas at the throttled temperature past the sample. The minimum obtainable temperature in this arrangement is about 2K. Inside the sample space, at the end of a long insertion rod, the sample sits in a cradle which is wired for thermometry and for a heating element. Usually both the diffuser and the sample are actively heated to provide stable temperature control. Some of the measurements in this thesis used a different, "continuous flow" cryostat, in which a separate helium dewar takes the place of the He reservoir.

The temperature is read by calibrated CG resistors or GaAlAs diodes (low temperature) or Pt resistors (high temperature). Temperature control usually involves a commercially available (Lakeshore) feedback device with a PID (Proportional-Integral-Differential) algorithm. One achieves a stable temperature by balancing the

heat flow against the cooling power determined by the cryogen flow. The appropriate levels of each depend on the sample heat capacity and the structure of the cryostat. One pitfall of gas-flow cryostats is that, at the very lowest temperatures, liquid helium tends to accumulate in the sample space. This has the effect of spuriously depolarizing incoming muons and increasing the background signal. To avoid this effect, one usually uses a manually controlled heater to periodically vaporize the accumulating liquid.

2.4.2 Detectors

Muon and positron events are detected in scintillation counters–which, for the present experiments, were made at TRIUMF. Lucite light-guides lead the pulse to a photomultiplier-cascade tube, whose signal is carried to the electronics for shaping and triggering. The same kinds of detectors are used to sense both the incident muons and the decay positrons. The only difference between a muon and a positron counter is the thickness: the muon counter must be thinner than a muon's stopping range in the scintillator to enable the muons to enter the sample. The detector arrangement is determined by the "trigger," i.e. the logical sequence of detector firings which leads to a histogrammed muon-decay event. The trigger is determined by the logical layout of the data acquisition electronics.

There are a few sources of spurious signal which must be minimized. Care must be taken that the detectors have no "light leaks" which give a spurious signal; for this purpose they are wrapped in black electrical tape or otherwise shrouded. Even so, there will be some "dark noise" due to random firings of the phototube. Pulses from beam positrons in the thin muon counter provide more signal which must be discarded. Fortunately, beam positrons deposit less energy in the scintillators than

do the incident muons, so these pulses are easy to descriminate in the electronics. Even ignoring dark noise and beam contaminants, there will be some pulses due to cosmic rays, local radioactivity, and any other environmental factors which add to a (hopefully) time-independent background, which is subtracted in the data analysis.

2.4.3 Electronics

Figure 6 shows a block diagram of the electronics for a simple-trigger experiment. A "good" data event satisfies the following conditions: (1) a muon passes through a thin scintillator placed before the sample; (2)no other muons pass through the thin scintillator; (3)at a later time, a positron passes through one of the counters arrayed about the sample. To minimize the effects of dark noise, each counter is often composed of two layered, independent detectors. More complex triggers involve using the counter geometry to determine whether the muon actually lands in the sample or on the sample backing (for example, in the Knight-shift apparatus used in chapter 5); or the vetoing of incident muons which miss the sample.

The process by which a pulse from the detectors is shaped and qualified as "good data"–or rejected–may be broken into 4 stages. The raw pulses from the detectors are descriminated and regularized in CFD's (Constant Fraction Discriminators). The discrimination threshold allows the electronics to ignore the band of events from contaminant positrons. Coincident positron detectors may be run with a wider acceptance, as the random pulses from one detector will not appear in its partner. The regularization is done by adding to the original incoming pulse, a time-delayed, scaled, and inverted version of the original pulse. If, regardless of pulse height, all of the pulses from the detector have the same characterisstic shape, then the zero-crossing of the total (original pulse+ scaled, delayed and inverted original pulse) will

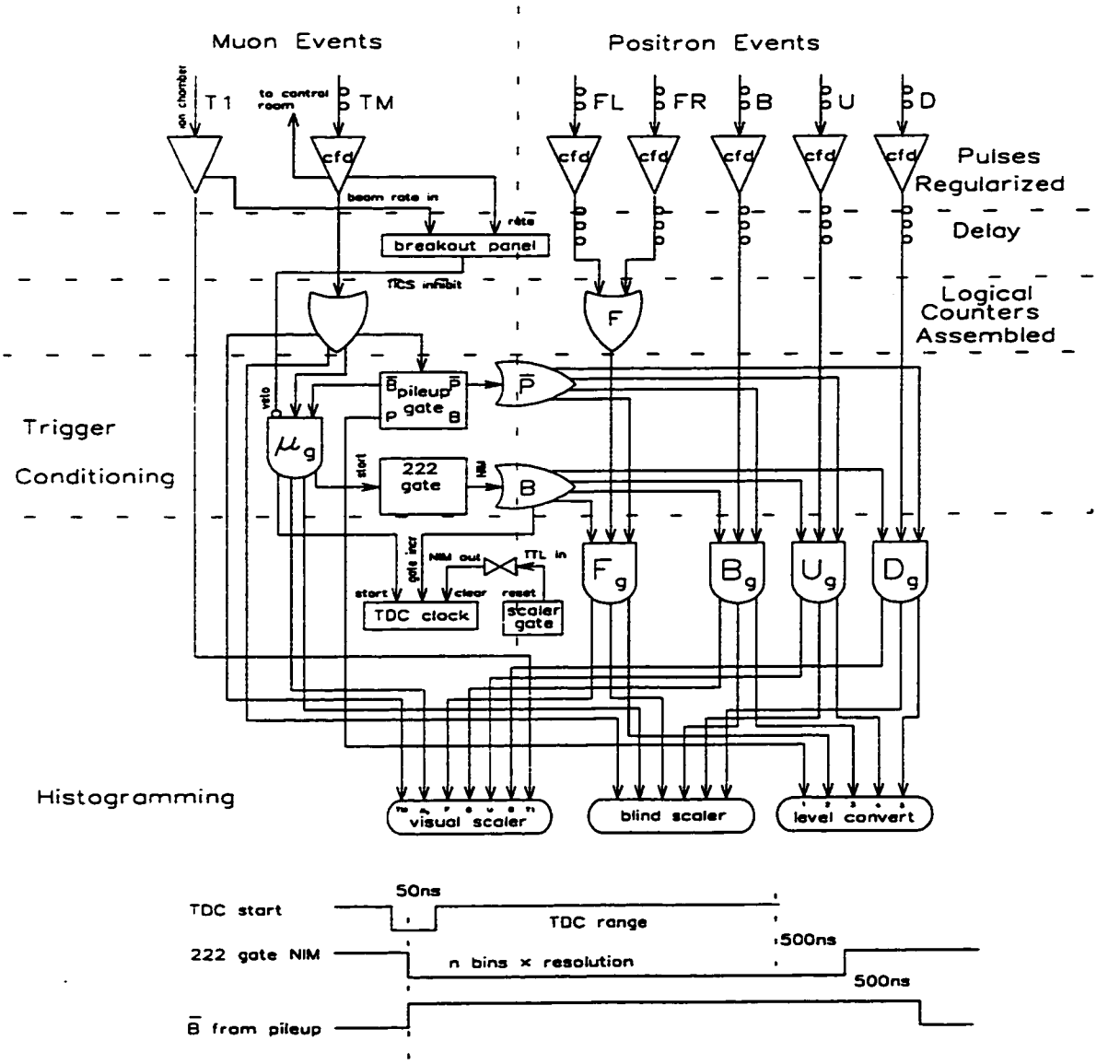

Figure 2.2 Block diagram of the data-handling electronics for a simple-trigger time-differential μSR experiment.

occur at the same time. At the zero crossing, the CFD puts out a square logic pulse.

Next, a delay is put in for the purpose of background subtraction. Pulses from positron events are delayed so that any signal within the delay window is due to background (which is assumed to be time-independent). A typical delay window is approximately 200-300 ns. This background is subtracted from each detector signal "by hand," before the data is fit.

The next step in the logic combines the physical detectors into the logical counters. Care must be taken to synchronize the pulses from the component detectors, so that they arrive at the same time. If the physical detectors are layered, coincident detectors, then the pulses are logically ANDed together. For reasons of experimental geometry, the upstream detector often feeds to two phototubes, each of which may independently send a pulse. In this case, the pulses will be logically ORed together.

Now the trigger conditions are defined. For the positron event to be counted, prior to the positron pulse, a muon pulse must have arrived. A single muon pulse from the thin counter will start a digital clock, open a data gate, and flip a logical switch to the "busy" state. Any later muon pulse arriving within the data gate will cause the "pileup" condition, which invalidates the positron events from both muons. Pileup events are useless in a time-resolved experiment, because there is no way to determine which decay positron belongs to which muon.

A muon which arrives when the system is not in the "busy" state, and opens the data gate is called a "gated" (or "provisionally good") muon. If no other muons arrive within the data gate, any positron events are also "gated." In the final, histogramming step, the muon arrival time, positron arrival time, and logical detector are scaled and recorded.

The histograms are read periodically into a VAX computer, where they are available for online data analysis. With this system, one can watch the data accumulate in "quasi-real time" and steer the experiment accordingly.

Chapter 3

More on μSR Techniques

This chapter presents the basic features of μSR data as a function of the magnetic field distribution in a sample. The total magnetic field at the muon site is the sum of the fields due to the sample alone (the intrinsic nuclear and electronic moments), the bulk response to an applied field, applied field itself, and the demagnetization field due to the sample shape. Most of the data presented in chapters 4-6 was taken either in zero applied field, or in a configuration where the demagnetization factor $\sim$ 1. For the one exception, a measurement of a crystal in an applied LF=2kG (section 4.2.3), I only consider the qualitative features of the data which are independent of the demagnetization field. Hence, in sections, 3.2–3.3 and 3.5, the demagnetization is not taken into account.

3.1 ZF-μSR

I now outline the general features of the zero-applied-field (ZF) μSR corrected asymmetry spectrum. The ZF-μSR techniques are applied extensively to the stripe phases of the 214 system in the next chapter.

If a well defined electronic spin structure exists, then muon spins implanted at

magnetically equivalent lattice sites precess in identical fashion, leading to a statistically large precession of the muon spin asymmetry signal at a frequency defined by the field at that site: $\nu = \gamma_\mu/2\pi B_{\rm Local}$, where $\gamma_\mu/2\pi = 13.5$ MHz/kG. The static field muon asymmetry signal is thus proportional to the frequency Fourier cosine transform of the local field distriubution.

The relaxation envelope of the oscillating signal reveals the characteristics of the field distribution. For a finite number of components, the asymmetry spectrum shows characteristic beats and (in theory) oscillates forever. The recovery time for the asymmetry in this case is just the inverse beat frequency. As the frequency peaks broaden, then at each field there will be an oscillating component which beats with other fields at a much different frequencies. The typical recovey time therefore becomes larger, and for a dense field distribution, becomes infinite. For the case of several broad frequency peaks which are separated by more than their width, the muon asymmetry signal will appear "multicomponent," manifesting beats, but will not recover its full amplitude in the long time limit. Figures 3.1 and 3.2 illustrate these points. In Fig. 3.1 the raw asymmetry spectrum is constructed from an idealized sample conatining two distinct static magnetic fields at the muon site. Figure 3.2 shows the idealized spectrum for a sample with two different muon sites with progressive static broadening of the frequency lines.

A fairly general phenomenological form for the ZF asymmetry signal is therefore:

$$A(t) = A_\perp \sum_{i\neq 0}^{I_{Max}} W_i \cos(2\pi\nu_i t) \times \exp(-(\Lambda_i t)^{\beta_{\perp i}})$$

$$+A_\parallel \times \exp(-(\Lambda_0 t)^{\beta_\parallel}).$$

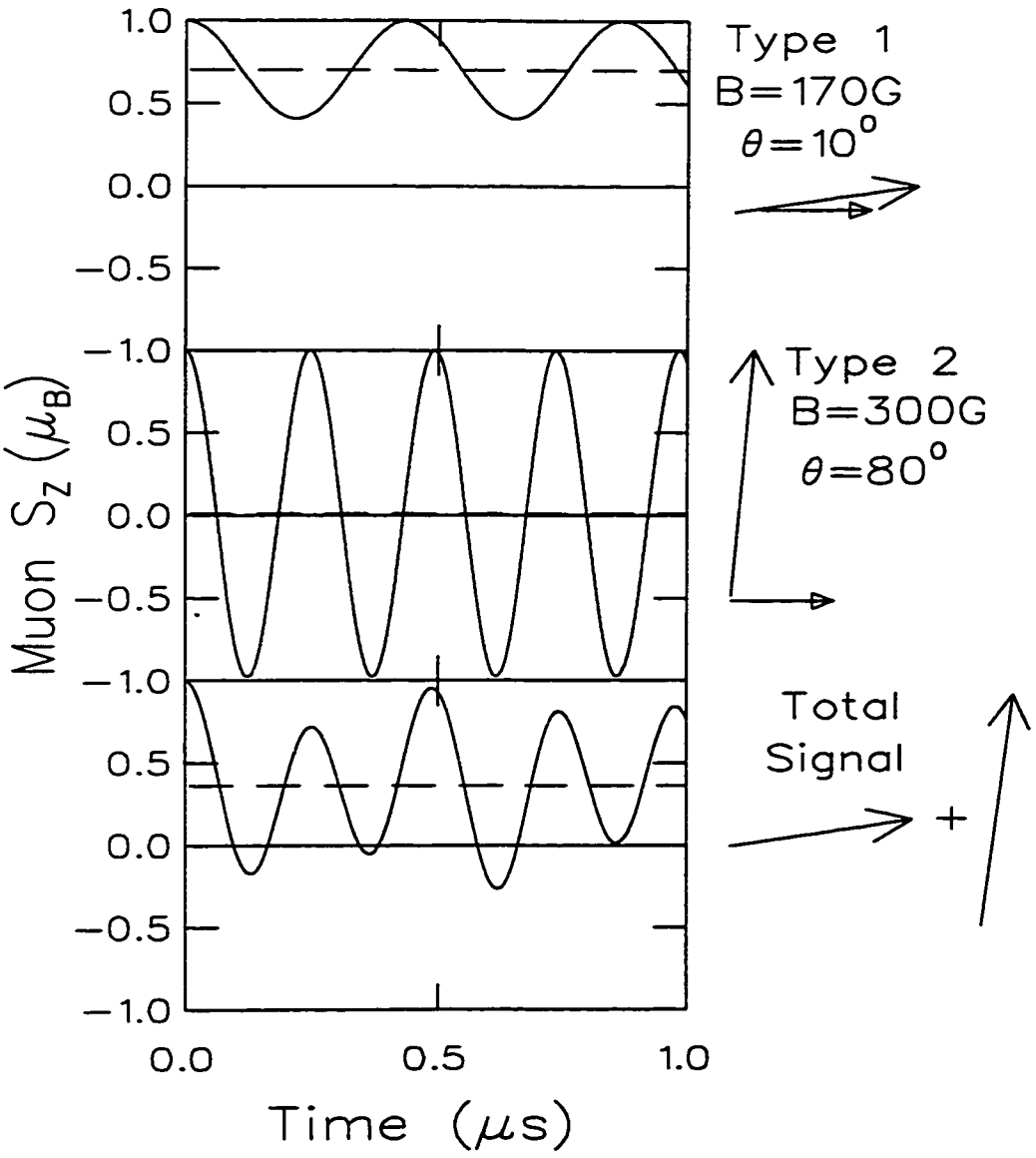

Figure 3.1 Construction of an idealized ZF-μSR signal from the signals due to two different magnetic muon sites.

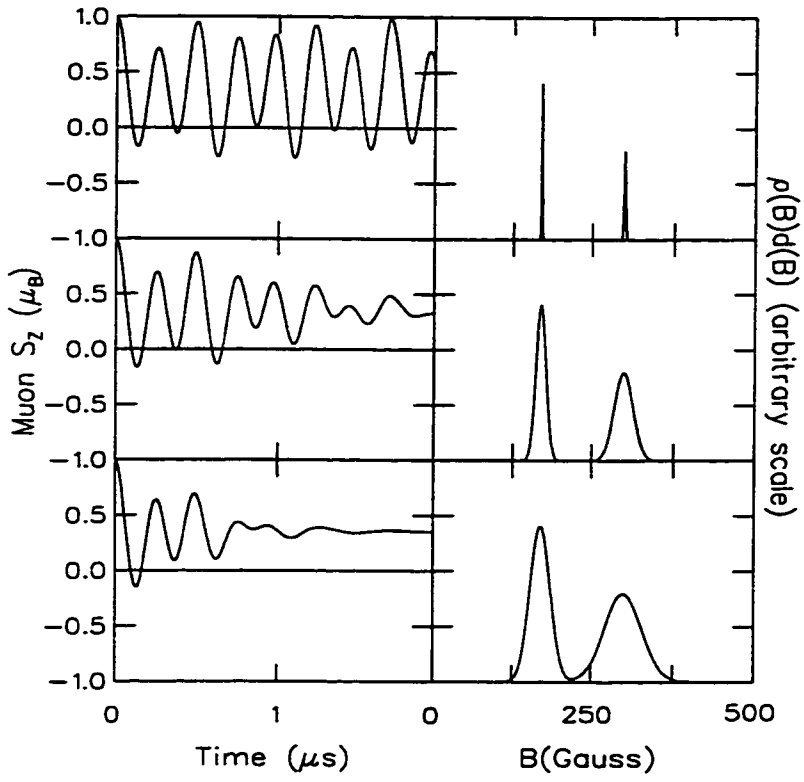

Figure 3.2 The effect of progressive static broadening on a signal composed of two oscillating components.

The ratios $W_i : W_j; i, j \neq 0$ denote the relative weights of the frequency components which are separated by more than their distribution widths, and ν_i is the mean frequency of each component. One would also expect a variety of longitudinal relaxation signals, each characterized by its own relaxation rate Λ and exponent β, but the absence of a distinguishing frequency makes the $A_{||}$ signal difficult to analyze in this way.

The ratio $A_\perp : A_{||}$ (the ratio of oscillating to nonoscillating parts of the asymmetry signal) reveals the average degree to which $\hat{P}_\mu$ aligns with $\vec{B}_{\text{Local}}$. Muons with $\hat{P}_\mu \parallel \vec{B}_{\text{Local}}$ do not precess, although their polarizations may be dynamically relaxed by perpendicular fluctuations. In a homogeneous polycrystalline sample, with a static component to the local field, because the crystallites orient randomly with respect to $\hat{P}_\mu$, $A_\perp/(A_\perp + A_{||}) = \frac{2}{3}$, the isotropic average perpendicular component of the muon spin. For a ceramic sample where only a V_{ord} portion of the total volume V_{tot} orders, $A_\perp/(A_\perp + A_{||}) = \frac{2}{3} \times V_{\text{ord}}/V_{\text{tot}} < \frac{2}{3}$. In a single crystal, given $\hat{P}_\mu$, the $A_\perp$ fraction will be given by $V_{\text{ord}}/V_{\text{tot}} \times \langle \sin^2 \theta_{\mu-B} \rangle$, where $\theta_{\mu-B}$ is the angle between $\hat{P}_\mu$ and $\vec{B}_{\text{local}}$ at the muon site, and the brackets denote an average over domains of V_{ord}. The parameters Λ and β incorporate relaxation due to the width of each component distribution and dynamics. Let Δ represent the instantaneous value of B_{local}. When $\Lambda < \gamma_\mu \Delta$, one may distinguish dynamic from static relaxation by inspection. The relaxation of the $A_{||}$ part of the asymmetry signal results from fluctuations in the perpendicular directions. Hence in a homogeneously ordered powder sample with fluctuating fields, the $A_{||} = \frac{1}{3}$ fraction relaxes to zero. In such systems, there will is dynamic broadening of the oscillating components as well. A static magnetic environment, by contrast, may cause a static disorder-induced broadening of the oscillating components, but the $A_{||}$ fraction persists in the long time limit described by $t \gg 1/\gamma_\mu \Delta$.

3.2 LF-μSR

The "long time limit," however, may not always be accessible in the experiment. Typical time-differential μSR spectra are limited to about 10μs. A more definitive way to distinguish dynamic relaxation from static relaxation is the application of a longitudinal field (LF) which is a few times larger than any ordered field in the sample. The muons precess about the total field with frequency ν. In sufficiently strong LF, the asymmetry does not oscillate because the local field and the initial muon polarization are nearly parallel, so that $A_\perp \to 0$. Then, any relaxation is due to dynamics which cause transitions between the local muon Zeeman states. We consider a Markovian spin decay, with an inverse spin lifetime of ν_d. When ν_d is large compared to ν, the relaxation rate probes the spectral density of the field fluctuations at energies $2h\nu$. The resulting muon asymmetry spectrum is approximately exponential in shape:

$$A(t) = A(0)\exp(-\Lambda_{\text{homog}}t),$$

with

$$\Lambda_{\text{homog}} = \frac{2\Delta^2\nu_d}{(2\pi\nu)^2 + \nu_d^2}.$$

If the distributions of Δ or ν_d vary over the sample volume, then the relaxation function is an integral of various exponentials over the sample volume. The relaxation function is often well described by the "stretched-exponential" form

$$A(t) = A(0)\exp(-(\Lambda t)^\beta),$$

where now

$$\Lambda = D \times \Lambda_{\text{homog}},$$

with D, a number of order unity, and β determined by the distributions of Δ and ν_d.

3.3 TF μSR

In a transverse-field (TF) μSR experiment, the muon beam is polarized perpendicular to an applied magnetic field $\vec{H}$. Understanding of the ZF technique begets understanding of the TF technique: the major difference is that in the TF case, the applied field adds a central frequency to any intrinsic broadening factors in the sample. In an otherwise nonmagnetic environment, the transversely polarized muons would precess at the frequency defined by the applied field. As in ZF-μSR, the broadening of the TF frequency, which in the time domain manifests as damping of the precession, results from the combination of the static and dynamic magnetism inherent in the sample.

Whereas in LF-μSR the depolarizing fluctuations are perpendicular to $\vec{H}$, in TF-μSR fluctuations parallel to $\vec{H}$ can also depolarize the muon spins. If the fluctuations are isotropic, then the combination of LF and TF-μSR may be used to extract the static magnetic response of the sample. If (as is the case for most of the $La_{2-x}Sr_xCuO_4$ and $YBa_2Cu_3O_{6.63}$ samples examined in chapter 7) the ZF relaxation rate is predominantly due to nuclear dipolar fields, the observed TF frequencies are dominanted by the static electronic response of the sample. Common applications of TF-μSR are Knight-shift measurements of the uniform electronic susceptibility, and the inhomogeneous broadening of H in the superconducting state due to the vortex lattice in a type-II superconductor.

In chapters 5 and 7, the TF-μSR method is applied to cuprate superconductors in the intermediate-field state, e. g. $H_{C1}(T) < H < H_{C2}(T)$, where H_{C1} and H_{C2} are the lower and upper critical fields, respectively, at all temperatures $T < T_C$. In the following sections, I describe some of the intricacies involved in describing TF-μSR data in superconducting samples.

3.4 Type-II Superconductors in Applied Fields–Basic London Theory

Abrikosov has shown that, in type-II superconductors, near T_C or for $H \sim H_{C2}$, in the absence of pinning effects, the fluxoids tend to form a lattice stabilized by the competition between the external "pressure" of the expelled magnetic field and inter-fluxoid repulsion. The phenomenological expansion of this analysis to arbitrary fields is the province of the modified London model.

3.4.1 The London Equations

The London equations are phenomenological descriptions of the magnetic field and current distribution in a superconductor under an applied field, which however may be derived as a consequence of the full BCS theory when $\lambda_L/\xi \gg 1$, as is true in the cuprates. First consider the simplest case of a semi-infinite slab of superconductor, bounded by vacuum, with an applied magnetic field paralel to the face of the slab.

The essential approximation of the London theory is the *locality* of the current response to the magnetic vector potential (the Londons' ansatz)[11]:

$$\vec{J}(\vec{r}) \propto \vec{A}(\vec{r}).$$

As mentioned above, the Londons' ansatz results from the rigidity of the superconducting wavefunction. Writing the current operator as

$$\vec{J} = \psi(\nabla + \frac{2iq\vec{A}}{c})\psi^* - \psi^*(\nabla - \frac{2iq\vec{A}}{c})\psi,$$

gives the Londons' ansatz (to within a gauge choice) for $\psi \approx \psi_0$.

To derive the screening in the London limit, write

$$\vec{J} = q \times n_s \times \vec{v_s},$$

the superconducting carrier density times the supercarrier charge, times the supercarrier velocity. For a perfect conductor (no scattering)

$$\frac{d\vec{J}}{dt} = \frac{n_s q}{m^*} \times q\vec{E}.$$

Using the Maxwell equation

$$\nabla \times \vec{E} = \frac{-1}{c}\frac{\nabla \times d\vec{A}}{dt},$$

we have, for a particular choice of Gauge known as the "London Gauge"

$$\frac{d}{dt}(\vec{J} + \frac{n_s q^2}{m^* c}\vec{A}) = 0.$$

The Londons' ansatz then implies that the constant of proportionality between $\vec{J}$ and $\vec{A}$ is c/λ_L^2, where λ_L is the famous London penetration depth. To see how it got that name, take the curl of Londons' ansatz, and use the Maxwell equation

$$\nabla \times \vec{B} = \frac{-1}{c}\vec{J}.$$

The result reads:

$$\vec{B} + \lambda_L^2 \nabla \times \nabla \times \vec{B} = 0.$$

For a semi-infinite sample (superconductor for, say, $x < 0$) with an applied magnetic field in the z-direction, the London equation implies the exponential decay of the magnetic field and screening current density as one moves farther into the superconducting region:

$$\vec{B}(x) = \vec{B}(0)\exp(-x/\lambda_L), (x \leq 0),$$

$$\vec{J}(x) = \vec{J}(0)\exp(-x/\lambda_L), (x \leq 0).$$

Now consider an isolated fluxoid. The geometry changes from cartesian to cylindrical. The response of the superconductor to a very narrow (δ-function) core of

normal state material is just what one would get by wrapping the cartesian result around on itself: the response is just the Green's function for a cylindrical London equation, which turns out to be just a Bessel equation. The result is

$$\vec{B}(r) = \frac{\phi_0}{2\pi\lambda_L^2} K_0(r/\lambda_L),$$

where K_0 is the zeroth-order damped Bessel function of the second kind–a. k. a. the cylindrical analogue of an exponential[11].

For a flux lattice, the London equation has a source term which is just the lattice sum of vortices:

$$\lambda_L^2 \times \nabla \times \nabla \times \vec{B} + \vec{B} = \phi_0 \times \sum_i \mathcal{F}(\vec{r} - \vec{r}_i).$$

Here $\mathcal{F}$ is the spatial form of the field as a function from the center of a fluxoid; in the "extreme London limit" ($\lambda_L/\xi \gg 1$), $\mathcal{F}(\vec{r} - \vec{r}_i) \to \delta(\vec{r} - \vec{r}_i)$. As a consequence of this periodicity, the London equation for a vortex lattice is commonly Fourier transformed, and solved in wavevector space. The result in the extreme London limit is, for an isotropic superconductor:

$$\vec{B}(\vec{k}) = \frac{\bar{\vec{B}}}{1 + k^2\lambda_L^2}.$$

The sum over Fourier components at one of the lattice points diverges as $k \to \infty$: this is the consequence of neglecting the structure of the vortex core. Taking the core structure into account multiplies $\vec{B}(\vec{k})$ by a form factor $\mathcal{F}(\vec{k})$ which eliminates the divergence. Physically, this high-k cutoff results from the suppression of the superconducting state within approximately ξ of the center of a fluxoid. The screening currents move faster near the center of the fluxoid. The supercurrent velocity modifies the excitation spectrum of the superconducting condensate, and the superconducting state is suppressed. Hence the magnetic field is only weakly screened, and so the field at $r < \xi$ does not differ so much from the field at $r = 0$.

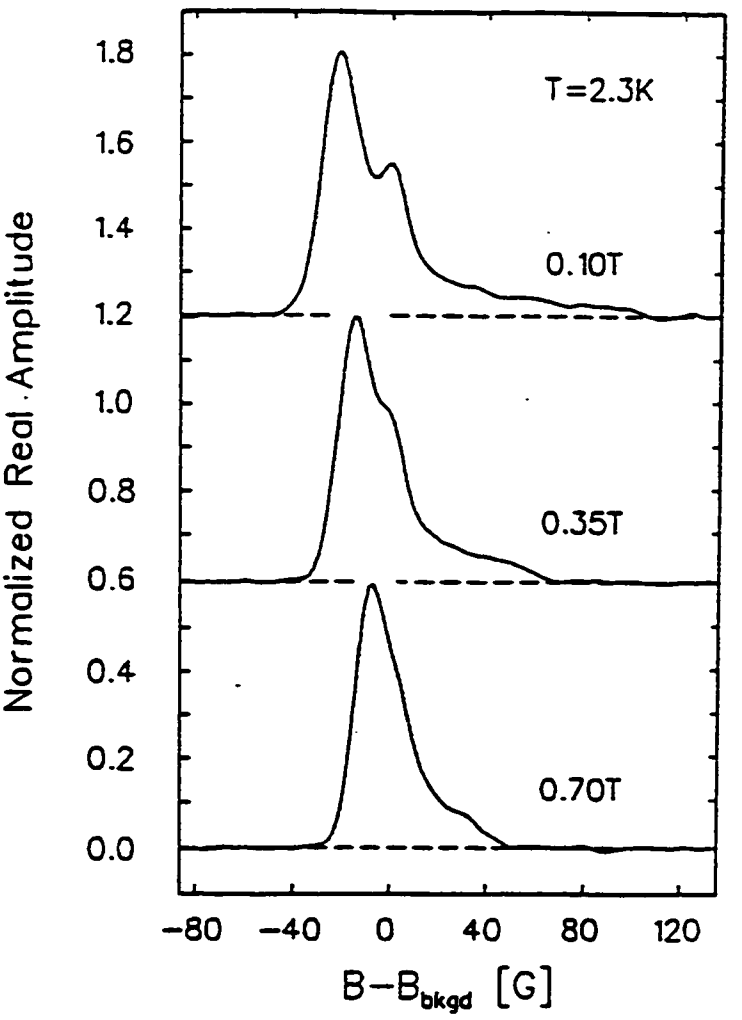

Figure 3.3 Abrikosov Lineshape observed in $NbSe_2$ (from ref. [26].)

The effects of the two lengthscales,λ and ξ, on the muon precession signal are most easily understood by looking at the Fourier transform. Figure 3.3 shows the Fourier transform of μSR spectra well below T_C. This spectrum shows the signatures of a frozen flux lattice. The overall asymmetric shift of spectral weight to lower frequencies is due to the Meissner screening of the magnetic field over the lengthscale λ_L. The high-frequency tail comes from those muons which sit closer to the flux cores. The highest observed frequency corresponds to the maximal field which occurs inside the fluxoid core, where the superconductivity breaks down.

The cuprates are layered materials, and therefore the flux lattice in the cuprates

is better described by a uniaxial solution[27]:

$$B_i(\vec{K}) = \frac{\bar{B}_i}{1+\lambda_\perp^2 k^2}[\delta_{z,i} - \frac{(\lambda_\parallel^2 - \lambda_\perp^2)k_{\perp,z}k_{\perp,i}}{1+\lambda_\perp^2 k^2 + (\lambda_\parallel^2 - \lambda_\perp^2)k_\perp^2}],$$

where $\lambda_\perp$ and $\lambda_\parallel$ are the respective penetration depths for external fields oriented perpendicular and parallel to the symmetry axis, and $k_\perp$ is the component of $\vec{k}$ perpendicular to the symmetry axis. When the applied field is parallel to the symmetry axis, then the lineshape is identical to that of an isotropic superconductor with $\lambda = \lambda_\perp$. On the other hand, when the applied field is perpendicular to the symmetry axis, the measured penetration depth is the geometric mean $\sqrt{\lambda_\perp \lambda_\parallel}$. This fact expresses the compromise between the superconducting screening, on the one hand, and the conducting anisotropy, on the other. Currents driven parallel to the symmetry axis will still try to move perpendicular to it. This situation is particularly fortuitous because it allows one to study ceramic or polycrystalline samples of highly anisotropic superconductors with very little correction due to the anisotropy: the effective penetration depth will be dominated by the shorter value. Ceramic samples of precise composition are much easier to make than crystalline samples of the same quality and homogeneity.

Figure 3.4[28] compares the theoretical μSR lineshape due to the flux latice in a single crystal uniaxial superconductor, with that in a polycrystal. These lineshapes neglect the effects of demagnetization in the individual superconducting grains, as well as pinning effects which would distort the flux lattice. The sharp features in the lineshapes correspond to the Van Hove singularities in the magnetic density of states. For applied fields$\ll H_{C2}$, the second moment of each distribution is approximately proportional to $\lambda_\perp^{-2}$.

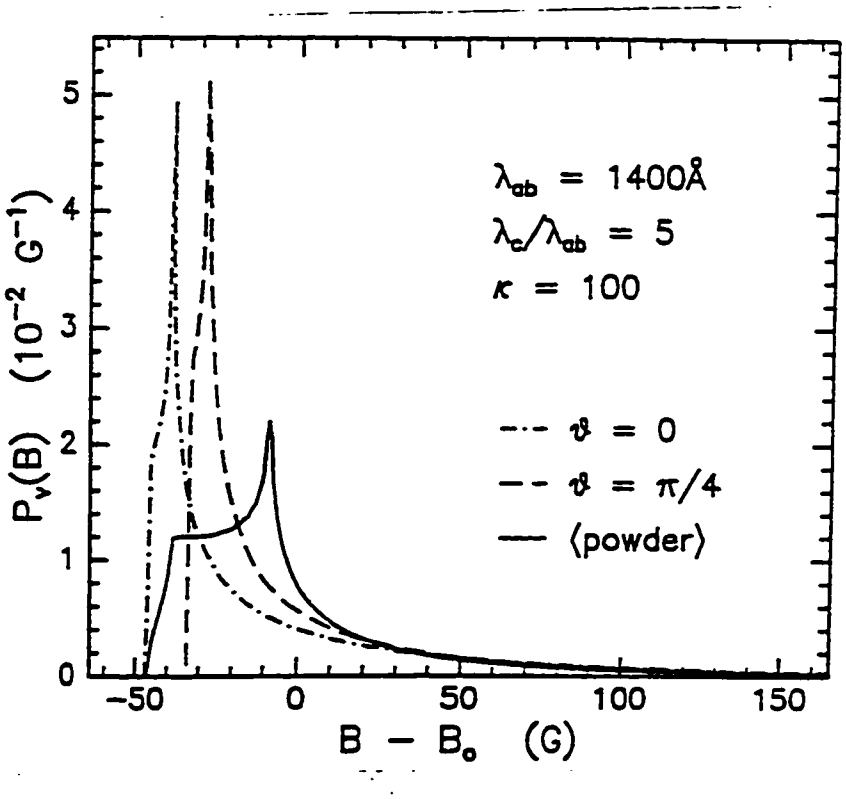

Figure 3.4 Theoretical field distributions for single-crystal and polycrystalline anisotropic superconductor in an aplied field (from ref. [28]).

3.4.2 Nonlocality Effects: "Clean" and "Dirty" Samples

The London models are approximations which assume the locality of the superconducting response to the magnetic field. In reality, the response of the superconductor to an applied vector potential is always nonlocal. The response has the Pippard form[29]:

$$\vec{J}(\vec{r}) = \frac{-3c}{4\pi\xi_0\lambda_L^2}\int \frac{\vec{A}(\vec{r})\cdot(\vec{r}-\vec{r'})(\vec{r}-\vec{r'})}{\mid \vec{r}-\vec{r'} \mid^4}\exp(-\mid \vec{r}-\vec{r'} \mid /\xi)d\vec{r'}.$$

Here ξ_0 is the BCS coherence length of the pure material, and

$$1/\xi = 1/\xi_0 + 1/l,$$

where l is the mean free path of an electron. The idealized range of the nonlocal response is ξ_0; when additional scattering occurs, the response is attenuated and the effective coherence length becomes smaller. In a type-II superconductor with $\lambda_L \gg \xi$, $\vec{A}$ will be approximately constant over the range of the integration. In this case, when $\xi = \xi_0$, one recovers the London result for the response to the field. The effect of the additional scattering attenuation is to further shorten the coherence length, which reduces the value of the integral below the pure material value. The result in this case is

$$\vec{J}(\vec{r}) = \frac{c}{\lambda_L^2} \times \frac{1}{1/\xi_0 + 1/l}.$$

In other words, the scattering modifies the measured penetration depth by a factor $\sqrt{1/\xi_0 + 1/l}$. These considerations will be important in Chapter 7, where Zn impurity effects in the cuprates are discussed.

3.4.3 "Extrinsic" Polycrystalline Distortions: Demagnetization and Pinning Effects

In practice. polycrystalline samples rarely (if ever) manifest the sharp van Hove singularities and the sharp cutoff which characterize the theoretical polycrystalline lineshape. In actual polycrystals and ceramics, the theoretical lineshape is convolved with disorder due to local pinning of the flux lattice, the differing demagnetization fields of the randomly shaped grains, and thermal motions of the fluxoids. These effects will tend to smear the sharp features of the lineshape.

Harshman *et al.*[28] find that the lineshape for cermic $YBa_2Cu_3O_7$ is well described by the theoretical polycrystalline lineshape, when this is convolved with the effects of flux pinning (without the effects of demagnetization). According to Harshman *et al.*: as the superconductor is cooled, the superconducting state becomes more robust, and, in the absence of pinning, more flux would be expelled from the superconductor. In a field-cooling experiment, pinning, will tend to trap flux in the center of the superconducting grains. Fluxoids near the edges of the grains have a greater chance to escape (because there are fewer pinning centers between them and the edge of the grain). This combination of circumstances leads to a distribution in the local density of fluxoids, an increasing rarefaction of the flux lattice as the edge of the grain is approached. The pining model thereby introduces a third parameter to the lineshape, the average pinning inhomogeneity.

3.5 Fitting Ceramic Data: the Gaussian Approximation

Figure 3.5 shows a typical lineshape in ceramic $La_{1.85}Sr_{0.15}CuO_4$ at low temperature, field-cooled in a transverse field of 1kG. Given the smoothness of the field distribu-

tion (no prominent Van Hove singularities) and the approximate symmetry of the lineshape, I adopt a one-parameter fitting regimen. The ceramic TF-μSR data in this thesis are fit with a simple Gaussian-damped cosine oscillation:

$$A(t) = \exp(-(\sigma t)^2/2) \times \cos(\omega t + \phi).$$

This fits a Gaussian peak to the second moment of the field distribution. In the extreme London limit, the second moment of the field distribution, $\langle \Delta B^2 \rangle \propto \phi_0^2 \lambda_L^{-4}$[30].

This choice of relaxation function is not by any means new–it is the old standard of such experiments on ceramic samples. But, with all of the approximation, how does one know that this method is valid? The answer lies in the degree to which one is measuring extrinsic broadening versus the intrinsic width of the fluxoid field distribution. The combined field distribution, which is the convolution of the two processes, will be controlled by the stronger one. For two convolved Gaussians, this comparison resolves to a comparison of the relative Gaussian widths: the larger width wins. For the fluxoid lineshape, one can compare actual experiments. Values of $\lambda_\perp$ estimated from Gaussian fits to data from ceramic $YBa_2Cu_3O_{6+x}$ compare well to those extracted from fits to the full lineshape for high-quality single crystals[31, 32].

3.6 Measuring Superconductivity by Any Means Necessary: Hysteresis Effects

Sometimes, the presence of fluctuating magnetic moments creates a dynamic relaxation which further broadens the field distribution seen by the muon. To first approximation in the time domain of the actual muon relaxation function, a dynamical relaxation will premultiply the static relaxation function. In practice, the two effects are difficult to separate as the dynamic relaxation becomes large. In such circum-

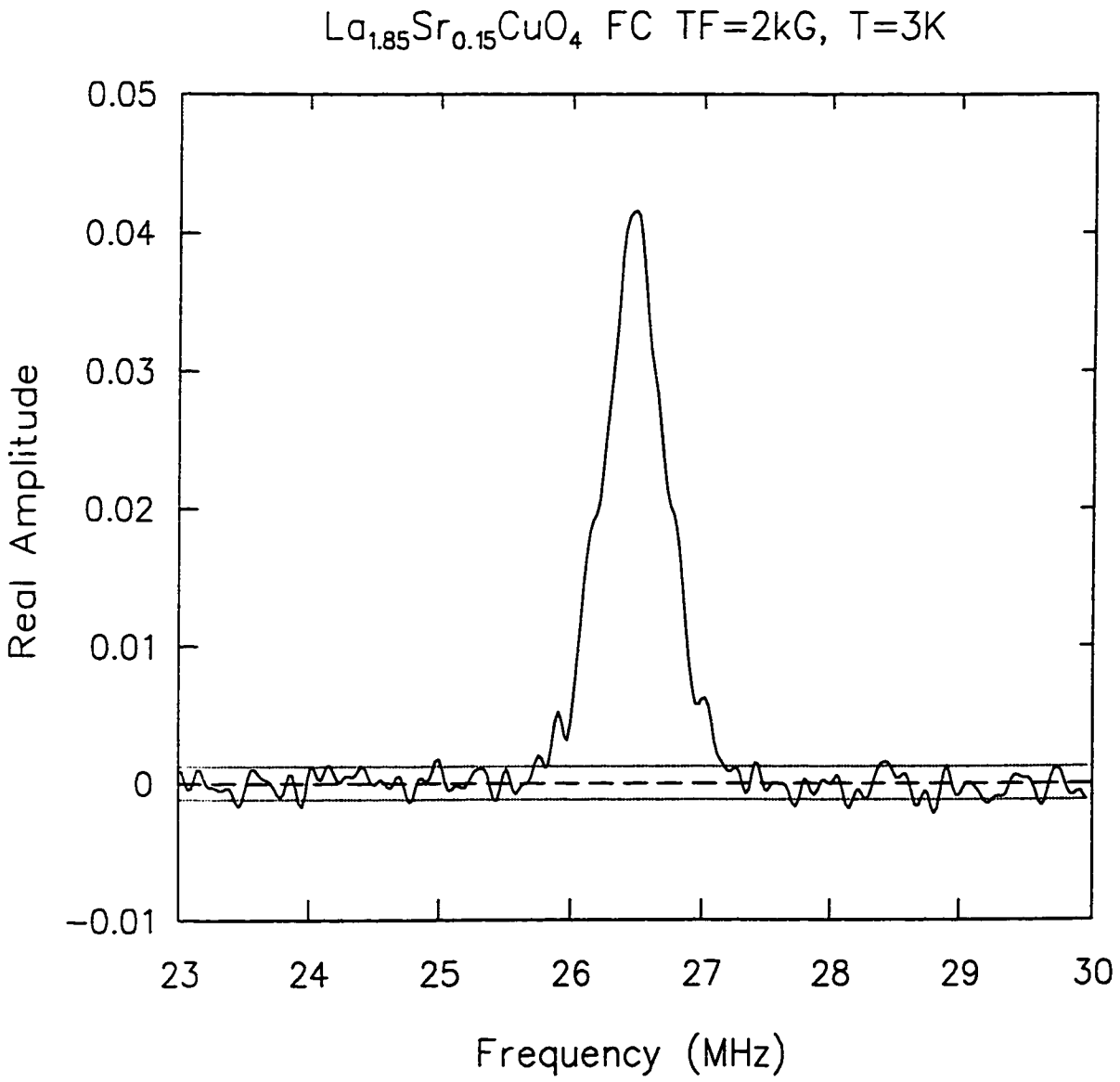

Figure 3.5 Experimental frequency lineshape (Fourier transform of the TF μSR asymmetry spectrum) for a ceramic sample of $La_{1.85}Sr_{0.15}CuO_4$.

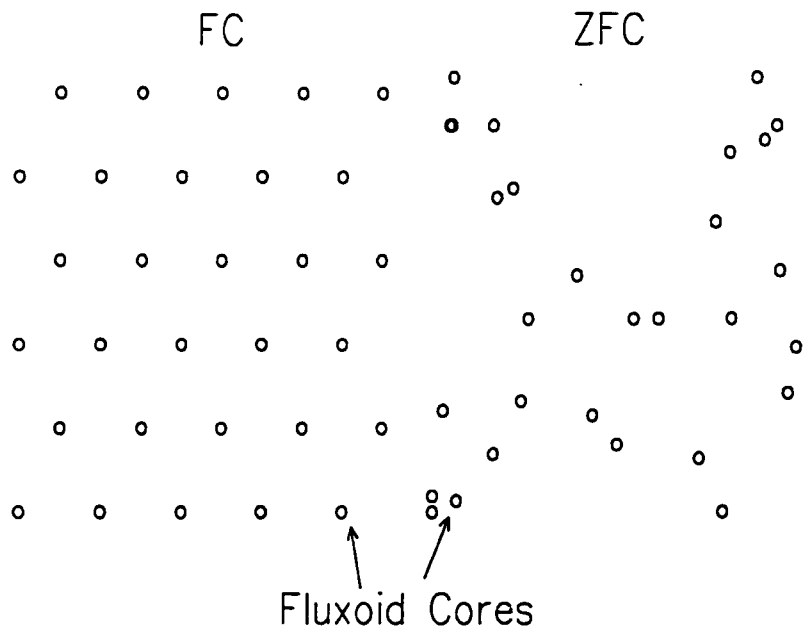

Figure 3.6 Locations of the fluxoid cores in field cooling (FC) and zero-field cooling (ZFC).

stances, to establish that a sample is superconducting at all with μSR, one must rely on irreveribility effects due to fluxoid pinning. Figure 3.6 shows the basic idea. If the sample is in fact supewrconducting, then in the presence of fluxoid pinning, the field-cooled (FC) and zero-field-cooled (ZFC) magnetic field distributions should be easily distinguishable. The second moment of the ZFC distribution should be much greater due to the regions where flux piles up behind pinning barriers, and to those which are surrounded by pinning barriers and so relatively fluxoid-free. Below the characteristic temperature for fluxoid pinning, T_p, the relaxation rates of the muon signals for FC znd ZFC will be markedly different. An example of the magnitude of this effect in TF-μSR is shown in Fig. 3.7.

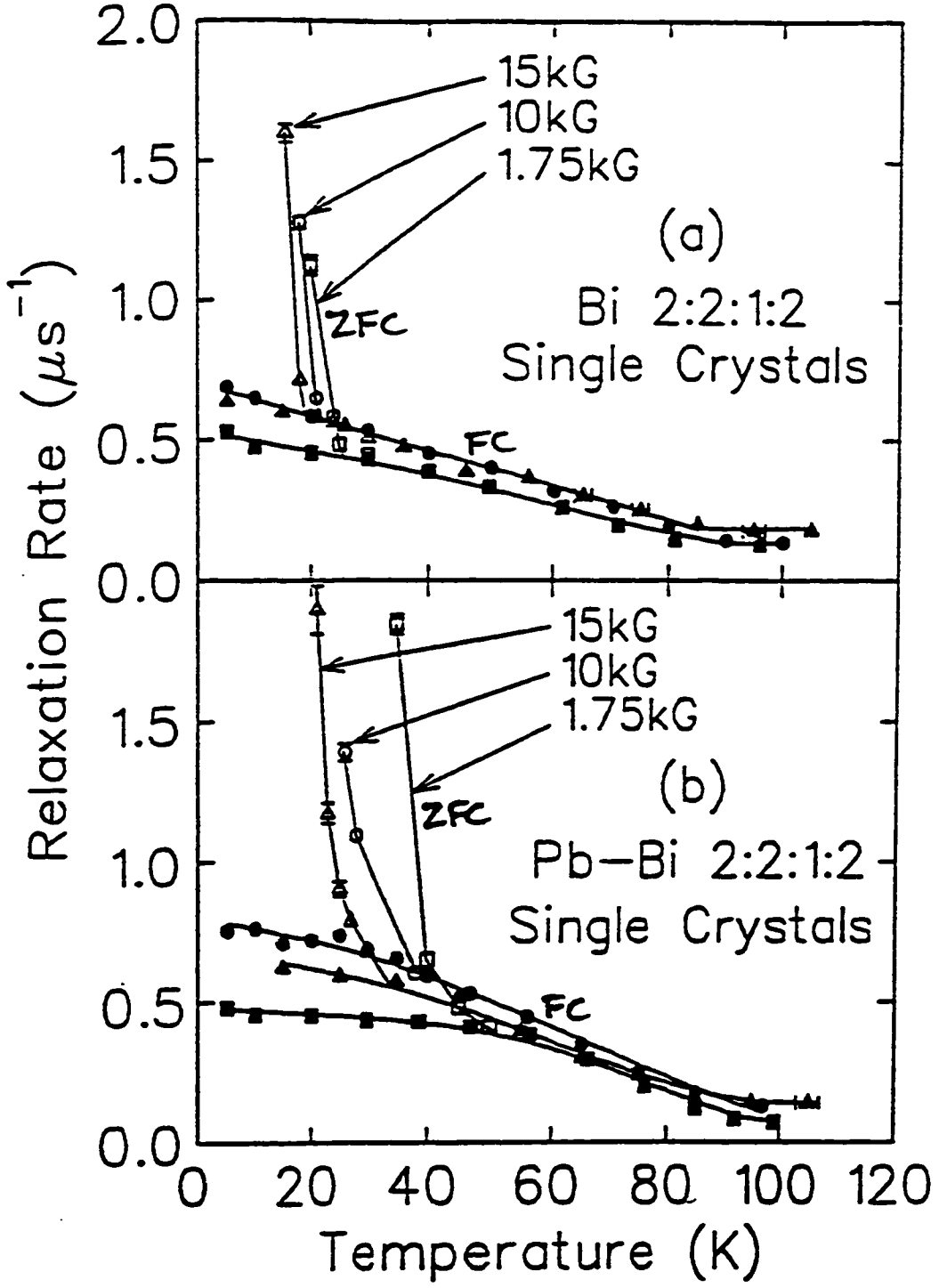

Figure 3.7 Field-cooled versus zero field-cooled TF-μSR relaxation rate in Bi and Pb-Bi based cuprates (from [33]).

Chapter 4

Stripe Correlations in the CuO_2 Plane

4.1 Introduction: Charge/Spin Modulations in the CuO_2 Plane

The underlying motivation of the following experiments is that, an understanding of the role of the antiferromagnetic correlations in the doped states of the CuO_2 plane is an important part of understanding the SC transition in the cuprates. In this chapter, I use μSR techniques to characterize the peculiar magnetic "stripe" order (to be defined below) which was first identified in the "214" materials $La_{1.6-x}Nd_{0.4}Sr_xCuO_4$ (a similar order is known to occur in the isostructural nickelate $LaNi_2O_{4+\delta}$). The interplay between superconductivity and the stripe magnetic order in $La_{1.6-x}Nd_{0.4}Sr_xCuO_4$ forms the subject of the next chapter. Much of the work in chapters 4 and 5 has been accepted for publication in the October, 1998 issue of Phys. Rev. B.

4.1.1 Overview of the 214 Phase Diagrams

The electronic and structural phase diagrams for the materials $La_{2-x}(Ba/Sr)_xCuO_4$ are reproduced in Figs. 4.1 and 4.2. As with all the cuprates, the undoped parent material is an antiferromagnet, with a transition temperature $T_N \approx 300$K. The Cu

spins are coupled by a Cu(3d)-O(2p)-Cu(3d) exchange interaction. Doping (Ba/Sr) at the La site is believed to introduce holes into the CuO_2 plane, which disrupts the exchange interaction quite efficiently. Both $La_{2-x}Ba_xCuO_4$ and $La_{2-x}Sr_xCuO_4$ move through a spin glass-like disordered phase (SG) and eventually become superconducting at dopant concentrations of 0.05 and 0.07, respectively. However, at $x \approx 0.125$ in $La_{2-x}Ba_xCuO_4$ and $x \approx 0.115$ in $La_{2-x}Sr_xCuO_4$, superconductivity is suppressed and magnetic order reemerges. This anomaly is known as the "1/8 effect"[34, 35, 36, 37].

In addition to these electronic transitions, the 214 materials also have a rich structural phase diagram. At high temperatures/low dopant concentrations, $La_{2-x}(Ba/Sr)_xCuO_4$ is tetragonal. As the temperature is lowered and x changes, the CuO_6 octahedra distort about the (110) or $(1\bar{1}0)$ axes[34]. The structural ground state depends sensitively on the size of the dopant ion. The three possibilities generally observed may be decomposed into different superpositions of these two distortions. They are: (1)low-temperature orthorhombic (LTO), (2)low-temperature tetragonal (LTT), and (3) the intermediate Pccn phase. Figure 4.3 shows the different distortions and Fig. 4.4 shows the important wrinkling effects they have on the CuO_2 plane.

4.1.2 Stripe Instabilities in 214

A series of neutron scattering studies have indicated that near-AF spin correlations pervade the SC state of $La_{2-x}Sr_xCuO_4$, for $x < 0.20$. The dynamical magnetic susceptibility shows excitations at wavevectors split around the planar AF wavevector ($(\pi/a, \pi/a)$ in inverse lattice units, where a is the spacing between two Cu in the planes). Neutron scattering techniques have shown the closely related material $La_{1.6-x}Nd_{0.4}Sr_xCuO_4$ to order magnetically for $x \sim 0.125 - 0.15$, while T_C is

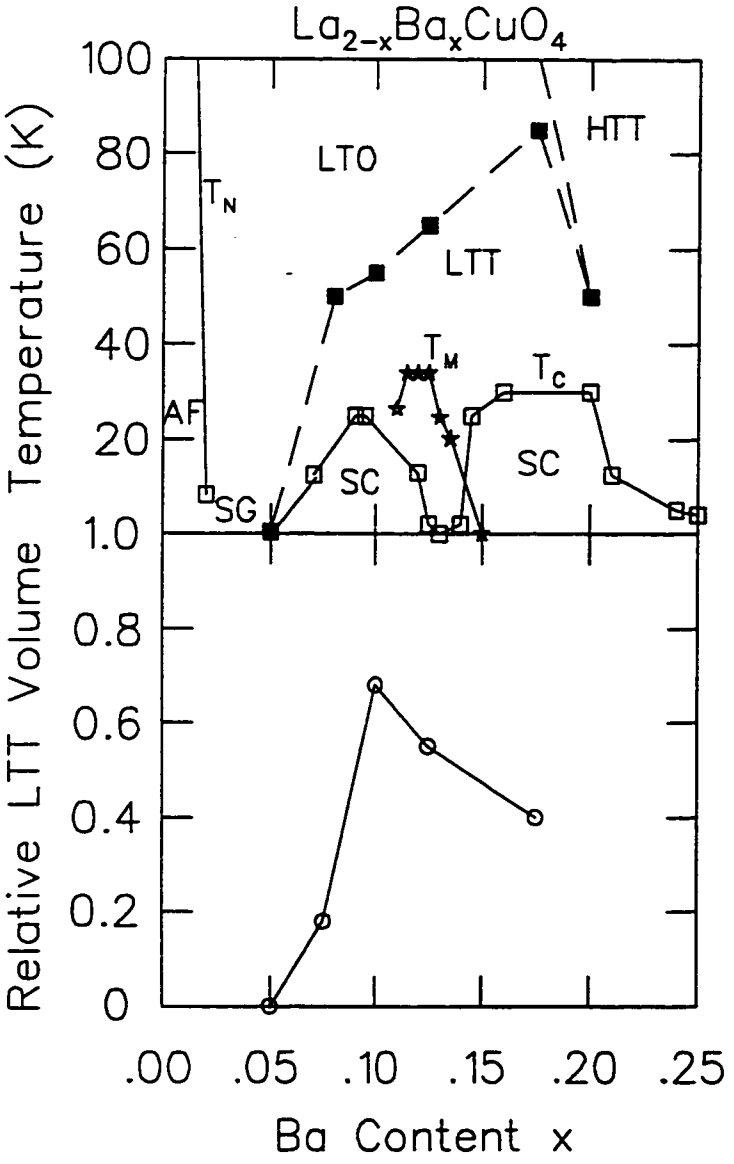

Figure 4.1 Electronic and structural phase diagrams as a function of temperature and doping x for $La_{2-x}Ba_xCuO_4$[34, 35, 36]. The electronic phases are indicated by solid lines connecting the open squares. These are antiferromagnetic (AF), cluster-spin-glass (SG) and superconductor (SC). The structural phases are indicated by dashed lines connecting the filled squares.

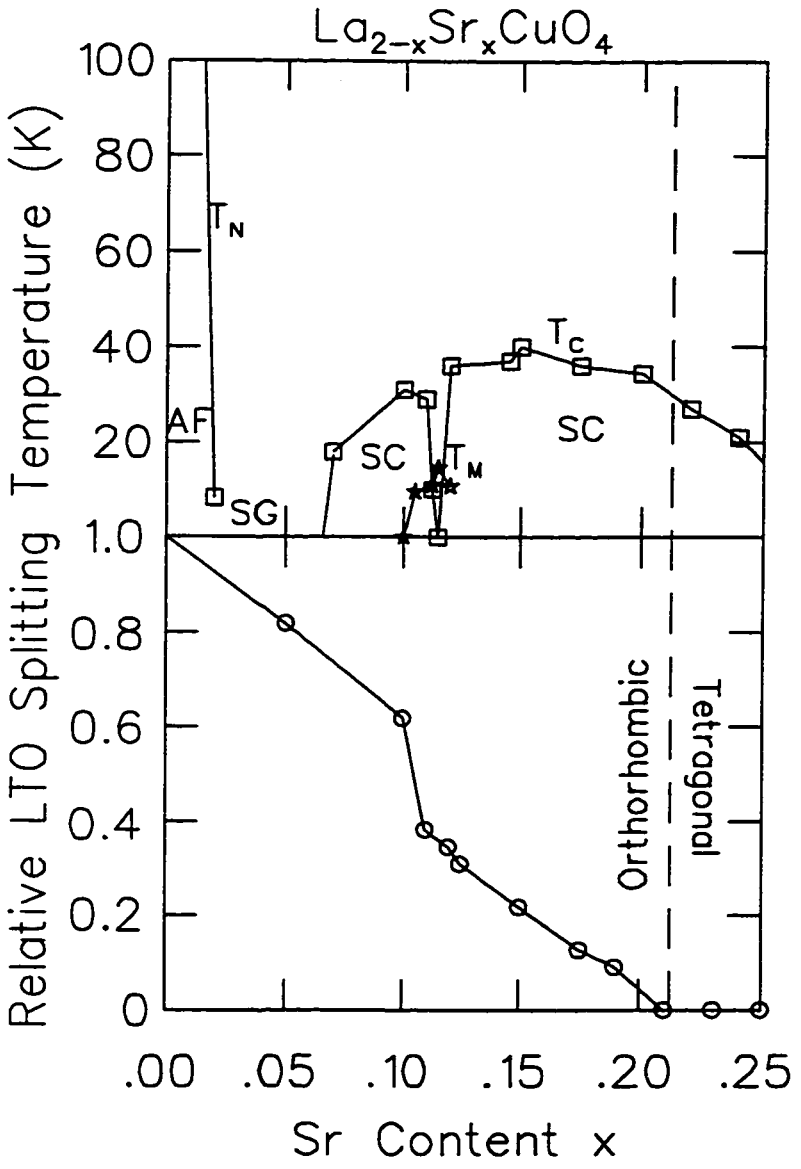

Figure 4.2 Electronic and structural phases as a function of temperature and doping x for $La_{2-x}Sr_xCuO_4$[36, 38, 39].

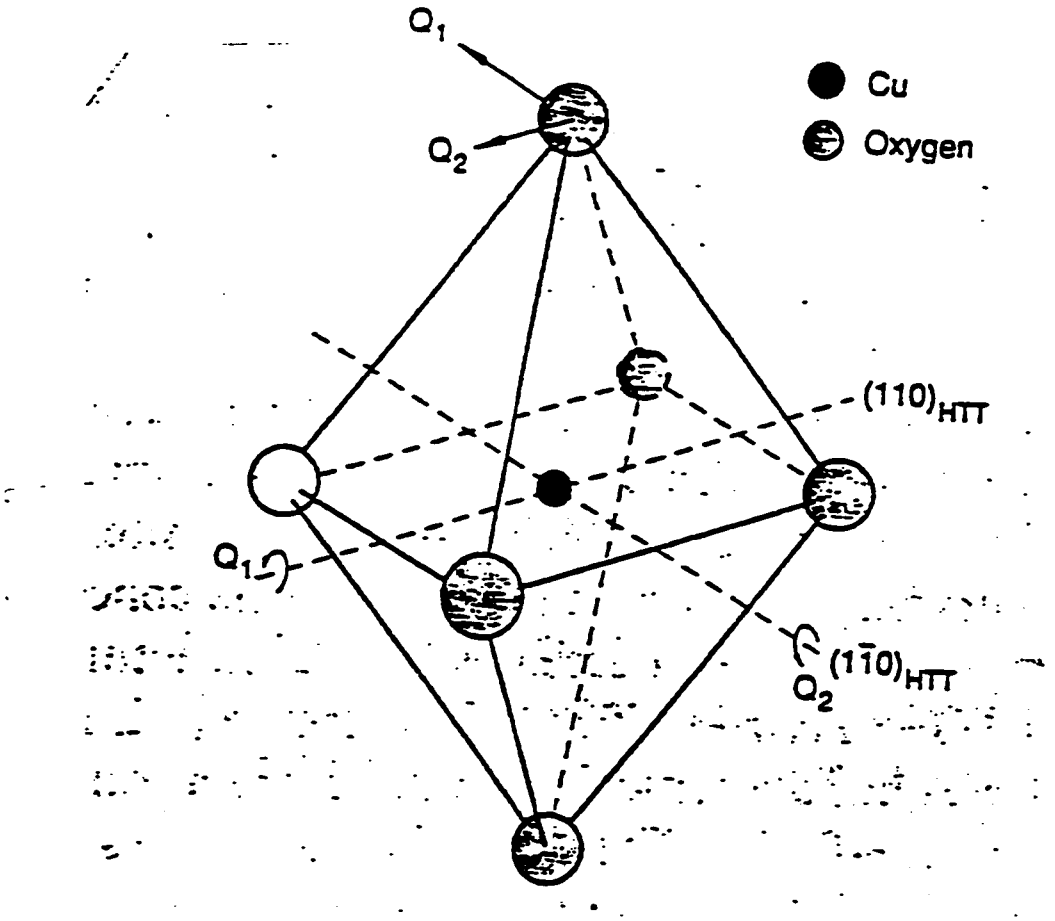

Figure 4.3 Distortions of the CuO_6 octahedra in the 214 systems (from [40].

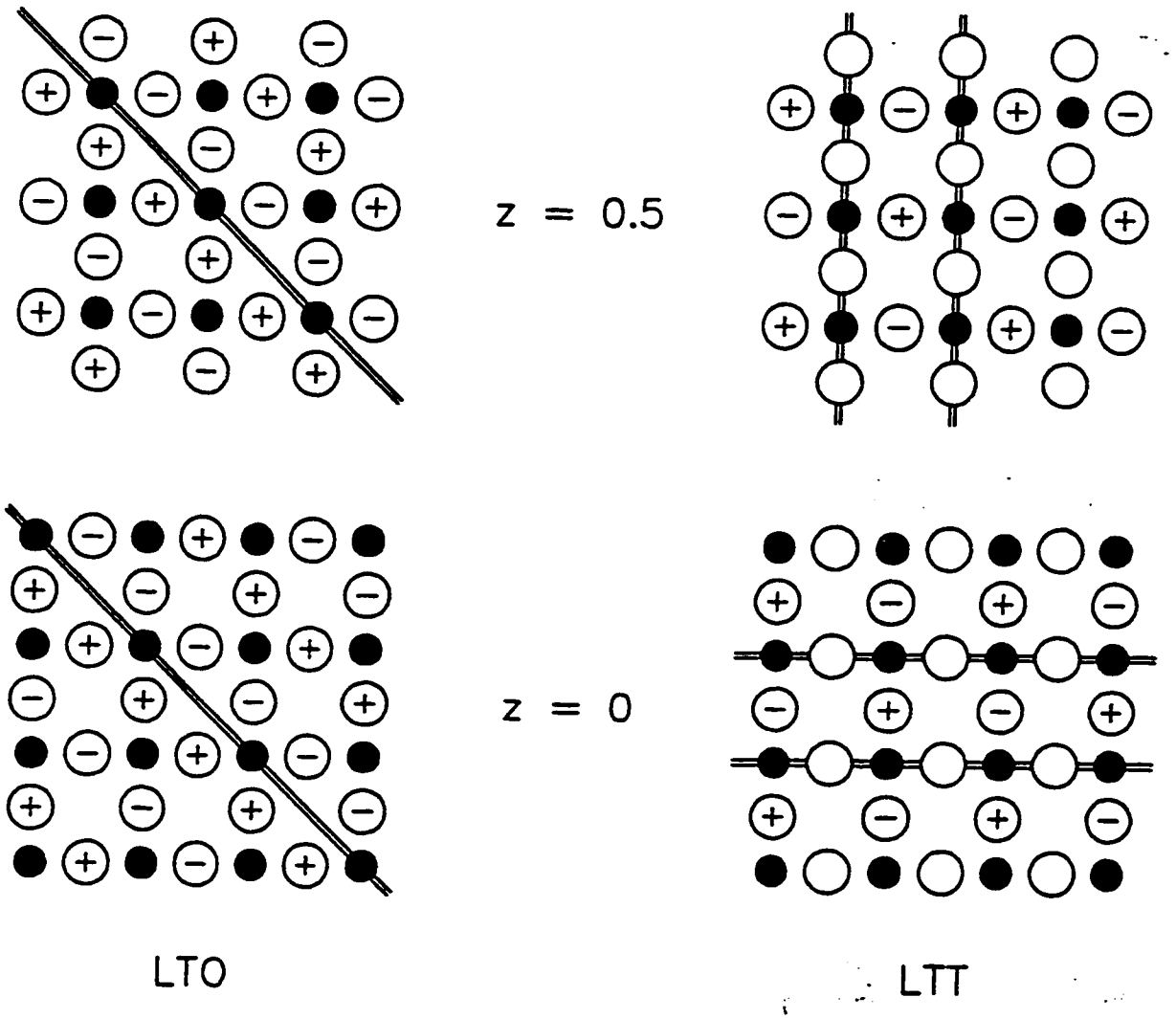

Figure 4.4 Furrowing of the CuO_2 plane in the LTO and LTT phases (from [41]).

suppressed in this doping range. The electronic and structural phase diagrams of $La_{1.6-x}Nd_{0.4}Sr_xCuO_4$ are reproduced in Fig. 4.5. The wavevector dependence of the magnetic order in $La_{1.6-x}Nd_{0.4}Sr_xCuO_4$ also shows peaks split about the AF peak. In addition, weak splitting of the nuclear Bragg peaks suggested that this magnetic order was coupled to a modulation of the charge density in the CuO_2 plane. A schematic of the neutron scattering results for $La_{1.475}Nd_{0.4}Sr_{0.125}CuO_4$ is shown in Fig. 4.6.

Tranquada and coworkers proposed a stripe-modulated structure to explain the observed modulations of the charge and spin modulations in $La_{1.475}Nd_{0.4}Sr_{0.125}CuO_4$ as the result of pinning–of the very same dynamic modulations seen in $La_{2-x}Sr_xCuO_4$–on lattice distortions stabilized by the Nd substitution. This stripe model is sketched in Fig. 4.7. The direction of the stripes in each CuO_2 plane follows the furrows created by the LTT distortion. Because the furrows rotate by $\pi/2$ between CuO_2 layers, the one-dimensional modulation leads to two sets of satellite peaks, *i. e.* the four satellites seen in the experiment correspond to two orthogonal modulations. The neutron scattering intensity for the magnetic peaks is largely "2-dimensional," that is, it does not resolve into Bragg peaks for momentum transfers perpendicular to the CuO_2 planes. In the stripe model, this fact results from the degeneracy of the modulation phase between nearest-neighbor planes, and the near-degeneracy of body-centered tetragonal AF order. The interplanar couplings will be randomized if the charge modulations are not correlated between nearest-neighbor planes.

The stripe model is not the only one which would generate the observed satellite peaks for momentum transfers in the plane. A two-dimensional "grid" modulation would mimic the stripe results for planar momentum transfers. However, a grid modulation would possibly lead to more "3-dimensional" correlations of the spin structure, because the lowest-energy state would be for the interstices of one grid to

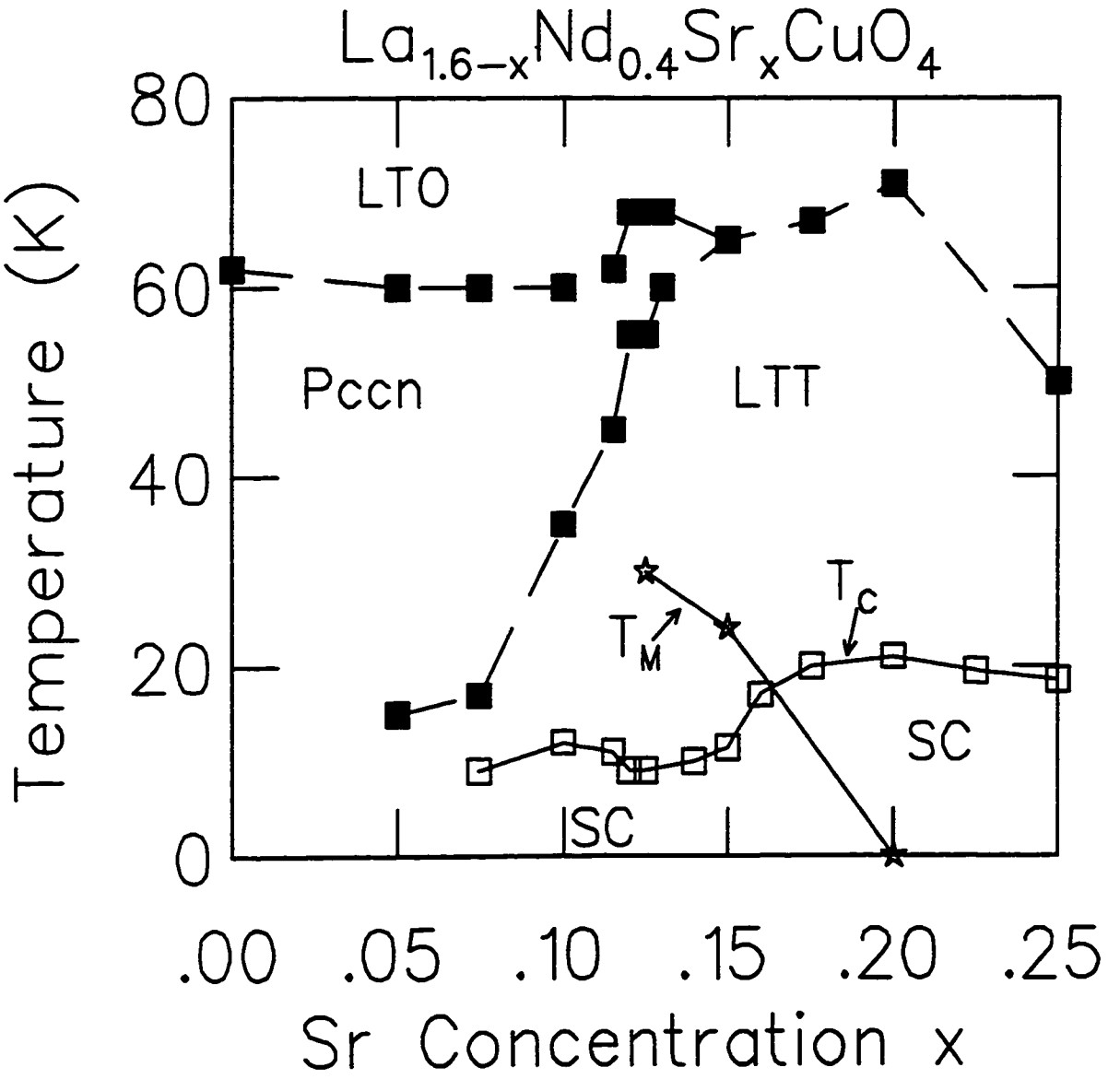

Figure 4.5 Electronic and structural phases of $La_{1.6-x}Nd_{0.4}Sr_xCuO_4$, as a function of x and temperature[42, 40, 43, 44].

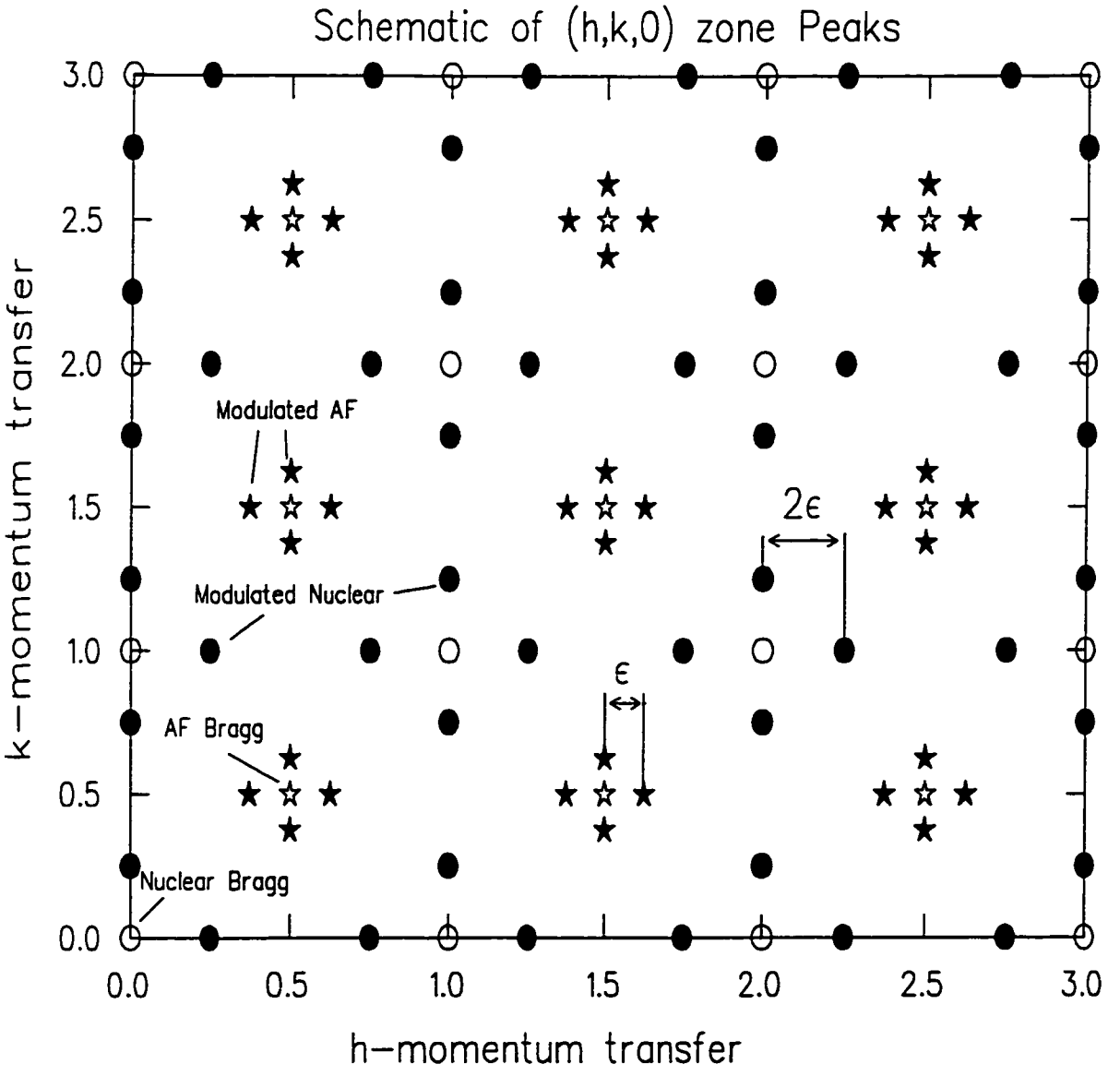

Figure 4.6 A schematic of the neutron scattering results for $La_{1.6-x}Nd_{0.4}Sr_xCuO_4$[45].

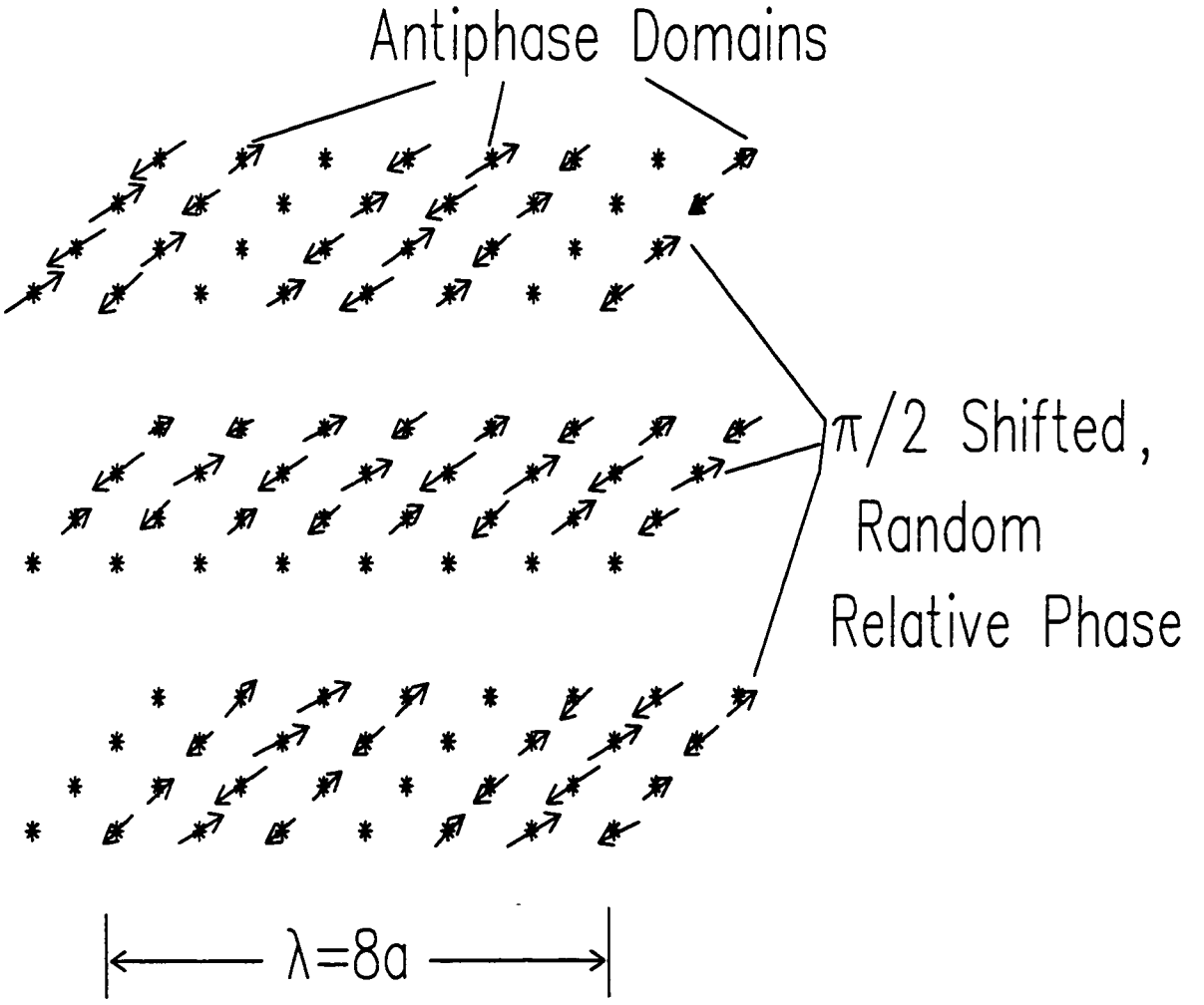

Figure 4.7 The proposed modulated charge/magnetic order inferred from the neutron scattering measurements[45].

lie atop the holes of the grid below, leading to phase locking between the nearest neighbor planes. Furthermore, the LTT distortion leads to a preferred axis in the CuO_2 plane which seems conducive to pinning stripelike dynamical modulations. X-ray diffraction measurements[46] show significant correlations between the charge modulations in next-nearest-neighbor planes, where the stripes should line up, but show little correlation between nearest-neighbor planes.

There is no theoretical consensus on the mechanism of the stripe modulations. Early explanations suggested that the magnetic modulations resulted from the effects of a nearly nested Fermi surface and the creation of a spin-density wave (SDW)[47]. However, the primacy of the charge ordering seems to argue against this picture. Furthermore, the observed modulation wavevector does not seem to be a spanning vector of the Fermi surface [48].

A different approach is based upon the tendency of doped neutral holes to phase segregate in a strongly AF background [48]. Phase segregation of doped neutral holes would minimize the total number of frustrated antiferromagnetic bonds in the underlying lattice. Minimizing the number of frustrated bonds minimizes the overall energy. Hence, doped neutral holes in an antiferromagnetic background with frustration effects tend to clump together. In this picture, Coulomb repulsion would frustrate this spontaneous phase segregation, leading to dynamical correlations in the charge and spin density in the SC state. According to Emery *et al.*, the doped holes in the SC state try to form soliton domain walls ("topological defects") which bound antiphase AF regions. Given the proper lattice distortions, the solitons will also become pinned.

Unfortunately, no recent theory of the stripe modulation carries with it a conclusive test of its validity for μSR, for example, in the size of the ordered moment, or

in the ordering temperature. This chapter presents a more detailed analysis of the data in references [35, 37], along with newer μSR data from $La_{1.875}Ba_{0.125-x}Sr_xCuO_4$, $La_{1.45}Nd_{0.4}Sr_{0.15}CuO_4$, and $La_{1.4}Nd_{0.4}Sr_{0.2}CuO_4$ systems. The techniques of zero-field (ZF) μSR eludicate the nature of the magnetic order in a large variety of Ba-doped "1/8" and Sr-doped samples which contain Nd. I extract the magnetic ordering temperature T_N, and estimate the ordered Cu moment S_0. These results suggest that the behavior of the Cu spins in all of these compounds is almost certainly the same, the only differences being due to secondary ordering of the Nd moments. In terms of the ratio of the ordered moment to the scaled transition temperature T_N/J_{AF}, where J_{AF} is the largest coupling constant in the system, previous μSR studies [49] have established the different qualitative behaviors of quasi 2-dimensional systems of S=1/2 ions (like the cuprate antiferromagnets) and quasi 1-dimensional systems (like the S=1/2 spin chain compounds and the 3-leg "ladder" cuprate). I compare the stripe materials to previously measured low-dimensional cuprate antiferromagnets.

4.2 ZF-μSR Asymmetry Spectra

Between 1990 and 1997, our group measured time differential ZF-μSR spectra at the M13 and M15 surface muon channels of TRIUMF. The samples were affixed to pure Ag backings with Apiezon-N grease, then mounted in the tail of a standard Janis gas-flow cryostat with a minimum temperature of 2K, or a cold-finger continuous-flow cryostat with a minimum temperature of 1.3K. Once the stray fields at the samples were minimized, muons landing in the backings or in the Ag cryostat tails did not relax noticeably over the time range studied. Because the samples under study do posess a significant nuclear magnetic moment, we are able to distinguish those muons which land in the sample even in the absence of electronic magnetic order. However,

because in some setups the decay positrons due to muons landing in the Ag backing were not excluded from the histograms, the overall corrected asymmetry due to the sample alone had an arbitrary amplitude, which depended on the overall sample size with respect to the beam spot.

4.2.1 Ba-and Nd,Ba-doped Samples

One purpose of these experiments is to determine whether the "1/8" effect and the stripe magnetic order are the same phenomenon. The Ba-doped samples allow a calibration of the stripe order against the "1/8" magnetic order. Substituting the Ba-doped "1/8" samples with Nd allows us to compare the effects of Ba and Sr doping under otherwise identical conditions.

The ceramic $La_{1.875}Ba_{0.125}CuO_4$ samples showed spontaneous precession below $T_N \approx 30$K. indicating magnetic order of the Cu spins. The ceramic $La_{1.475}Nd_{0.4}Ba_{0.125}CuO_4$ showed a similar magnetic field order with the same T_N. Figure 4.8 shows typical spectra from samples of each type. The spectra from both Ba-doped systems show a damped oscillation and a relaxing $A_{||}$ component. It seems highly likely from Fig. 4.8 that substituting Nd at the La site in $La_{1.875}Ba_{0.125}CuO_4$ does not significantly affect the Cu order. The solid curves in Fig. 4.8 are fits to the phenomenological form

$$A(t) = A_\perp \times J_0(2\pi\nu t) \times \exp(-\Lambda_\perp t^{\beta_\perp}) + A_{||} \times \exp(-\Lambda_{||} t^{\beta_{||}}).$$

Here J_0 is the zeroth order Bessel function of the first kind. Some of the $La_{1.875}Ba_{0.125}CuO_4$ data had been fit previously with a damped cosine function [35, 37]. The cosine fits tended to yield values of the initial phase of the muon asymmetry which were inconsistent with the known initial polarization of the muon beam. Some possible implications of the Bessel form for the asymmetry function are discussed below. The

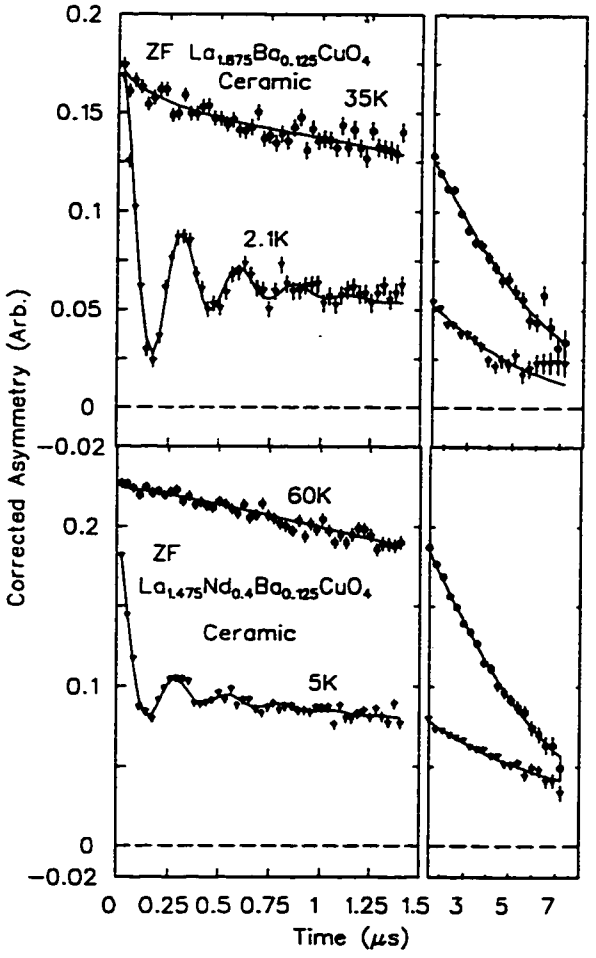

Figure 4.8 Representative asymmetry spectra and fits (solid curves) for ceramic samples of $La_{1.875}Ba_{0.125}CuO_4$ and $La_{1.475}Nd_{0.4}Ba_{0.125}CuO_4$.

value of the extracted frequency does not depend strongly on which of the two functions (Bessel or cosine) is used, because the first few zeros of the functions have the same spacing to within 1%. The observed $\nu \approx 3.5$ MHz corresponds to an average $B_{local} \approx 220G$ at the muon site.

4.2.2 Ba+Sr-doped Samples

Ceramic samples of $La_{1.875}Ba_{0.1}Sr_{0.025}CuO_4$ and $La_{1.875}Ba_{0.06}Sr_{0.0625}CuO_4$ showed two distinct magnetic volume fractions with different magnetic behaviors. Below 30K, and down to 5K, part of these samples showed a magnetic order with the same frequency as in the single-dopant samples, while the rest of the sample relaxed with the slow Kubo-Toyabe function typical to systems of small disordered moments. Similar instances of distinct magnetic regions in mixed-dopant ceramic samples have been reported previously by Lappas *et al.*[50], who attributed the reduced ordered fraction to the decreased pinning of the stripe order as less of the lattice undergoes the LTO→LTT transition.

4.2.3 Nd,Sr-doped Samples

Figure 4.9 shows representative spectra from crystal samples of $La_{1.475}Nd_{0.4}Sr_{0.125}CuO_4$ and $La_{1.45}Nd_{0.4}Sr_{0.15}CuO_4$. We also measured several ceramic samples at the $x = 0.125$ composition which showed the same general behavior as the crystal. For $x = 0.125$ T_N and ν at $5K < T < 10K$ are nearly identical to that seen in the Ba-doped samples. For $x = 0.15$, T_N is slightly lower, but the saturating ν remains unchanged. There were two significant differences between the Sr-doped and Ba-doped samples without Nd. At $T < 5$K, both ν and $\Lambda_\perp$ began to increase dramatically.The 3.5K

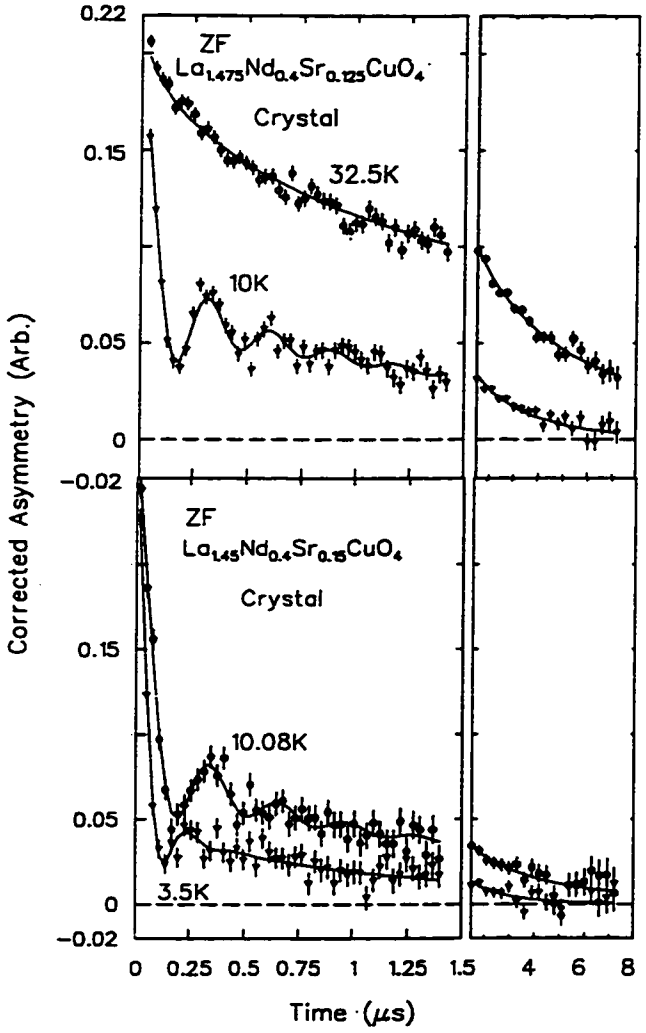

Figure 4.9 Representative asymmetry spectra and fits (solid curves) for crystals of $La_{1.475}Nd_{0.4}Sr_{0.125}CuO_4$ and $La_{1.45}Nd_{0.4}Sr_{0.15}CuO_4$.

spectrum for the $x = 0.15$ sample in Fig. 5 shows this effect. As Fig. 4.10 shows, the LF = 2kG measurements of $La_{1.475}Nd_{0.4}Sr_{0.125}CuO_4$ crystal reveal dynamic relaxation which is almost completely absent from the $La_{1.875}Ba_{0.125}CuO_4$ ceramic. The neutron scattering analysis of Tranquada *et al.* [42] suggests that, at $T \approx 5$K, the Nd ions begin to order following the Cu order, while the Cu moments themselves begin to cant out of the plane. The low-temperature enhancement of the relaxation and the frequency are consistent with this picture. Because the Nd spins are only randomly present in the lattice, the Nd ordering should increase the relaxation rate, but should not coherently add to the measured precession frequency. Figure 4.11 shows the relaxation parameters Λ and β for the $La_{1.475}Nd_{0.4}Sr_{0.125}CuO_4$ crystal, as functions of temperature. Λ increases below 5K, suggesting that the temperature scale for the moments producing the relaxation differs markedly from T_N. β decreases to 0.45 at low temperatures, suggesting that the fluctuating magnetic field is inhomogeneous, as expected from the random placement of the Nd ions.

The rotation of the Cu spins out of the plane should change both the direction and the magnitude of $\vec{B}_{\text{local}}$. This rotation of the magnetic field may be inferred from comparison of the $A_\perp/A_{||}$ between single-crystal and ceramic samples of $La_{1.475}Nd_{0.4}Sr_{0.125}CuO_4$ in Fig. 4.12. If there were no reorientation of the moments, then these temperature dependences should have been identical. The oscillating asymmetry component in the crystal sample is relatively enhanced below 10K, indicating that the field at the muon site may rotate out of the plane as the temperature is lowered. However, it is difficult to precisely define the field direction in the crystal without a normalizing measurement of the total ordered volume of the sample. The most reliable such measurement would be to mill the sample into a powder, and measure the powder-averaged oscillating component. Unfortunately, time constraints

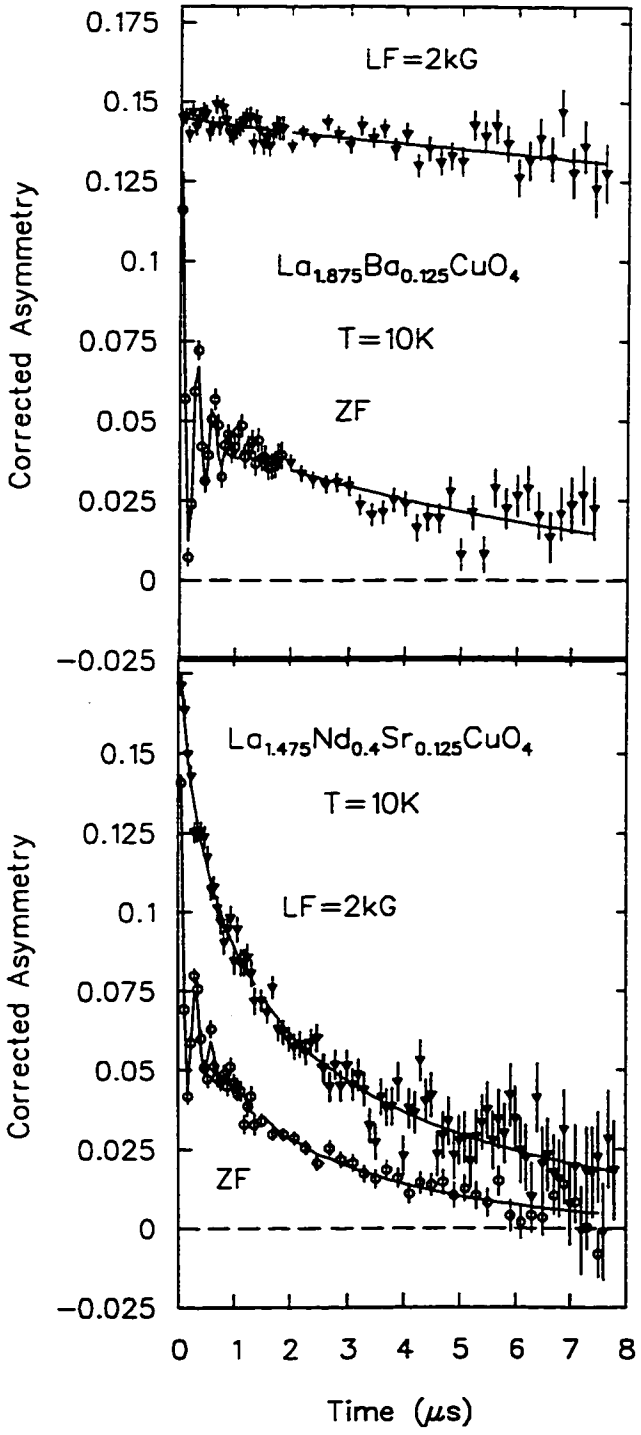

Figure 4.10 Comparative decoupling at T = 10K and LF=2kG for (top) Ba-doped ceramic and (bottom) Sr-doped crystal.

and the relative rarity of large single crystals prevented such a measurement on this sample.

4.2.4 Summary of Measurements on the x $\leq$ 0.15 Samples

Figure 4.13 shows ν as a function of temperature for the various samples with $x \leq 0.15$. T_N for all of these samples is approximately the same regardless of the presence of Nd or whether the sample is doped with Ba, Sr, or both. Exclusive of the $T < 5K$ enhancement in the samples with Nd, ν saturates at the same value of 3.5 MHz. This frequency results from the ordered Cu moment. Ignoring the low-temperature effects of the Nd-Cu coupling, we identify this frequency as the intrinsic magnetization of the Cu ordering in these systems. We may roughly estimate the size of the ordered moment by assuming that the muon site is unchanged from that in undoped La_2CuO_4. (The reasonableness of this assumption is discussed below in the section on the muon site.) In this case, the ratio of the ordered moment sizes should approximately equal the ratio of the frequencies. For La_2CuO_4, Uemura *et al.* found $\nu \rightarrow 5.8$MHz at low temperatures, for an ordered moment of approximately $0.5\mu_B$. Therefore by this method, $S_0 \approx 0.3\mu_B$. The more detailed calculation presented in the discussion below, which takes into account the modulated antiphase spin structure seen in $La_{1.475}Nd_{0.4}Sr_{0.125}CuO_4$ and $La_{1.45}Nd_{0.4}Sr_{0.15}CuO_4$[51], gives nearly the same result.

4.2.5 x = 0.2 Samples

How far up the doping scale do the stripe effects persist? Tranquada *et al.*[51] find evidence of static spin correlations even in a single crystal of $La_{1.4}Nd_{0.4}Sr_{0.2}CuO_4$. In

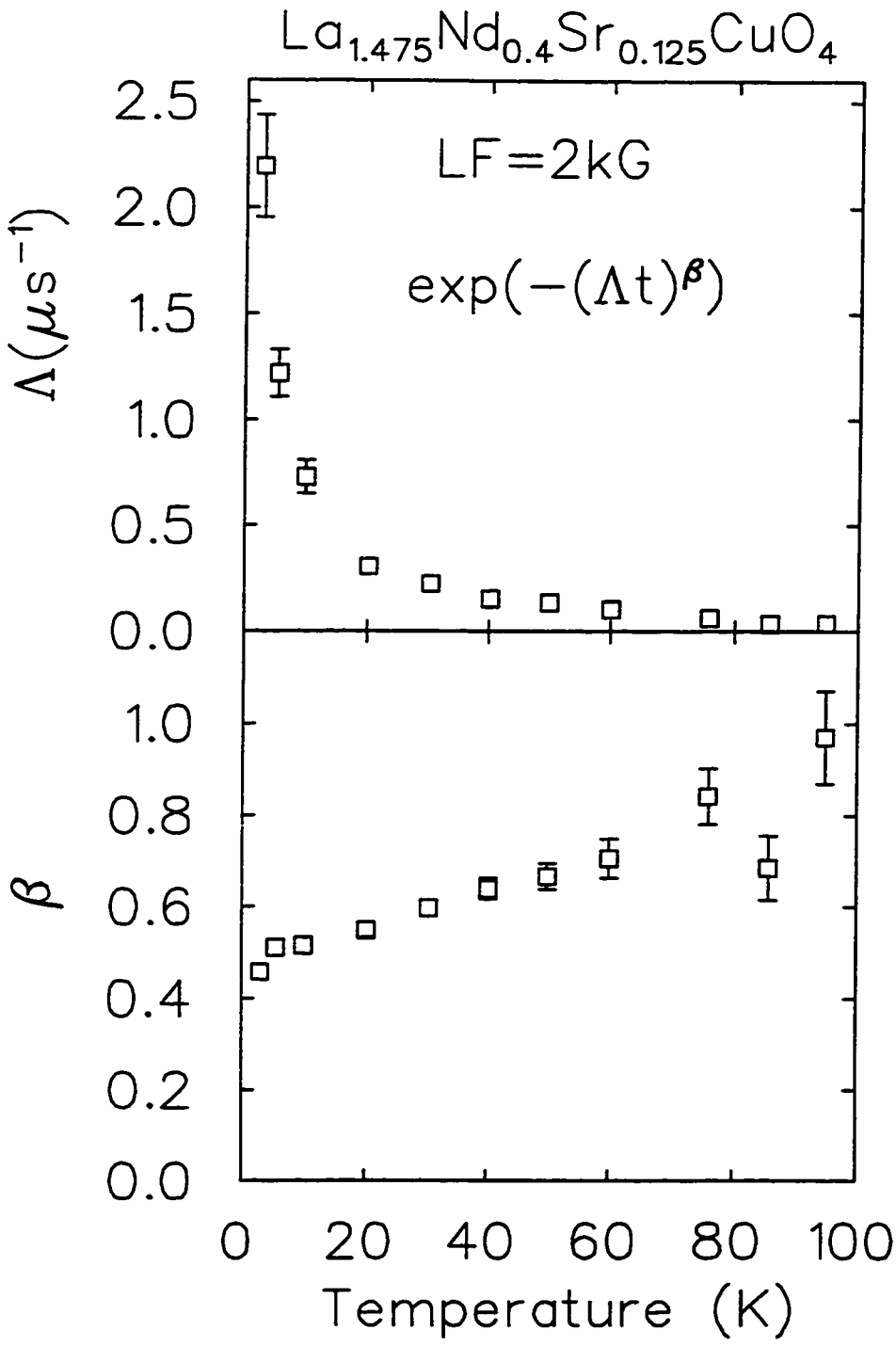

Figure 4.11 Temperature dependences of (top) relaxation power Λ and (bottom) relaxation exponent β for $La_{1.475}Nd_{0.4}Sr_{0.125}CuO_4$ crystal.

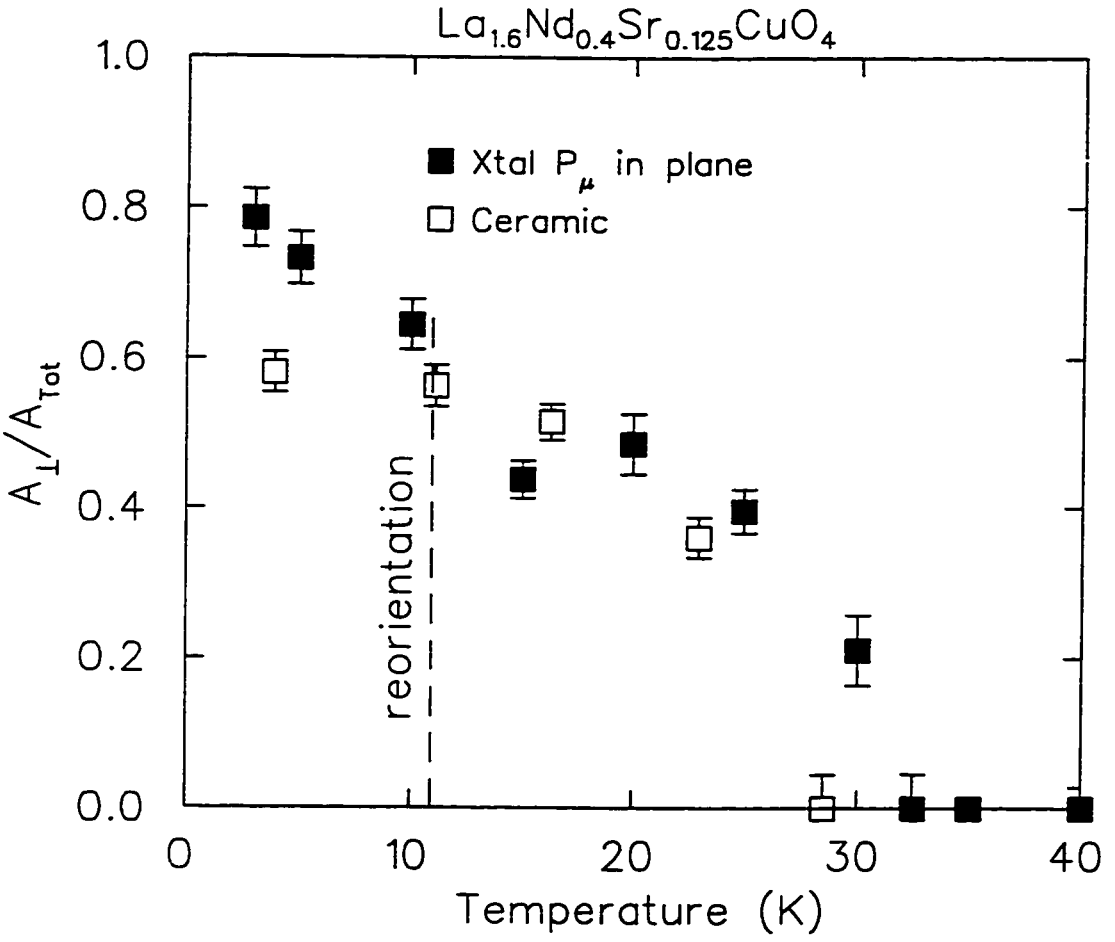

Figure 4.12 Comparison of the temperature dependence of the $A_{\perp}$ asymmetry fraction between ceramic and crystal samples of $La_{1.475}Nd_{0.4}Sr_{0.125}CuO_4$.

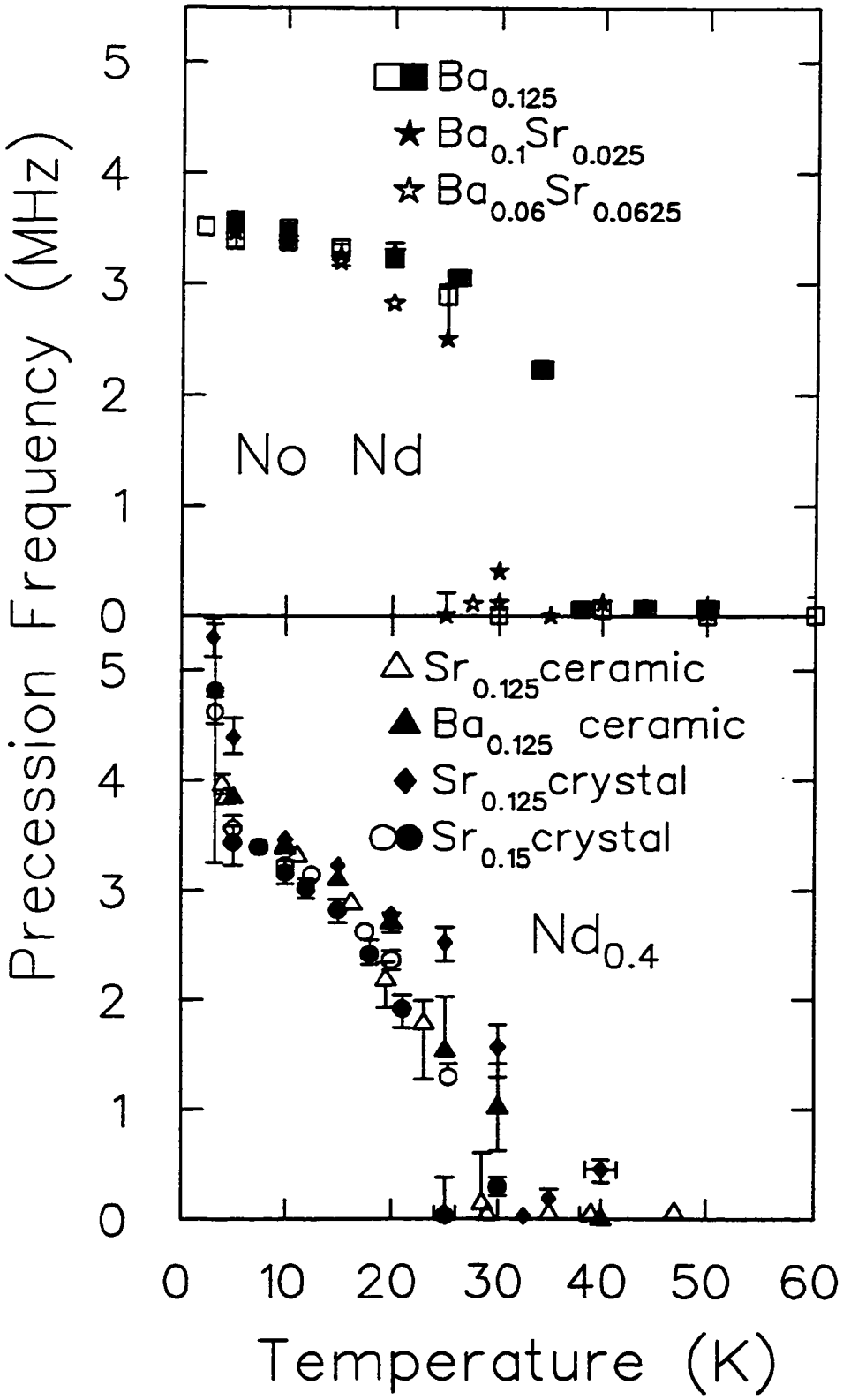

Figure 4.13 Temperature dependence of the Bessel frequency extracted from fits.

contrast with these results, ZF-μSR measurements on the $La_{1.4}Nd_{0.4}Sr_{0.2}CuO_4$ crystal revealed no coherent magnetic order. The low-temperature μSR spectrum, shown in Fig. 4.14, shows no static recovery, which implies that the magnetic fields in this sample remained dynamic down to 1.88K. The initial relaxation is four times as fast as the frequency due to the ordered Cu moments in the $x = 0.125$ and $x = 0.15$ samples. LF measurements on a ceramic sample of the same composition show that the fast relaxation begins to decouple at 1 kG. In light of the neutron scattering data which suggest a static order of the Cu spins, it seems likely that this fast relaxation is due to the combined quasistatic ordering of Nd and Cu moments, and that in the $x = 0.20$ samples, in contrast to the lower-doping samples, the temperature scales of the Cu and Nd spin systems are not well separated.

4.3 Discussion of the Magnetic Order

Because of the similarities among the data from all of the samples with $x = 0.125$ and $x = 0.15$, we analyze the magnetic order in the same generic picture of antiphase stripe magnetic order with little correlation between different CuO_2 planes. It is important to note, however, that there is as yet no other experimental evidence for such stripe magnetism in the $La_{1.875}Ba_{0.125}CuO_4$ system. Large single crystal samples appropriate for neutron scattering measurements have not been available. This is unfortunate because only the $La_{1.875}Ba_{0.125}CuO_4$ system is free of the broadening due to the Nd dynamics; nevertheless, we proceed on the μSR evidence that the two examples of magnetic order are of similar origin.

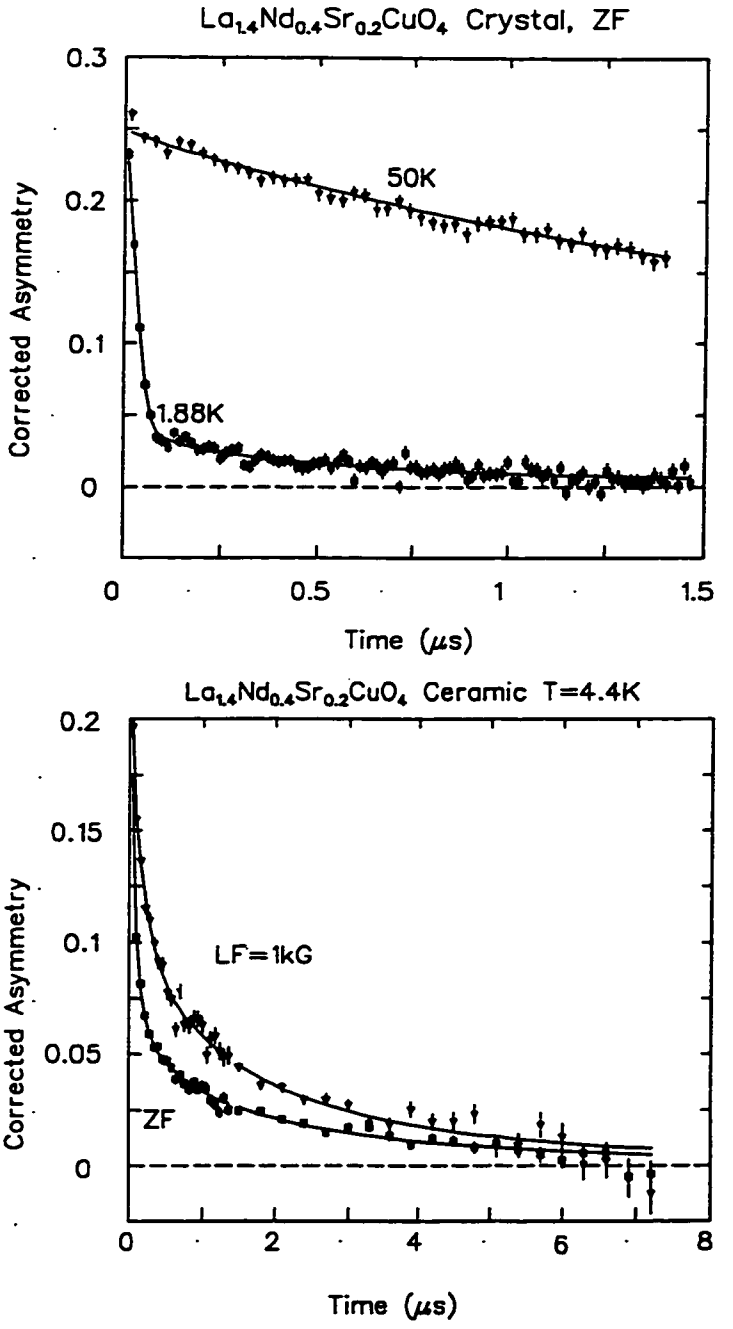

Figure 4.14 ZF spectra of the $La_{1.4}Nd_{0.4}Sr_{0.2}CuO_4$ single crystal at 1.88K, and the decoupling in 1kG for a ceramic sample at 4.4K.

4.3.1 The Muon Site

To definitively extract S_0 from the measured ZF-μSR signal, we need to establish the muon site. Hitti *et al.* [52] have deduced the muon site in undoped La_2CuO_4 by assuming that the muon resides 1.0 Å away from an oxygen site and simulating the μSR frequency as a function of the muon position in the ordered state, with the ordered moment determined by neutron scattering. They concluded that in this material the muon resides near the apical oxygen, at fractional coordinates $(x/a, y/b, z/c) = (0.253, 0, 0.162)$, or at an angular position $(\theta = 1.569, \phi = n\pi/2)$ on the sphere of radius 1.0 Å surrounding the apical oxygen. The barriers between these sites are due mostly to the four La ions located at the intermediate angles.

This site is not the global electrostatic minimum on the spherical surface surrounding the apical oxygen. Figure 4.15 shows the results of a simple Ewald calculation, assuming ionic charges, for this surface. The global minimum for undoped La_2CuO_4 occurs at $\theta = 0.66$, and a similar local minimum occurs at $\theta = 1.88$. The curvature of the potential near the minima $k \sim 0.1\text{eV/Å}^2$. Taking the muon mass at 106 MeV, the harmonic approximation then gives a ground-state dispersion in position of $\Delta x \sim 0.4$Å, so the muon might be localized near the local minimum of $\theta = 1.88$ in the absence of other effects such as self-trapping. A similar Ewald calculation for the doped lattice using the average ionic charges, gives essentially the same result for the potential surface. I estimate the effect of doping in the unit cell by treating the case of Sr substitution at the La sites as an additional negative charge at one of the 5 La sites nearest the apical oxygen. For the most common arrangement with the substitution at one of the fourfold coordinated La sites, this had the effect of eliminating the barrier between two adjacent muon sites at $(2n+1)\pi/4$ on the sphere. However,

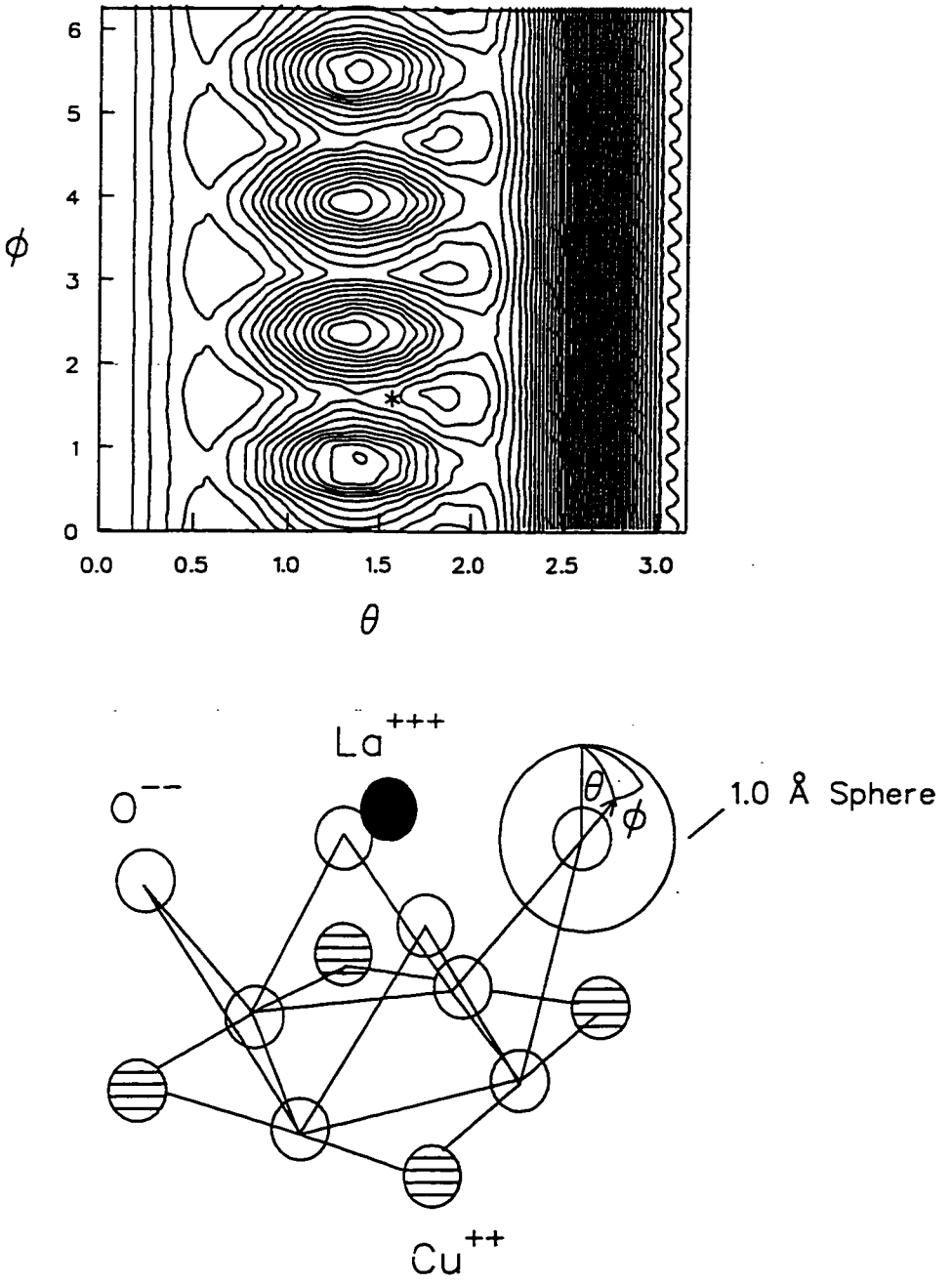

Figure 4.15 The electrostatic potential energy surface as a function of θ and ϕ at a radius of 1Å from the apical oxygen, as calculated with an Ewald sum. The asterisk denotes one of the four equivalent sites found by Hitti *et al.*[52].

allowing the muon to reside between two of these minima does not introduce very different frequencies.

One mechanism which would introduce different frequencies would be to allow the muon site to become correlated with the charge modulation—if the charge modulation is made sufficiently narrow so that the muon could lower its energy by moving toward the high-spin, low-charge Cu^{++} region. However simulations of the muon asymmetry signal such as those described in the next section show that this mechanism would lead to the presence of a relatively high-frequency part of the oscillating asymmetry signal, where only one frequency is observed. It seems likely that the muon site in the doped compounds is nearly the same as that in the undoped La_2CuO_4.

4.3.2 Spin Structure and Simulations

μSR is a real-space probe. As such it is difficult to distinguish, using μSR, among the various possible shapes for the spin modulation. Even in antiferromagnetic La_2CuO_4 well below T_N, there is significant damping of the oscillating μSR signal. However, simulating the μSR signal does confirm that (1)the dominant frequency of the μSR signal is fairly independent of the shape of the modulation, and that (2) the presence of the antiphase stripe order does not significantly alter the simple frequency-ratio calculation of S_0.

The simulations assembled the antiphase modulated spin lattice several times with the phase of the modulation in each plane randomly assigned to one of the values allowed by the commensurate modulation length (for a commensurate modulation) or to any value (for an incommensurate modulation). The magnetic field at the muon site was then calculated assuming a dipolar magnetic coupling between the electron

spins and the muon spin.

The results for three different static modulations with $S_0 = 1\mu_B$ are shown in Fig. 4.17. The characteristics of each may be understood simply as the result of the differing local spin structures near the muon site. For the simple sinusoidal modulation with wavelength of 8 lattice units, three different spin sizes $(1, 1/\sqrt{2}, 0)$ lead to three frequency peaks. For the blocked-sinusoidal modulation of the same wavelength, two spin sizes lead to two peaks; and for an incommensurate modulation there is a continuum of allowed spin sizes and muon precession frequencies. A fourth kind of modulation, related to the incommensurate spectrum, involves disordered pinnings of the stripes which gives a locally incommensurate modulation with a variable wavelength. Intraplanar phase disorder (as distinguished from incommensurability) could result from inhomogeneous pinning of intrinsically commensurate stripes which stretches out the fundamental modulation and thereby introduces a continuum of local spin sizes, as shown in Fig. 4.16. The shape of the spin modulation envelope in the $La_{1.475}Nd_{0.4}Sr_{0.125}CuO_4$ system has been determined by neutron scattering to be primarily sinusoidal. However, Bragg peaks from the higher harmonics would only have been a few percent of the intensity due to the (already small) fundamental reflection. The simulations from each of the modulations discussed above may be made to resemble the observed spectrum for $La_{1.875}Ba_{0.125}CuO_4$ by including appropriate amounts of Gaussian disorder or phase disorder/incommensurability. The simplest scenario consistent with both the μSR and neutron scattering results is a sinusoidal modulation with a high degree of incommensurability or phase disorder.

We might ask, just how much disorder is required to make the commensurate modulation resemble the incommensurate modulation? Let us assume that the local field is proportional to the size of the spin on the Cu nearest the muon site (this

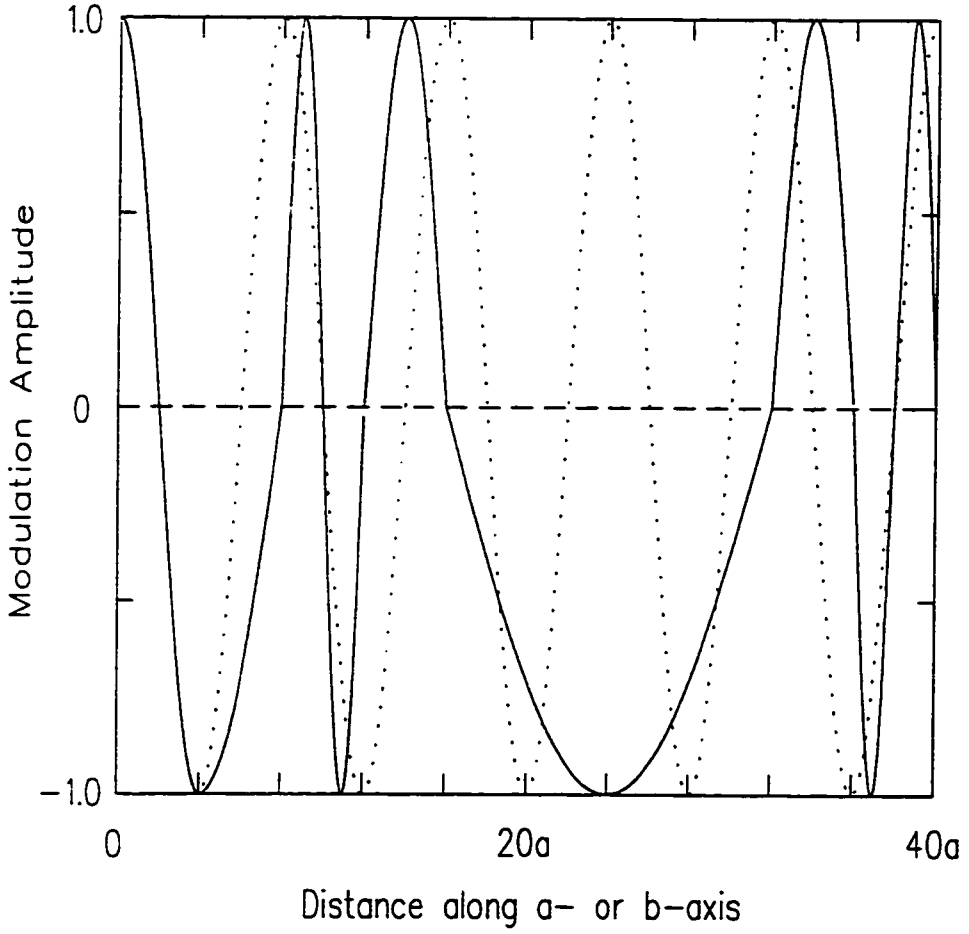

Figure 4.16 The "phase-disordered" modulation profile.

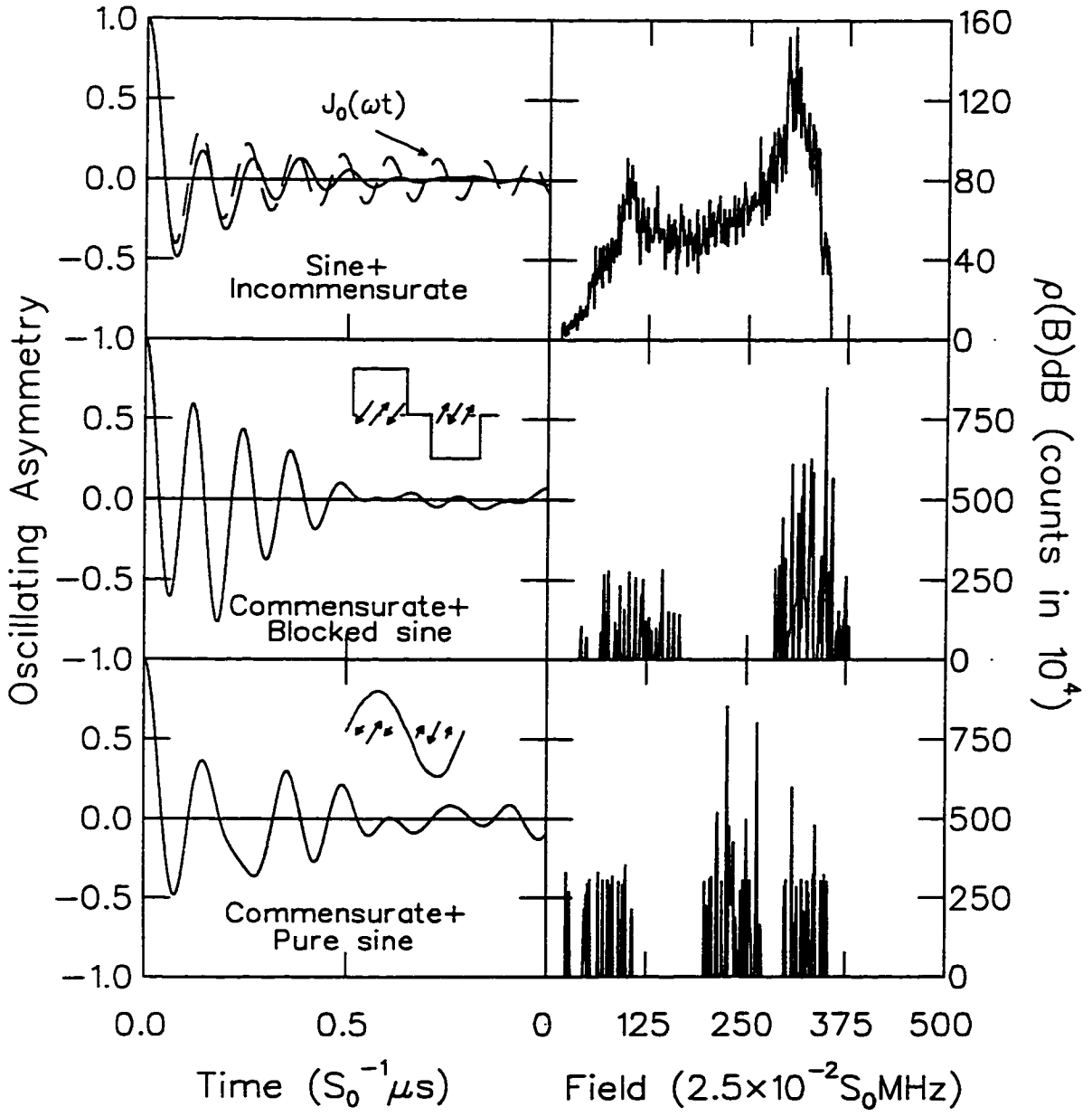

Figure 4.17 Simulated $A_\perp$ component of the muon asymmetry spectrum for various shapes of the spin modulation, along with the corresponding magnetic field distributions at the muon site.

is roughly true for the simulations above). An incommensurate sinusoidal modulation in this case will yield a pure Besel function field distribution, while a commensurate sinusoidal modulation with a period of $8a$ will yield a three-component field distribution. Consider an idealized situation in which the wavelength of the modulation is allowed to take on any discrete value $\lambda = na$, with probability P_n. Then the magnetic field for each wavelength will take on values proportional to $\sin(2\pi j/n), 0 \leq j < n-1$. Model the case of a disordered, commensurate modulation by letting $P_n \propto \exp(-(\mathrm{n} - \bar{\mathrm{n}})^2/2\Delta^2)$, where Δ is the variance of the wavelength and $\bar{n}a$ is the mean wavelength. The shortest possible modulation wavelength is a; to maintain the same average spacing for this symmetrical distribution of wavelengths, the possible wavelengths are then restricted to the interval $[a, 17a]$. The results of this simple model are shown in Fig. 4.18. For $\Delta \sim 1$, the spectrum shows prominent beats; however, as Δ increases, the spectrum rapidly turns into a very Bessel-like shape. In a calculation which includes the effects of the neighboring planes, the beats will be further smoothed. Hence it seems plausible that the modulation of the spin density could be commensurate, but with a slightly variable wavelength.

Despite this ambiguity, the ordering frequency is relatively robust among the commensurate and incommensurate simulations. According to the results of Fig. 4.17, the fundamental frequency observed for each of these spin structures would be approximately the same. Scaling the frequency for the incommensurate modulation simulation to the measured frequency in $La_{1.875}Ba_{0.125}CuO_4$ gives $S_0 \approx 0.34\mu_B$ for this spin structure.

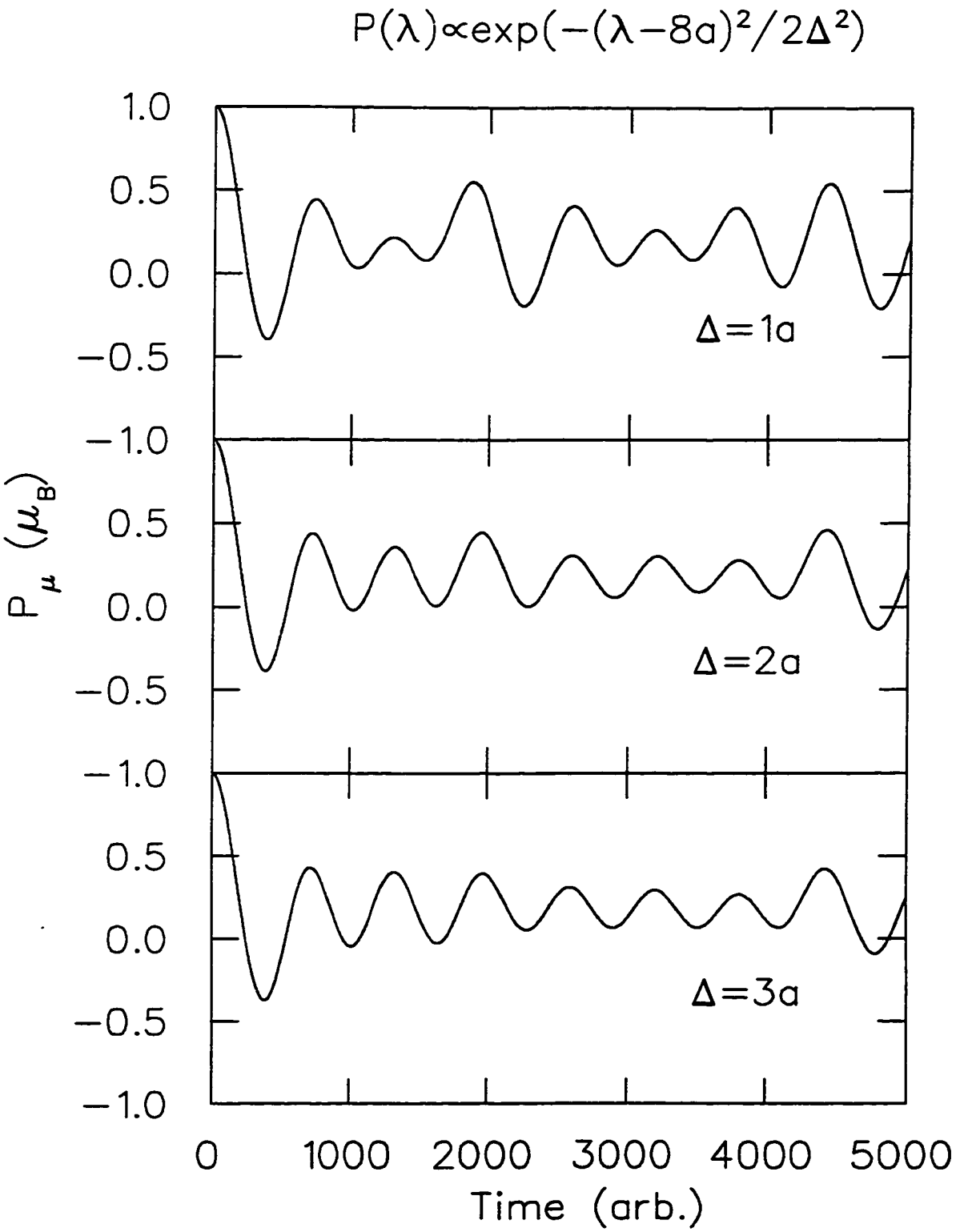

Figure 4.18 Simulated $A_\perp$ component of the muon asymmetry spectrum for commensurate spin modulations with domains of different wavelength, assuming a contact interaction between the muon and its nearest neighboring Cu spin.

4.3.3 Comparison with Neutron Scattering Measurements

The measured values of T_N also differ substantially from those derived from the neutron scattering measurements. Figure 4.19, compares the scaled intensity of the magnetic Bragg peak along with the analogous quantity derived from the μSR data, $A_\perp|\nu|^2$. The μSR and neutron scattering data for the crystal were taken on the same sample. In the neutron scattering experiment, the charge-ordering peaks show finite intensity below $T_{CO} \approx 60$K, and the magnetic peaks show finite intensity below $T_N \approx 50$K. However, as noted above, the μSR measurements show no magnetic order until the temperature drops below 30K. The cause of this disagreement may be the coarser energy resolution of the neutron scattering experiment. The neutron scattering measurements were done with an open collimation to maximize the weak signals from the nuclear superlattice peaks. Indeed, neutron scattering measurements of different crystals of $La_{1.475}Nd_{0.4}Sr_{0.125}CuO_4$ with tighter energy resolutions show that the magnetic Bragg peak of the spin modulation broadens substantially above $T_N(\mu\text{SR})$ [53]. This implies that, between T_N(neutrons) and $T_N(\mu\text{SR})$, the Cu spins are merely quasi-static, with true static order occurring below $T_N(\mu\text{SR})$. These results are also consistent with the evidence that the frozen moment seen in the $x = 0.20$ system is quasistatic. In the $x = 0.125$ system, apparently, the pinning effect is more pronounced.

One can simulate the effect of slow fluctuations of the spin stripe positions on the static commensurate $La_{1.875}Ba_{0.125}CuO_4$ spectrum. The effect of spin fluctuations within a stripe should be similar, since for the locally nearly-AF order the effect of spin-flips or stripe movement beneath the muon are almost equivalent. Similarly, the effect of fluctuations within commensurate and incommensurate spin structures would

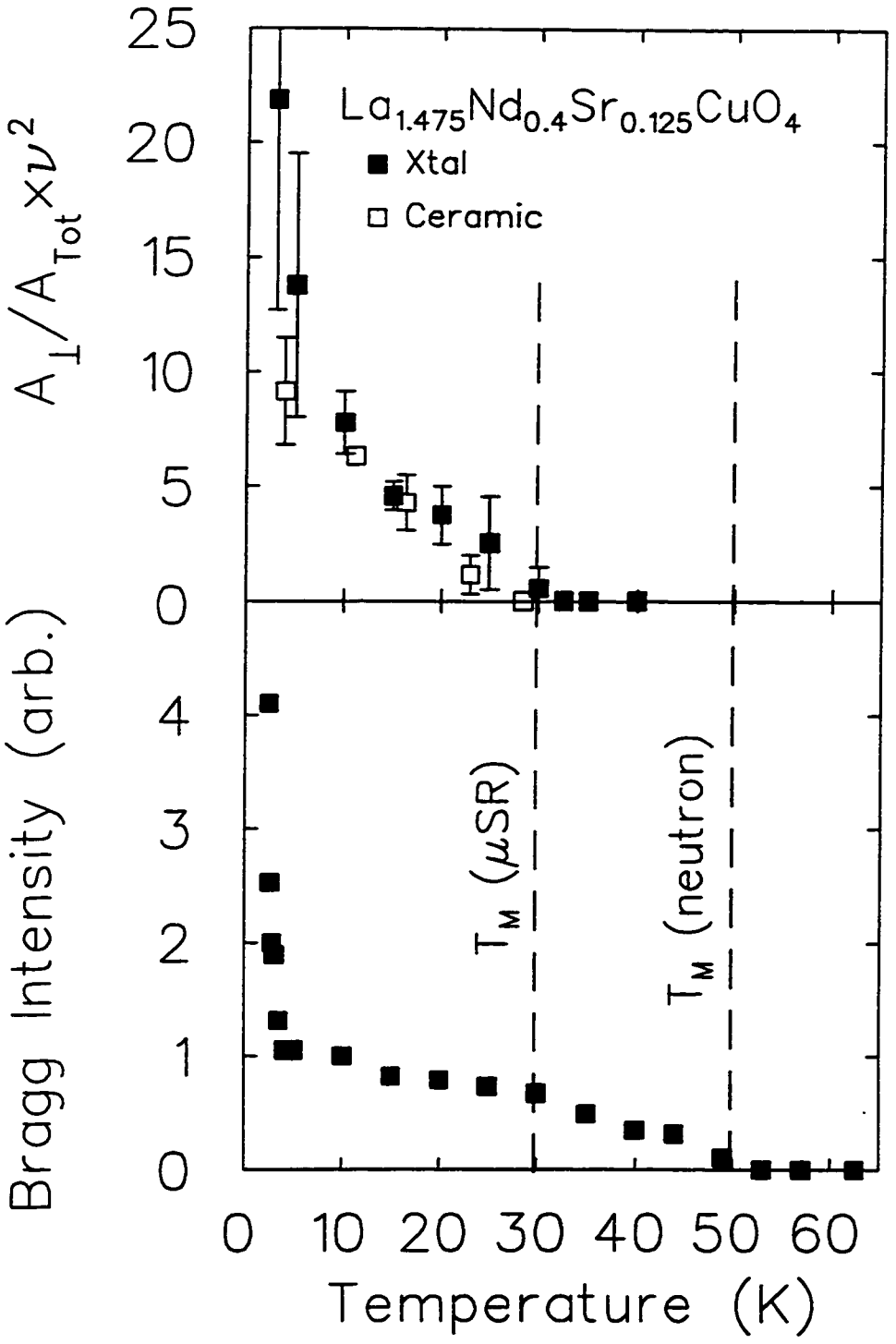

Figure 4.19 Comparison of neutron scattering magnetic Bragg intensity of the satellite peak in $La_{1.475}Nd_{0.4}Sr_{0.125}CuO_4$ to the analogous quantity derived from the μSR measurements.

be almost the same. The commensurate spectrum is used for because the relatively short period eases the computation.

Comparison of the relaxation of the $A_{||}$ aligned component in $La_{1.875}Ba_{0.125}CuO_4$ to the simulated relaxation rate yields a rough estimate the upper limit of such a fluctuation rate. The simulation was dynamicized as follows: for each time step, we calculated the local dipolar field at the muon site. The muon polarization was developed according to the Bloch equations for the expectation values of the spin. Before the next time step, the modulated order was allowed to shift over one lattice unit, with random probablilty. The probability per time step of a shift determined the model spin fluctuation rate.

Figure 4.20 shows the results for the blocked-sine modulation with static gaussian broadening proportional to the local field and S_0=1, with several values of the hopping probability per nanosecond ν_h. Values of ν_h down to about $12.5 \times S_0 \mu s^{-1}$ would induce a relaxation of the $A_{||}$ asymmetry component which is stronger, in relation to the oscillation frequency, than the rate seen in the data for the statically ordered $La_{1.875}Ba_{0.125}CuO_4$ ceramic samples. Hence our data confirm that the spins are static, with an upper limit for the hop rate of $\nu_h = 3.75 \mu s^{-1}$ well below $T_N(\mu SR)$.

S_0 from the neutron scattering measurements[42] $\approx 0.1 \mu_B$, which is a factor of 3 smaller than S_0 derived from μSR. One explanation for this disparity is that, since neutron scattering is a nonlocal probe, disorder in the direction and phase of the magnetic modulation reduce S_0(neutron) as compared to $S_0(\mu SR)$. A similar effect has been inferred from the comparison of μSR and neutron scattering measurements of S_0 for the low-T_N samples of La_2CuO_{4-y}[54]. The in-plane correlation length of the magnetic order seen with neutron scattering is on the order of 170 Å–fairly good

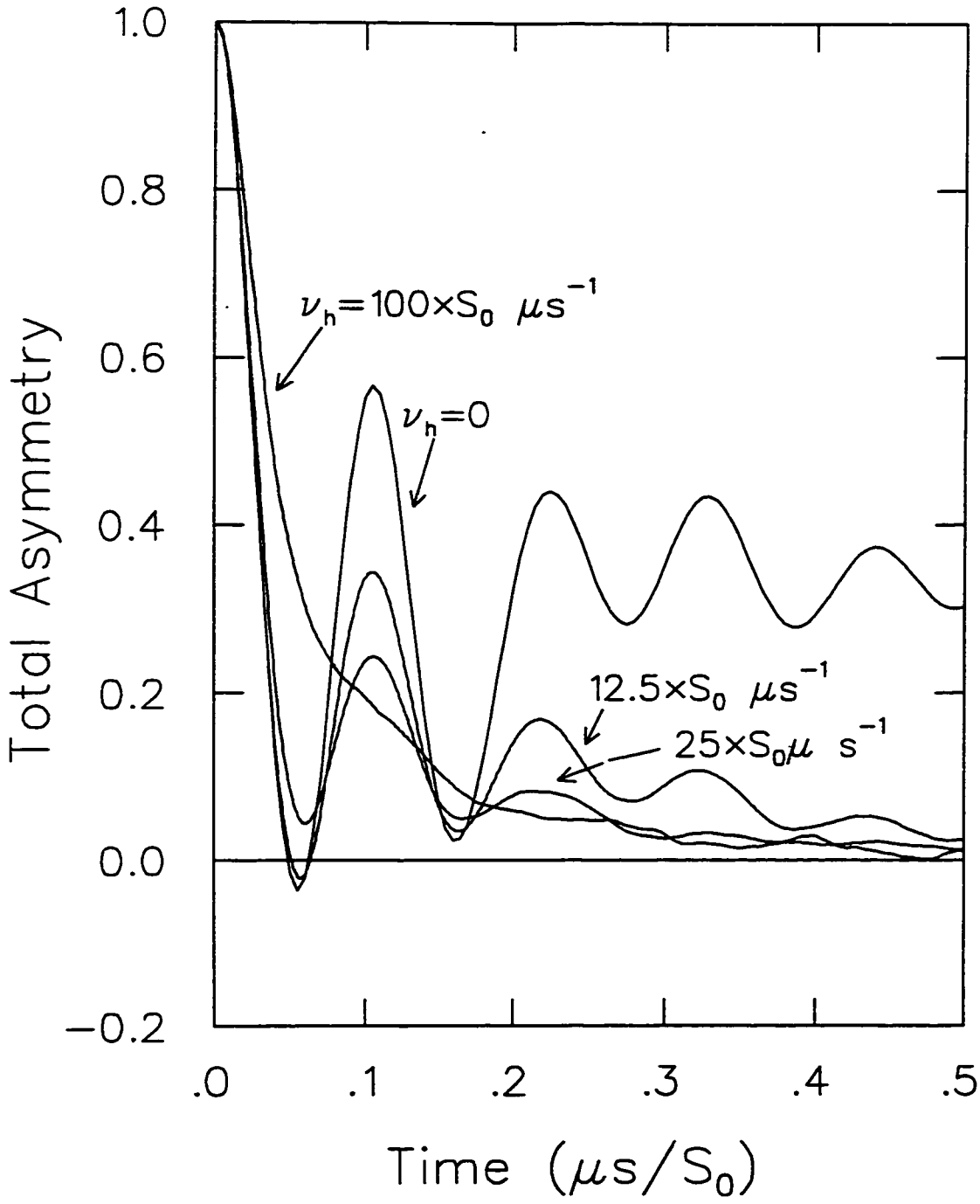

Figure 4.20 The effect of stripe motion of the gaussian-broadened spectrum for the blocked-sine modulation.

long range order. Therefore any order invoked to rectify the two results for S_0 must be short-ranged and self-correcting over several wavelengths of the modulation, as is the phase-disorder mentioned above.

I now briefly discuss the support in the neutron scattering measurements for the incommensurate or phase-disordered lineshape described by a damped Bessel function. The neutron scattering measurements of Tranquada *et al.* on $La_{1.475}Nd_{0.4}Sr_{0.125}CuO_4$ yield an incommensurate magnetic modulation wavevector of $\epsilon \approx 0.118 \times 2\pi/a$. One possible explanation for this very incommensurate value is that about 25% of the charge stripes are slightly displaced[42] from the position they would have in a commensurate modulation. The difference between $S_0(\mu SR)$ and S_0(neutron) implies that disorder plays a strong role in this system. ϵ of the dynamic modulations seen in SC samples increases proportionately to x. As x increases above 0.125, ϵ changes very slowly [42]. This suggests that the stripes tend to be pinned at a single spacing, even as the charge density increases. For SC samples, Yamada*et al.* [55] have suggested that this effect is due to an overloading of the O-2p hole states, and that much beyond $x = 0.125$ the doped holes change to an Cu-3d character. One might expect from these trends the gradual destruction of the static stripe phase by "overcrowding"as doping increases much beyond $x = 0.125$, as is seen for $x = 0.20$.

4.3.4 Comparison to AF La_2CuO_4 Systems

Fig. 4.21 compares the μSR frequencies for the samples in this chapter to the frequencies in the $x < 0.02$ "doped AF" samples measured by Borsa *et al.*[38]. The doped AF samples show evidence of two transitions. At intermediate temperatures, the precession frequency in $La_{1.984}Sr_{0.016}CuO_4$ is comparable to that seen in the $x = 0.125$ samples. However at T <50K, there is an enhancement of the frequency

in $La_{1.984}Sr_{0.016}CuO_4$ and $La_{1.986}Sr_{0.014}CuO_4$ which brings the ordered moments up to almost the full value for La_2CuO_4. Borsa *et al.* have explained the reduced magnetization in the intermediate temperature range as the result of finite size effects on the antiferromagnon spectrum due to the segregation of the doped holes in the CuO_2 plane. Hone and Castro-Neto[56, 57] have proposed an explanation of the reduction of T_N at light dopings in a similar physical picture by estimating the effect of an anisotropy in the magnetic coupling in the directions along and across the stripes. I plot the extrapolated zero-temperature magnetizations $M(x = 0.125)/M(x = 0)$, and $T_N(x = 0.125)/T_N(0)$ along with the results of Borsa *et al.* and the finite-size theory in the lower panel Fig. 4.21. An important difference between the lightly doped AF and the situation in the $x \geq 0.125$ systems is that the antiphase magnetic order in the latter allows for stronger correlations through the regions where the spin is suppressed. Hence while real-space renormalization calculations for the lightly-doped AF show a crossover from 2-dimensional domains of correlated spins to 1-dimensional domains, and a concomitant loss of AF order at $x \sim 0.025$, the antiphase magnetic order is more robust and should be less reduced in dimension with doping.

4.3.5 Dimensionality of the Magnetic Order: Comparisons to Other AF Cuprates

Various μSR experiments highlight the importance of magnetic exchange anisotropy in determining S_0 for the various cuprate antiferromagnetic systems. Several quasi 1-dimensional, chain-like systems (Sr_2CuO_3, Ca_2CuO_3, $KCuF_3$, and $Ca_{0.966}Zn_{0.034}GeO_3$) have been studied by Kojima *et al.*[58], who showed that, if one scales T_N by the stronger antiferromagnetic exchange along the chain direction (denoted J_{AF}) then S_0 decreases with T_N/J_{AF}. The behavior of all of the one-dimensional systems measured

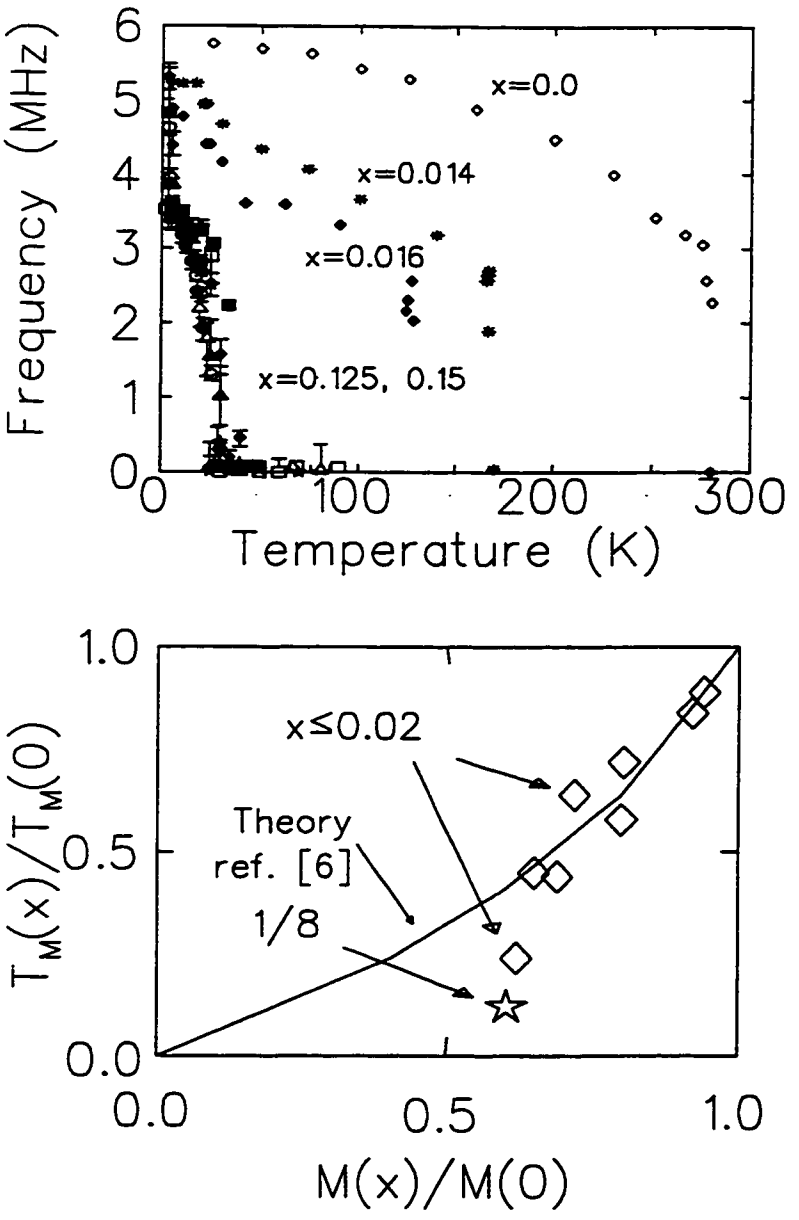

Figure 4.21 Upper panel: the μSR precession frequency for lightly doped AF $La_{2-x}Sr_xCuO_4$ with $x < 0.02$. The data from the present study for $x \geq 0.125$ is also shown. Lower Panel: a plot of the reduced $T_N(x)$ and $M(T = 0, x)$ for lightly doped AF $La_{2-x}Sr_xCuO_4$ along with the prediction of Hone and Castro-Neto (from reference [56, 57]), and the data from the more highly doped samples in the present study.

with μSR is very well described by the "chain mean-field" (CMF) theory of Affleck *et al.*[59]. The CMF theory treats each chain exactly in the mean field due to the other chains.

The data for the quasi-1d systems as well as the prediction of the chain mean-field theory are reproduced in Fig. 4.22. To this figure we add points for the quasi-2d cuprate antiferromagnets composed of stacked CuO_2 planes: $Sr_2CuO_2Cl_2$, $Ca_{0.86}Sr_{0.14}CuO_2$, $YBa_2Cu_3O_{6.15}$, and La_2CuO_{4-y} systems[54, 60, 61, 62]. These quasi-2d systems all have $S_0 \approx 0.5\mu_B$, independent of T_N.

Where do the stripe systems fit into this picture? Let us assume that the coupling within the stripes does not change very much from the case of La_2CuO_4. Then, a nominal value of $J_{AF} \approx 1300$K, places the striped systems intermediately between the quasi-1d and quasi-2d limits. For another comparison, I also plot a point for the "3-leg ladder" material $Sr_4Cu_6O_{10}$. As Fig. 4.23 shows, the structures of the stripe and ladder materials are similar in that both consist of nominally antiferromagnetic strips, about thre lattice constants across. For the ladder material, however, the interladder coupling is strongly frustrated. In the plot of Fig. 4.23, the ladder material falls in the quasi-1d regime. Like the theoretical calculations mentioned in the previous section, these comparisons suggest that the couplings across the boundaries for the stripe materials are comparatively stronger than for the quasi-1d cuprates, though not strong enough to bring them fully into the quasi-2d regime.

4.4 Summary

This chapter presented the ZF-μSR measurements of several "214" cuprate systems where superconductivity has been suppressed in concert with the LTO→LTT transi-

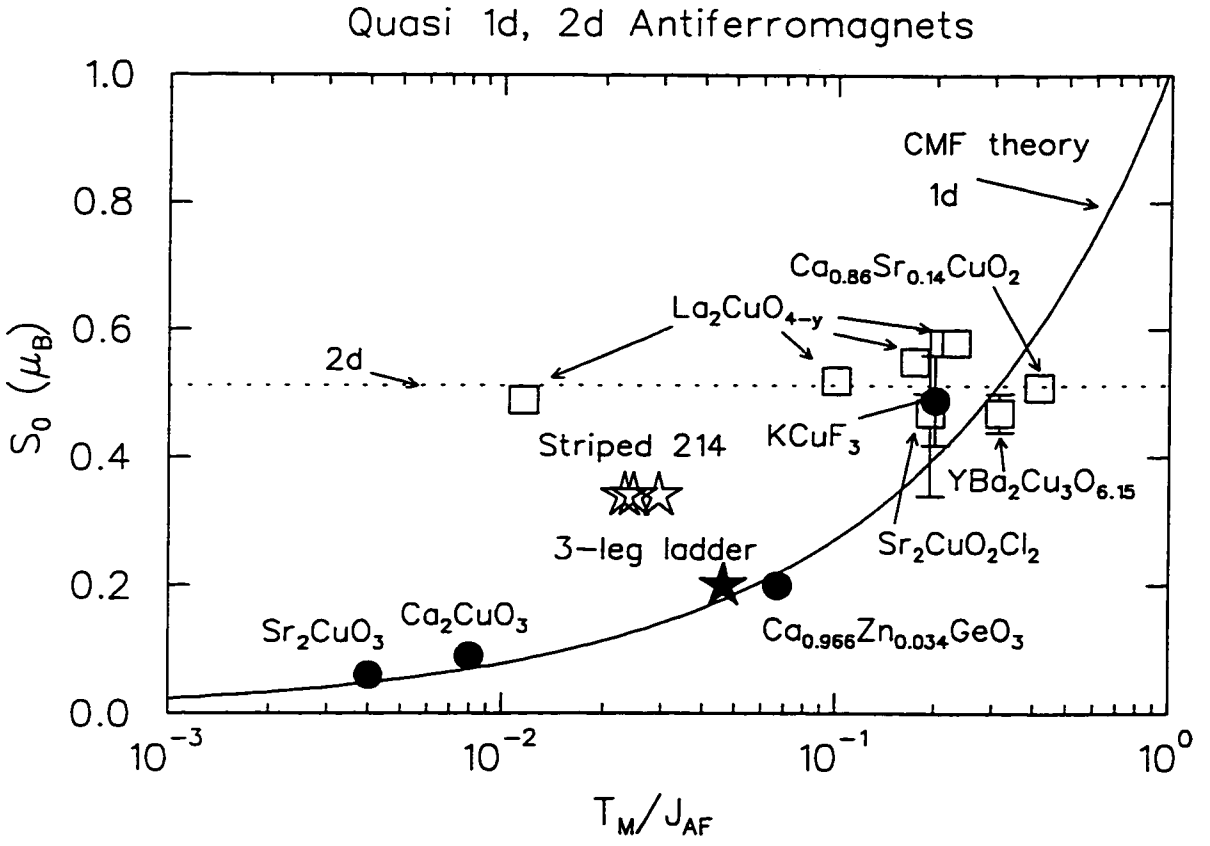

Figure 4.22 A comparison of quasi one-dimensional (closed circles)[58],quasi two-dimensional (open squares) [54, 60, 61, 62], and stripe (stars) AF systems. The solid curve is the relationship between S_0 and T_N/J_{AF} derived in reference [59]. The dotted line roughly defines the observed S_0 in all quasi two-dimensional systems.

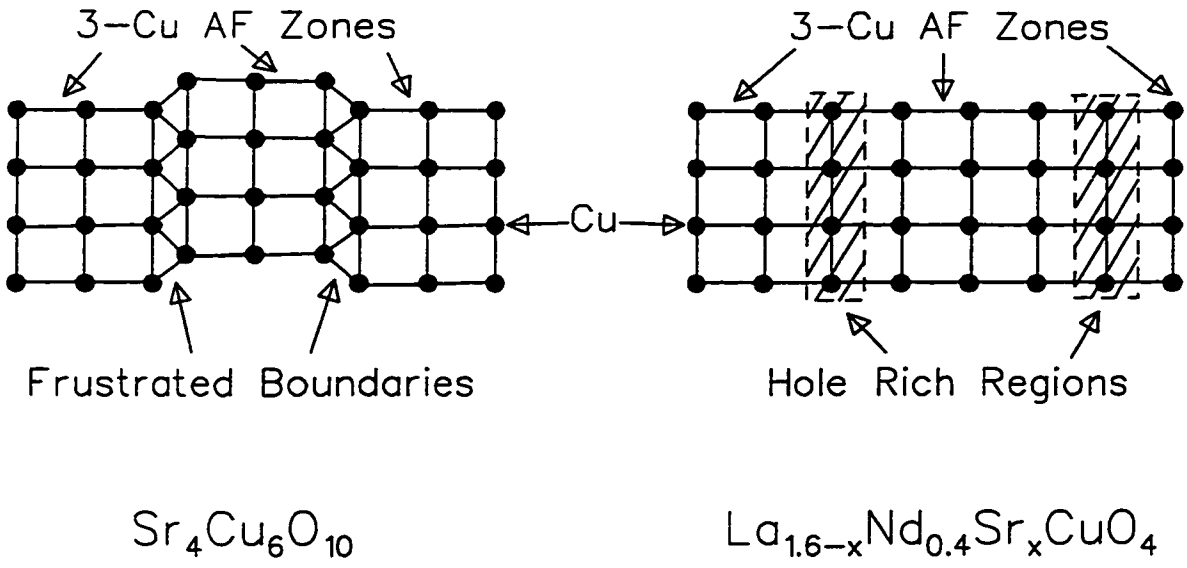

Figure 4.23 A comparison of (left) the 3-leg ladder cuprate $Sr_4Cu_6O_{10}$ and (right) the CuO_2 plane with hole stripes.

tion and the "1/8" effect, and yields the following conclusions:

(1) The data from all samples are best described by a modulation which yields a single frequency within the uncertainties of the asymmetry spectrum. On the 100-ns timescale, the order is describable as an incommensurate static modulation of antiferromagnetic order, or a commensurate modulation with large local inhomogeneous pinning effects. In the $La_{1.875}Bs_{0.125}CuO_4$ system, at the least, the magnetism is static to within a small fraction of the spontaneous precession frequency.

(2) There is strong evidence, from the successful neutron scattering analysis of the Nd low-temperature interplanar correlations, and the LF μSR data persented here, that in $La_{1.6-x}Nd_{0.4}Sr_xCuO_4$, for $x = 0.125$ and $x = 0.15$, the Nd and Cu spin systems remain distinct down to $T \approx 5$K. The size of the ordered Cu moment, S_0, at 10K is constant within the uncertainties for all of the samples showing spontaneous

precession, with a value estimated at $0.34\mu_B$.

(3) Simple comparisons of S_0 and the T_N/J_{AF} ratio to those for quasi-1d and quasi-2d spin-1/2 cuprate antiferromagnets suggest that the magnetic order in the stripe systems can be described as intermediate between the 1-dimensional and the 2-dimensional limits. These values of S_0 and T_N differ significantly from those previously reported from neutron scattering measurements.

Chapter 5

Superconductivity in the Striped Phase

DC susceptibility measurements [63, 42] suggest that superconductivity and stripe magnetic order coexist in the stripe materials, which raises the interesting possibility of the existence of a superconducting network of low-dimensional wires (the charge-rich stripes, with interplanar coupling allowed). However, since DC susceptibility is a bulk measurement, such results may also indicate a phase separation between superconducting and magnetically ordered volumes of the same sample.

Emery, Kivelson, and Zachar[48], and Castro-Neto and Hone[57], have developed theories of superconductivity involving coherent arrays or networks of charge stripes in an antiferromagnetic background. However, there has been no confirmation of the relative magnetic and superconducting volume fractions in a single sample. In this chapter, the techniques of transverse-field (TF) μSR are used to show that single crystals of $La_{1.45}Nd_{0.4}Sr_{0.15}CuO_4$ and $La_{1.4}Nd_{0.4}Sr_{0.2}CuO_4$ show similarly large hysteresis effects attributable to flux pinning in the superconducting state. The $La_{1.45}Nd_{0.4}Sr_{0.15}CuO_4$ crystal was then pulverized. ZF-μSR measurements on this powdered sample show that the *entire sample* becomes magnetic. This suggests that the superconducting and magnetic phases microscopically coexist in the stripe phase.

5.1 TF μSR Hysteresis Measurements

Below the flux-pinning temperature T_p in a superconductor, the FC and ZFC relaxation rates should diverge with the ZFC rate becoming larger due to inhomogeneous pinning in the flux lattice. The $La_{1.45}Nd_{0.4}Sr_{0.15}CuO4$ and $La_{1.4}Nd_{0.4}Sr_{0.2}CuO_4$ crystals were mounted on silver backing, behind a silver mask in a cold-finger cryostat. The asymmetries from the sample and the mask were counted separately, in a specialized Knight-shift apparatus designed by the μSR group at UBC. The degree of relaxation from the silver mask signal provided a rough check of the strength of the fringing fields in the sample.

The relaxation envelope of the sample signal was fit to the form $G(t) = \exp-(\Lambda t)^{\beta}$. In addition, there was a small background signal estimated from a small long-lived component of the oscillating asymmetry, most likely due to muons from the silver backing. For both samples, the background signal accounted for less than 10% of the total asymmetry. Figure 5.1 compares sample spectra in FC and ZFC showing pronounced differences in relaxation rate.

The comparative relaxation rates of the sample asymmetry are shown as a function of temperature in Fig. 5.2. Note the relatively large relaxation rate in $La_{1.45}Nd_{0.4}Sr_{0.15}CuO_4$ for $T_p < T < 20$K: this enhancement suggests that in this temperature regime, the static magnetic field is broadened due to the magnetic order in this system. Below T_p, the relaxation rate is enhanced for the entire asymmetry in each sample.

These TF-μSR measurements by themselves do not rule out the possibility of inhomogeneous superconductivity on the scale of the London penetration depth. The effect of the fringe fields in the vortex state in ZFC is so large that the case of a

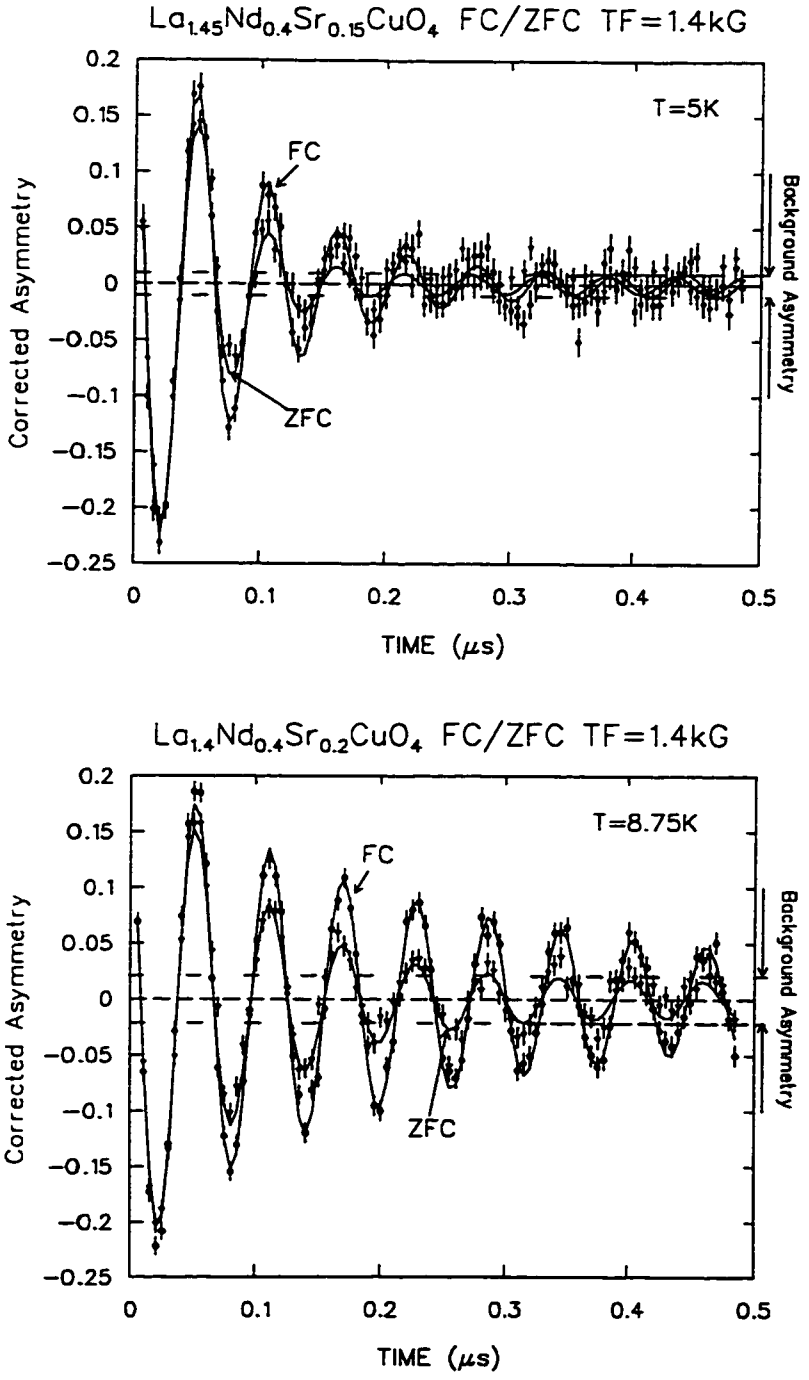

Figure 5.1 Comparison of FC and ZFC asymmetry spectra below T_p for an applied TF of 1400G.

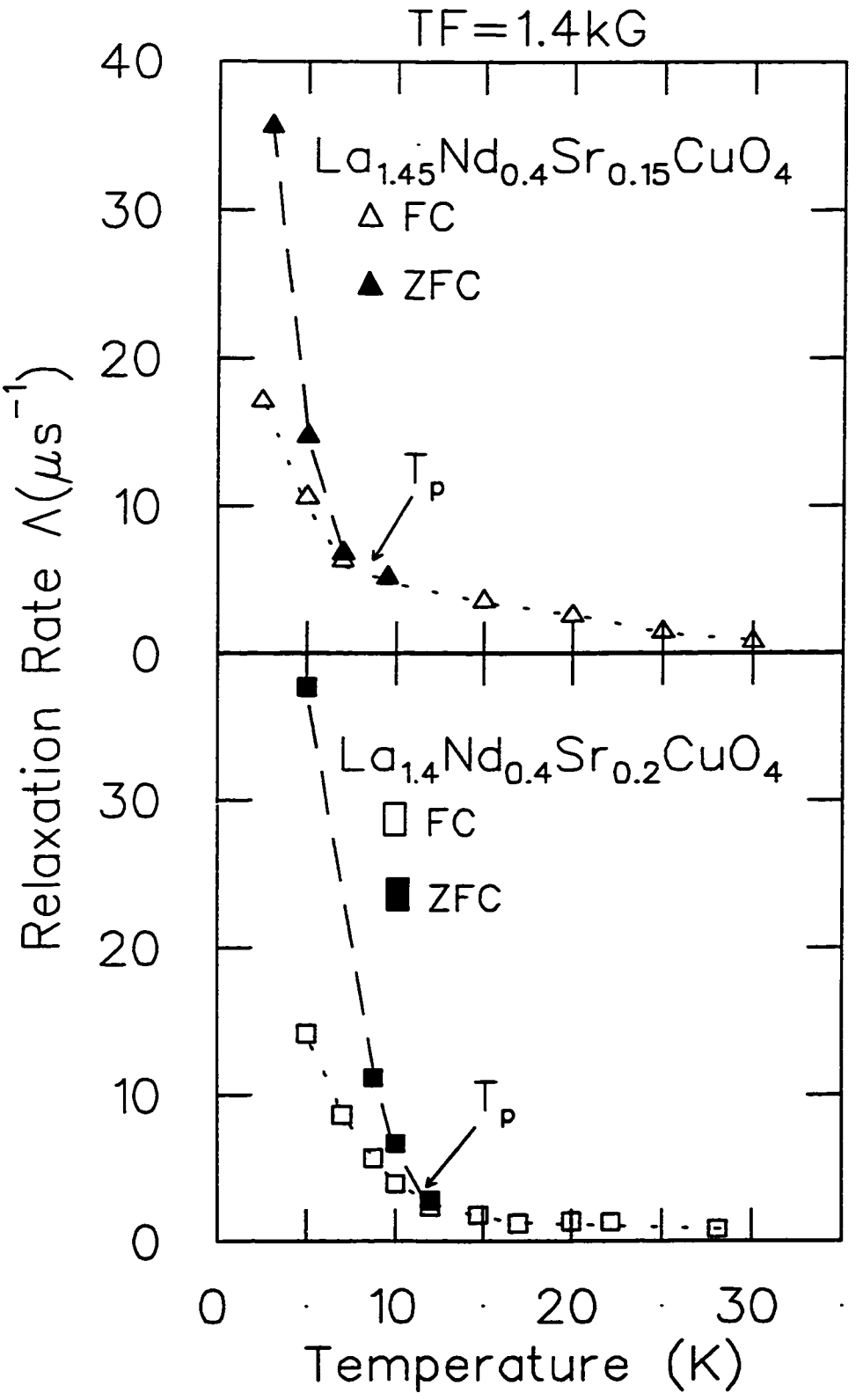

Figure 5.2 The FC and ZFC TF-μSR relaxation rates in $La_{1.45}Nd_{0.4}Sr_{0.15}CuO_4$ and $La_{1.4}Nd_{0.4}Sr_{0.2}CuO_4$ crystals, in an applied field of 1400G.

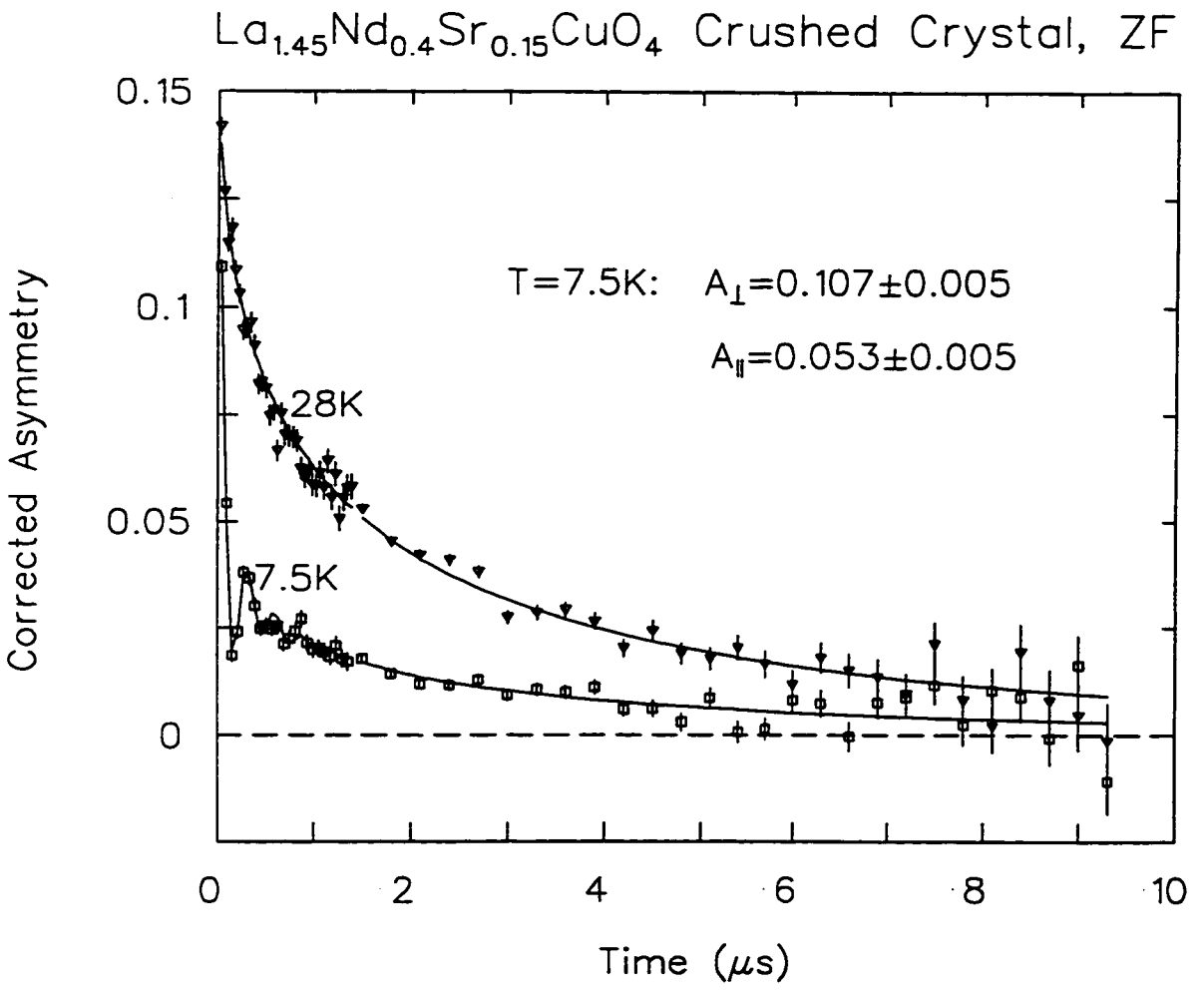

Figure 5.3 ZF spectra of the pulverized single-crystal sample of $La_{1.45}Nd_{0.4}Sr_{0.15}CuO_4$.

disordered flux expulsion into nonsuperconducting patches of the sample could be largely indistinguishable from the case of uniform superconductivity with a disordered flux lattice. Indeed, in ZFC, the asymmetry from the silver mask was strongly relaxed, while in FC this relaxation was negligible. However, the large hysteresis effect suggests that in these materials, superconductivity and magnetism coexist in the same regions of the sample. We checked this explicitly for the $La_{1.45}Nd_{0.4}Sr_{0.15}CuO_4$ by pulverizing the same crystal used in the hysteresis measurements and measuring its ZF-μSR spectrum. In this manner we precisely measure the magnetically ordered volume fraction, and identify any necessary overlap between the superconducting and magnetically ordered volumes of the sample.

The ZF-μSR spectra in Fig. 5.3 show that magnetic order with $A_\perp/A_\parallel = 2.02 \pm 0.21$ occurred *in the same sample.* Because of the Nd moments throughout the sample, there will be no regions of the sample where the μSR asymmetry does not relax. Hence the presence of a volume fraction which is invisible in ZF is highly unlikely. We may therefore estimate the upper limit of any unordered volume fraction from the lower limit of the observed $A_\perp : A_\parallel$ ratio. Calling the unordered part of the total asymmetry δ,

$$\frac{\frac{2}{3}(A_{tot} - \delta)}{\frac{1}{3}(A_{tot} - \delta) + \delta} = \frac{A_\perp}{A_\parallel}.$$

Then

$$\frac{\delta}{A_{tot}} = \frac{2 - A_\perp/A_\parallel}{2 + A_\perp/A_\parallel}.$$

Substituting our measured values gives $\delta/A_{tot} \approx 0.035$, which means that virtually the entire sample, with a lower limit of $\approx 97\%$ of the volume, was in the magnetically

ordered state. This suggests that, at least on the lengthscale of a penetration depth, the superconducting and magnetic order parameters coexist in the same region of the sample.

Chapter 6

Some Speculations on the Nature of the Stripe Phase

A general conclusion about the stripe materials is that the static modulated magnetic order competes with the superconductivity. In the hybrid materials $La_{1.875}Ba_{0.125-y}Sr_yCuO_4$, there seem to be two distinct volume fractions, one which undergoes the magnetic transition. Lappas *et al.* identify the nonmagnetic transition with the superconducting volume of the sample. This conclusion seems to disagree with the conclusion of the previous section; however, it is possible that a small superconducting portion (less than 10%) of the sample could induce a large hysteresis effect. In this case the modulated magnetic order is anathema to superconductivity, and may indeed represent a Fermi surface effect. Such a nesting effect could lead to a gap in the density of states at the Fermi surface, which would tend to suppress a superconducting transition.

On the other hand, there is some reason to believe that the stripe modulation is intrinsic to the superconductivity. As stated in the introduction to Chapter 4, dynamical modulations of the spin density occur in the superconducting state of the underdoped $La_{2-x}Sr_xCuO_4$ compound. Recently, Yamada *et al.*[55] have investigated the relationship between the modulation wavevector ϵ and T_C over the entire doping range. The pertinent figure from this work is reproduced in Fig. 6.1. For the un-

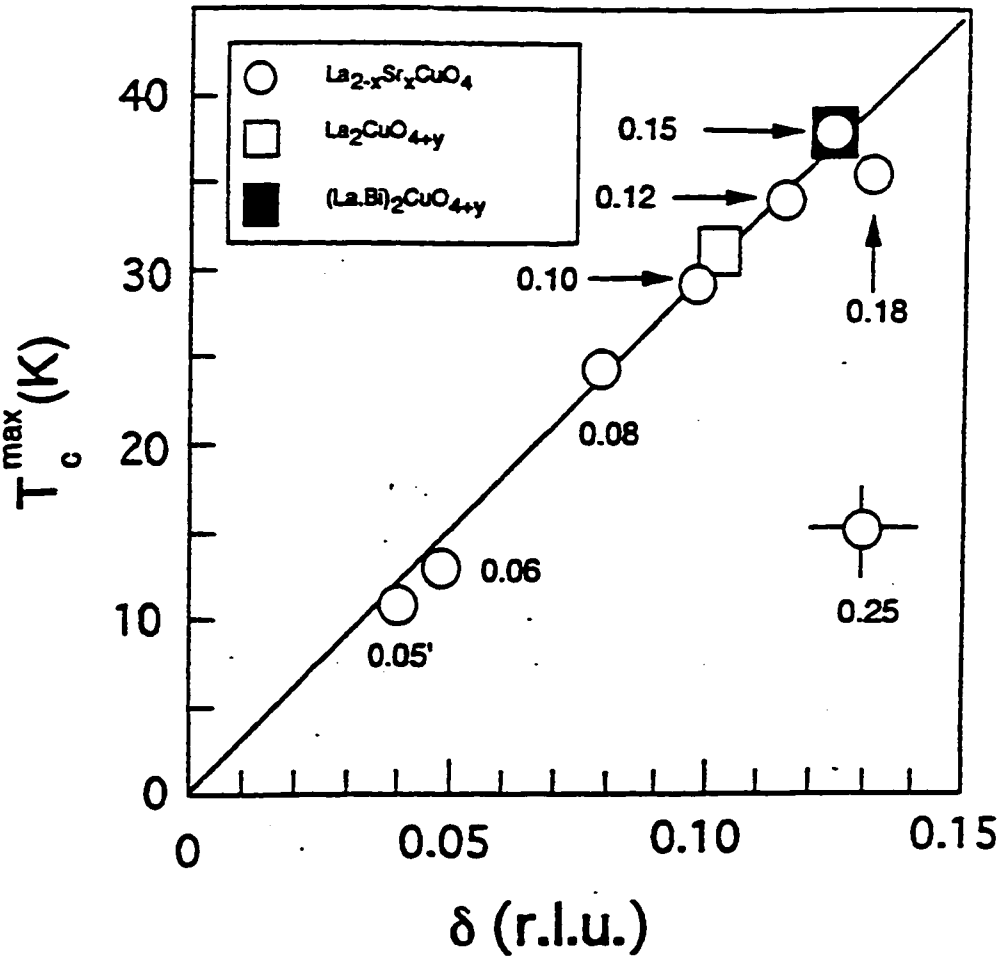

Figure 6.1 T_C as a function of the dynamical modulation wavevector δ (Yamada's δ is the same as our ϵ) for $La_{2-x}Sr_xCuO_4$. From ref. [55].

derdoped compounds, they find a remarkable proportionality, $T_C \propto \epsilon$. The stripes become less coherent in highly overdoped $x \simeq 0.25$ samples. Recent inelastic neutron scattering measurements have shown some evidence of a spin modulation in $YBa_2Cu_3O_{6+x}$. and angle-resolved photoemission experiments on a Bi-based cuprate have shown a transfer of the single-fermion spectral weight which is consistent with scattering from charge modulations.

If the dynamical stripes are important to the superconductivity (rather than a competing instability), then how should pinning effects change the superconductivity? If the stripe fluctuations are necessary to the pairing interaction, then one speculation is that pinning the stripes will "soften" the pairing boson, and thereby lower T_C. From the neutron scattering studies, the modulation seems to be driven by the charge ordering, so one is tempted to look at a softening of the charge fluctuations, or an increase in the effective mass of the doped holes. By combining Yamada's observation $T_C \propto \epsilon$, and Uemura's observation $T_C \propto n_s/m^*$ for a "healthy" underdoped $La_{2-x}SrxCuO_4$ cuprate, one deduces $m^* \propto \kappa/c$, where κ is the inverse spacing between holes in the direction perpendicular to the modulation, and c is the spacing between adjacent CuO_2 planes (a similar combination of these observations has been made by Castro-Neto[64]). When the T_C is suppressed in the "1/8" effect, Yamada's observation for the healthy material may not apply. If one supposes that the relation $T_C \propto n_s/m^*$ still holds, then this may indicate a large increase in m^*. Such an increase in the effective mass is compatible with a softening of the charge fluctuation rate. Since m^* seems to depend on the inverse spacing κ for a healthy superconductor, the putative softening may involve fluctuations in the direction along a stripe, *i. e.* perpendicular to the modulation direction. A possible charge-ordered ground state corresponding to this scenario is sketched in Fig. 6.2.

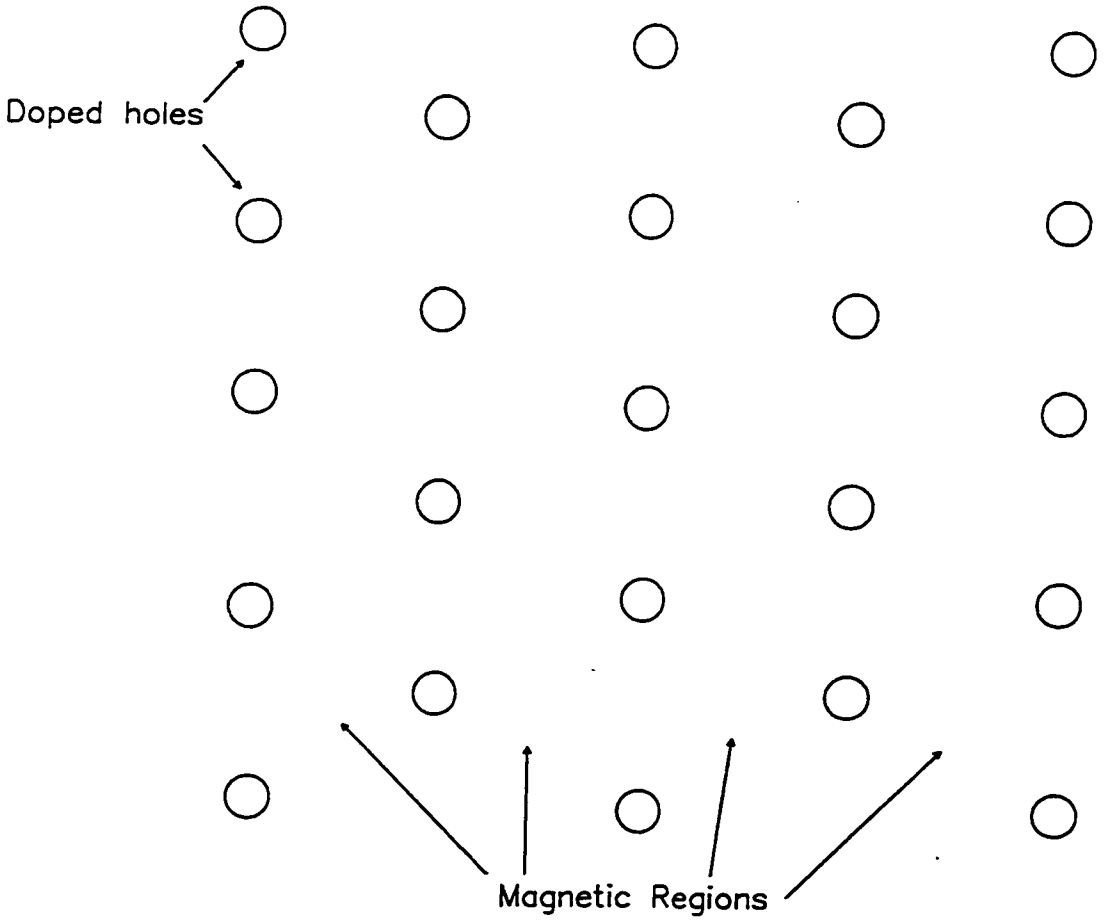

Figure 6.2 A sketch of a possible electronic ground state involving a softening of the charge fluctuations within a stripe.

Chapter 7

Spots: Zn Substitution Effects in the CuO_2 Plane

7.1 Introduction: Characterization of Zn Impurities

Zn substitution in the CuO_2 plane of the cuprate HTSC's has a remarkably strong effect on the superconducting state. In both $La_{2-x}Sr_x(Cu_{1-y}Zn_y)O_4$ and $YBa_2(Cu_{1-y}Zn_y)_3O_{6+x}$, Zn concentrations of only a few percent per planar Cu site are sufficient to completely destroy the superconducting state. The effects are even more remarkable for the fact that Zn is a nominally nonmagnetic impurity, with a filled $3d^{10}$ shell when it is doubly ionized. According to Anderson's theorem[6], a nonmagnetic impurity would have a very small effect on the T_C of an s-wave superconductor. Hence the strong suppression of T_C indicates that one of the two conditions must not hold, to wit: either Zn becomes magnetic when substituted into the CuO_2 plane, or the SC state in the cuprates does not have s-wave symmetry.

Susceptibility [65] and Y-NMR (in $YBa_2(Cu_{1-x}Zn_x)_3O_{6+x}$)[66, 67] show that the Zn substitutions *do* induce magnetic moments in the CuO_2 planes. Comparison in the $YBa_2(Cu_{1-x}Zn_x)_3O_{6+x}$ system to the moment induced by a known chain-substitution of Co confirms that in this system, the Zn goes overwhelmingly to the plane sites.

The size of the induced moment $\sim 0.8\mu_B$ in the underdoped samples, and decreases with increasing hole concentration. The intensities of satellite peaks in the Y-NMR spectrum for underdoped $YBa_2(Cu_{1-x}Zn_x)_3O_{6.6}$ [67] indicates that the induced moments are localized near the Zn impurities. These considerations suggest that Zn could act as a magnetic scatterer.

On the other hand, resistivity measurements[68] suggest that Zn acts as a untitarity-limit potential scatterer in underdoped $YBa_2(Cu_{1-x}Zn_x)_3O_{6+x}$ and $La_{2-x}Sr_x(Cu_{1-y}Zn_y)O_4$. Hence the transport measurements imply that the second condition of Anderson's theorem is broken, at least in the underdoped systems. The same interpretation extends to the transport in overdoped $YBa_2(Cu_{1-x}Zn_x)_3O_{6+x}$ and $La_{2-x}Sr_x(Cu_{1-y}Zn_y)O_4$, if the carrier concentration is determined by $1-x$ instead of x. This observation implies that the character of the conducting fermions may change from underdoping to overdoping, *i. e.* the sample changes from a bad metal with a small Fermi surface to a better metal with a large Fermi surface.

There is independent evidence that the order parameter in $YBa_2(Cu_{1-x}Zn_x)_3O_{6+x}$ has a d-wave shape, leading to nodes in the energy gap along certain directions at the Fermi surface. High-resolution microwave[69] and μSR [18] measurements of the low-temperature dependence of the penetration depth λ_L in single crystal $YBa_2Cu_3O_{6+x}$ is linear, consistent with the existence of line nodes in the gap function. Upon Zn substitution, the low-temperature λ_L depends quadratically on the temperature [17]. In a scattering-pair-breaking model, this crossover corresponds to the change in the angular dependence of the SC gap. Heuristically speaking, the scattering may be thought to average out the sharp nodal structure of the pure $YBa_2(Cu_{1-x}Zn_x)_3O_{6+x}$, leading to a more s-wave-like gap function (albeit with a smaller amplitude reflecting the decrease in T_C).

7.2 Some Experimental Details

From 1994-1997. the Columbia group measured the TF-μSR Gaussian relaxation rate σ in ceramic samples of $La_{2-x}Sr_xCu_{1-y}Zn_yO_4$ with $x = 0.15, 0.20; y = 0, 0.0025, 0.005, 0.01$ and of $YBa_2(Cu_{1-y}Zn_y)_3O_{6.63}$ with $y = 0, 0.05, 0.1$. The TF-μSR experiments were performed on ceramic samples of $La_{2-x}Sr_xCu_{1-y}Zn_yO_4$ The samples were mounted in standard Janis gas-flow cryostats with a base temperature of 2.2 K, and fixed on pressed rust powder to minimize backgrounds: the portion of the muon beam hitting the backing was rapidly depolarized by the Fe moments in the rust. As stated in Chapter 2, for clean-limit samples ($\xi_{ab} < l$) in an applied field H such that $H_{C1} < H \ll H_{C2}$, a fair approximation for ceramic samples is $\sigma \propto n_s/m^*$, the ratio of the superconducting carrier density to the electron effective mass. The cuprates are highly anisotropic, with $m_c^* > m_{ab}^*$, or equivalently, $\lambda_L(H \parallel c) < \lambda_L(H \perp c)$. For a ceramic sample, the angular-averaged relaxation rate which is actually measured is dominated by the shorter λ_L corresponding to screening currents flowing in the CuO_2 planes.

To estimate ξ_{ab}/l in our specimens, we assumed the density of states for a two-dimensional Fermi gas, and used the Sommerfeld parameter γ derived from specific heat measurements [70, 71, 72] and the scattering time τ inferred from resistivity measurements [68], to obtain $l = 52, 59$, and 101 Åfor the $La_{1.85}Sr_{0.15}Cu_{0.99}Zn_{0.01}O_4$ and $YBa_2(Cu_{0.99}Zn_{0.01})_3O_{6.63}$ samples, respectively. The mean free path increases with increasing hole doping and decreasing Zn content. Ando *et al*[73] found that in $La_{1.85}Sr_{0.15}CuO_4$, $H_{C2} = 61$ T at $T/T_C = 0.04$. Extrapolating this result to $T = 0$ gives $H_{C2} = 63.5$ T, or $\xi_{ab} = 22.7$Å. Assuming that $H_{C2} \propto T_C$ as it is in the BCS theory, $\xi_{ab} = 24.52$Åfor $x = 0.20$ $La_{2-x}Sr_xCu_{1-y}Zn_yO_4$, and $\xi_{ab} = 18.3$Å

for $YBa_2Cu_3O_{6.63}$. Hence all of the samples measured here fall near the clean limit for this value of the coherence length. On the other hand, the measurements of Sonier *et al.*[18] suggest that at fileds on the order of a few kilogauss, the radius at which the superfluid velocity around a fluxoid reaches its maximum is on the order of 120Å in $YBa_2Cu_3O_{6+x}$, which would make the scattering corrections much more important. The issue of the proper coherence length is therefore unsettled; I consider both possibilities below.

7.3 General Features of the Data

The sample spectra were fit with a damped Gaussian lineshape,

$$A(t) = A(0)e^{-(\sigma^2/2t^2)} \times \cos(\omega t + \phi).$$

Figure 7.1 shows the behavior of $\sigma(T)$ for the $La_{1.85}Sr_{0.15}Cu_{1-y}Zn_yO_4$ and the $YBa_2(Cu_{1-y}Zn_y)_3O_{6.63}$ series. Zn substitution markedly reduces the low-temperature value $\sigma(T \rightarrow 0)$. Similar results are obtained in the $La_{1.8}Sr_{0.2}Cu_{1-y}Zn_yO_4$ series. The $(x = 0.15, y = 0.01)$ sample exhibits weak magnetic order below 5 K. This weak magnetic order is manifested as an increase of $\sigma(T)$ below 5 K and was confirmed by ZF μSR measurements. ZF-μSR on the $La_{1.8}Sr_{0.2}Cu_{0.99}Zn_{0.01}O_4$ and $YBa_2(Cu_{0.99}Zn_{0.01})_3O_{6.63}$ samples showed no indication of magnetic order down to 2.5 K. The absence of magnetic order in the $YBa_2Cu_3O_{6.63}$ system means that the localized moments seen by Mahajan *et al.* affect only a very small fraction of the muon sites, which is consistent with localized moments.

Figure 7.2 shows a "Uemura" plot of T_C versus $\sigma(T \rightarrow 0)$. In terms of this plot, Zn doping has contrasting (but possibly related) effects on the underdoped and overdoped cuprates. Phenomenologically, underdoped cuprates tend to become *more*

Nachumi et al. Figure 1

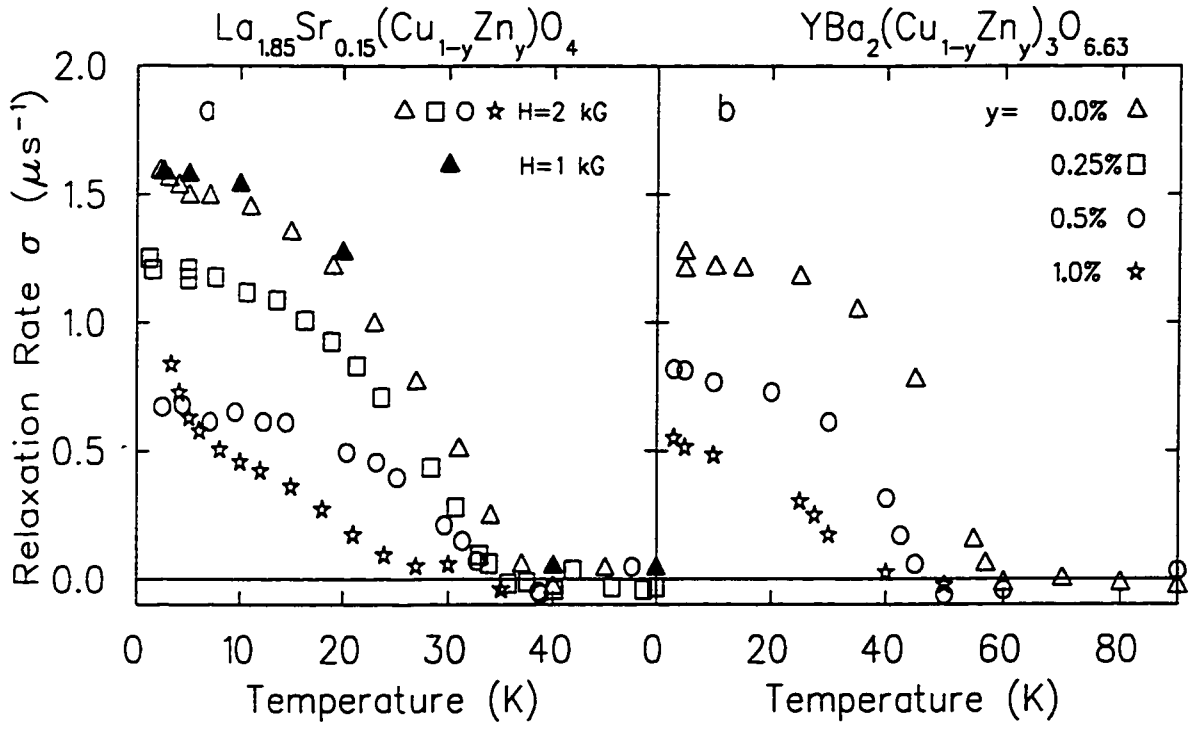

Figure 7.1 The results of Gaussian fits to the data as a function of temperature for $La_{1.85}Sr_{0.15}Cu_{1-y}Zn_yO_4$ and $YBa_2(Cu_{1-y}Zn_y)_3O_{6.63}$.

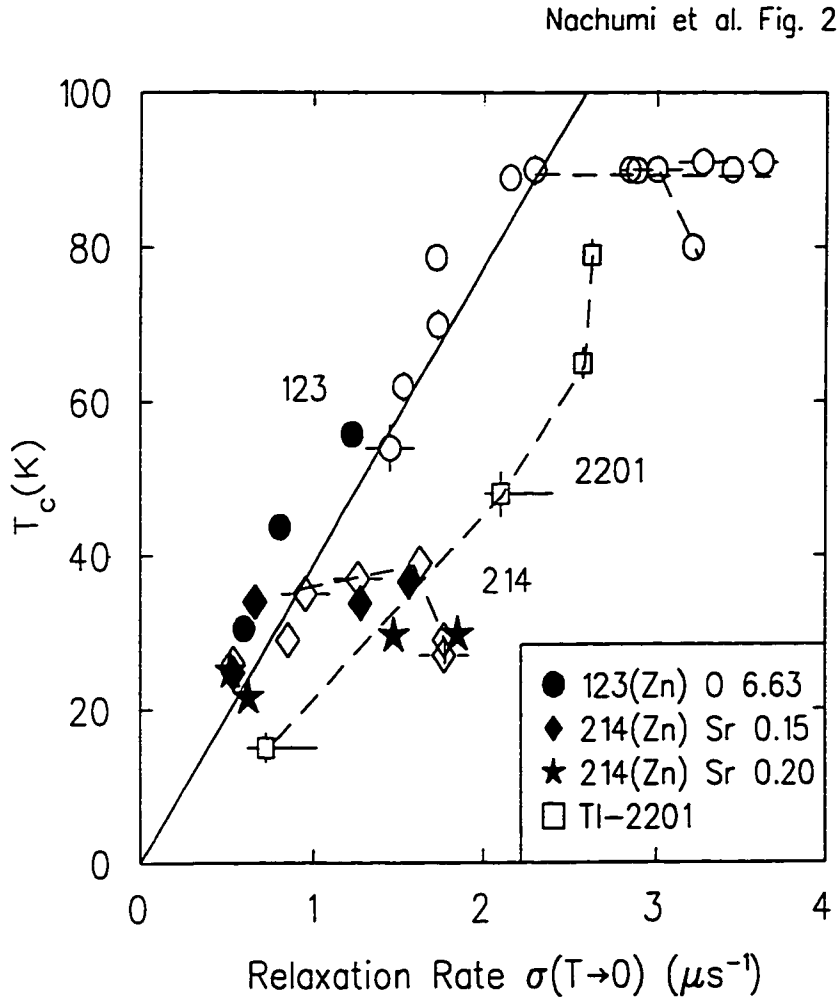

Figure 7.2 The results of Gaussian fits to the data as a function of temperature for $La_{1.85}Sr_{0.15}Cu_{1-y}Zn_yO_4$ and $YBa_2(Cu_{1-y}Zn_y)_3O_{6.63}$, as plotted on a Uemura diagram.

underdoped. moving back down the Uemura line (in the case of $YBa_2(Cu_{1-y}Zn_y)_3O_{6.63}$) or showing the beginnings of magnetic order (in the case of $La_{1.85}Sr_{0.15}Cu_{1-y}Zn_yO_4$). This effect is shown by ZF-μSR measurements in Fig. 7.3.

On the other hand, the overdoped series follows a trajectory which resembles those of extremely overdoped cuprates. For $La_{1.8}Sr_{0.2}Cu_{1-y}Zn_yO_4$, T_C and $\sigma(T \to 0)$ decrease, such that the points in the Uemura plot return toward the universal line, similar to the effect seen in overdoped Tl-2201 cuprate[21] and with no reemergent magnetic order. ZF measurements on $La_{1.8}Sr_{0.2}Cu_{1-y}Zn_yO_4$ with $y \sim 0.03$ (shown in Fig. 7.4 also confirm that even when superconductivity is entirely suppressed by Zn substitution. the $La_{1.8}Sr_{0.2}Cu_{1-y}Zn_yO_4$ system shows no magnetic order. This is not to imply that Zn doping makes an overdoped compound a better metal in the sense that adding normal carriers might. If Zn substitutions break pairs or otherwise disrupt the superconducting state, then perhaps actual overdoping spontaneously disrupts the superconducting state in a similar way.

7.4 Behavior of n_s/m^*: the Swiss Cheese Model

We have modeled the way in which the relaxation rate is reduced[74], as a *depletion of the superconducting condensate*, rather than as a scattering correction in the manner described in chapter 2. In terms of the Pippard form for the supercurrent response (chapter 2) the condensate depletion approach treats the effective coherence length

$$\xi_e = \xi_{ab} l/(\xi_{ab} + l)$$

as a constant and ignores both possible changes in ξ and the effects of l.

Assume the same angular averaging for each of the ceramic specimens, and take

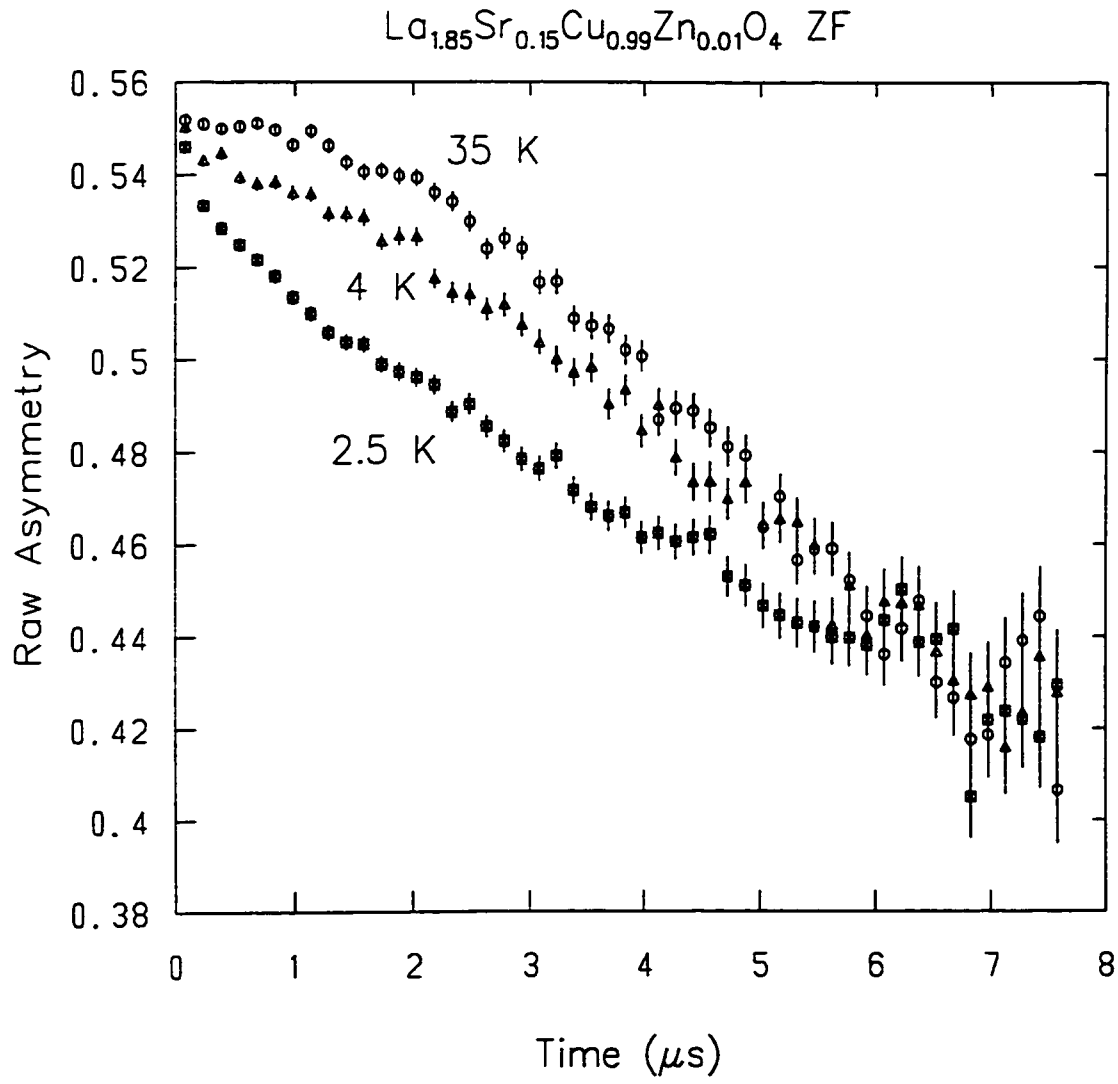

Figure 7.3 ZF spectra on the $La_{1.85}Sr_{0.15}Cu_{0.99}Zn_{0.01}O_4$ showing incipient magnetic order at low temperatures.

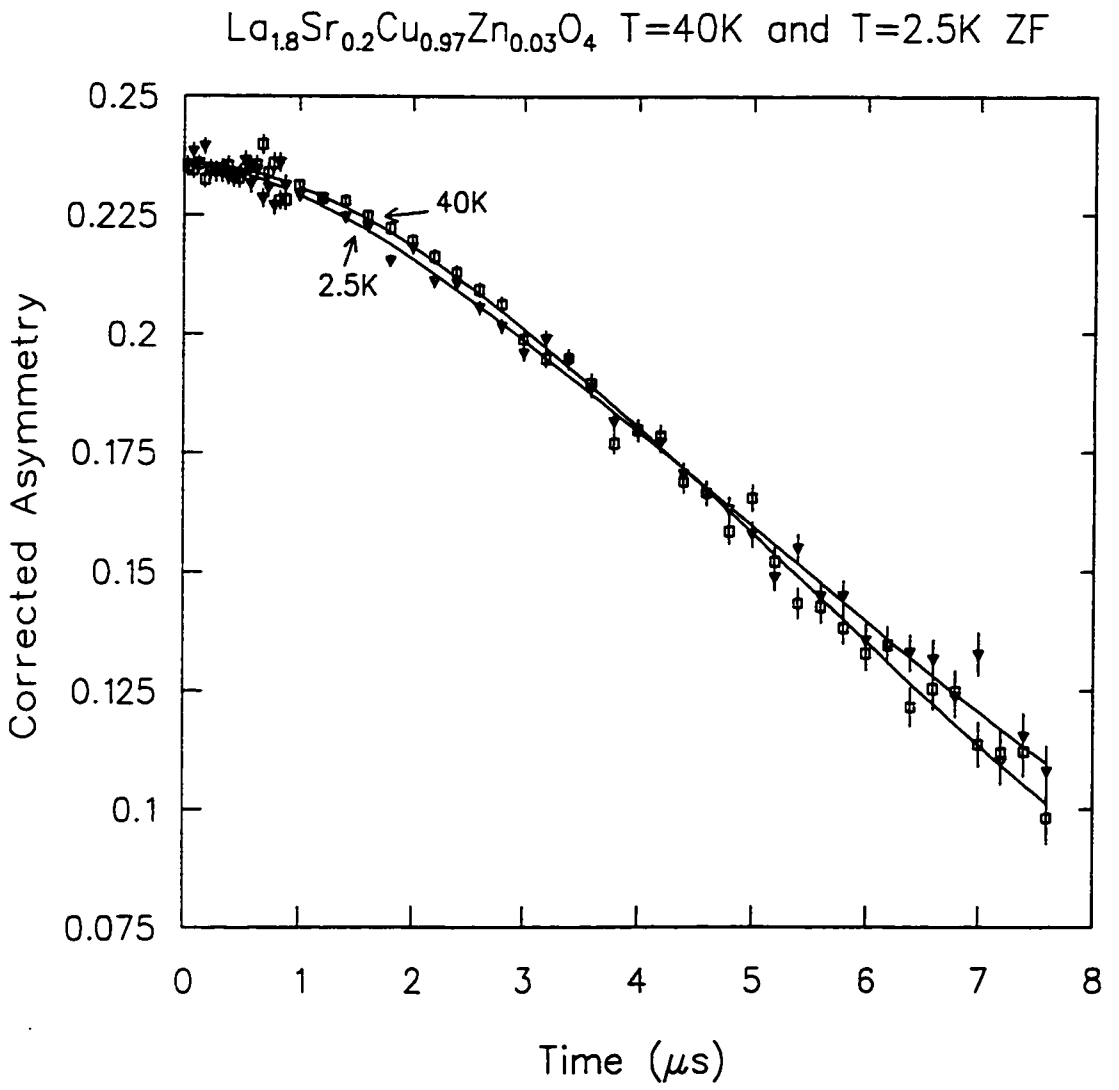

Figure 7.4 ZF spectra of $La_{1.8}Sr_{0.2}Cu_{0.97}Zn_{0.03}O_4$, showing *no* incipient magnetic order.

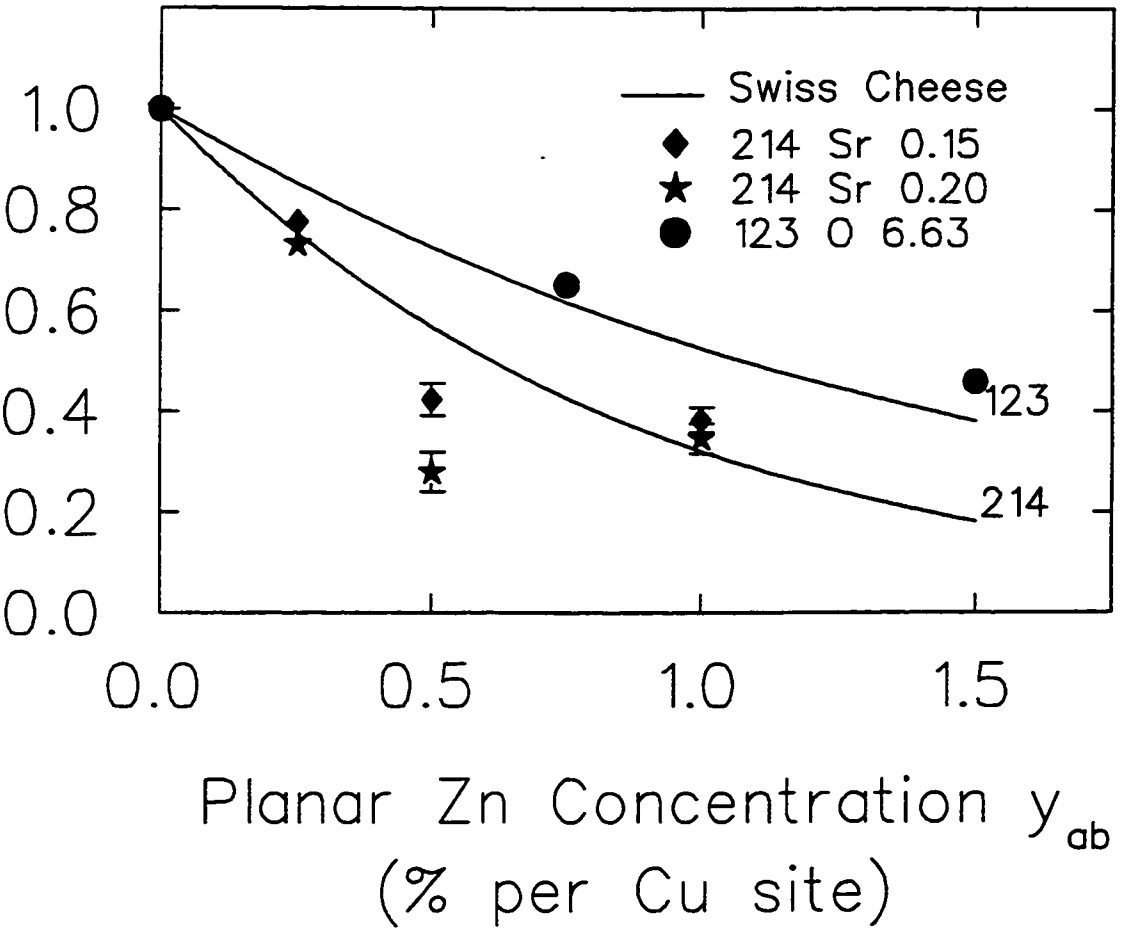

Figure 7.5 $\sigma(T \to 0)(y_{ab})$ normalized by $\sigma(T \to 0)(0)$ from the Gaussian fits.

the ratio of the low-temperature values σ_0 as a function of Zn concentration indicates how the relaxation rate is changed by the Zn substitution. Figure 7.5 shows the behavior of n_s/m^* normalized by the values for the Zn-free samples: $\sigma(T \to 0)(y_{ab})/\sigma(T \to 0)(0)$. Here y_{ab} represents the Zn concentration per planar Cu site. Since $YBa_2(Cu_{1-y}Zn_y)_3O_{6.63}$ also has one chain Cu site per formula unit, y_{ab} for this material is 1.5 times the Zn concentration per formula unit.

Consider a local suppression of the superconducting wavefunction Δ, in which the

CuO_2 plane is perforated with normal regions–like a Swiss cheese. Our Swiss cheese model assumes that each Zn destroys the SC state within a planar coherence length ξ_{ab} of itself, with the rest of the superfluid unaffected. Then, on the lengthscale of λ, this will appear as a reduction in the condensate density n_s. The expected reduction in the measured n_s/m^* is then

$$n_s(y_{ab})n_s(0) = \Pi_{i=1}^{y_{ab}V_{plane}}[1 - \beta/(V_{plane} - ia^2)],$$

where $\beta \approx \pi\xi_{ab}^2/a^2$ is the number of lattice sites where the superconductivity is suppressed, a is the $a-$ or $b-$ axis lattice constant, and V_{plane} is the number of lattice sites in a plane. This result is approximately exponential, and redudces to $e^{(-\beta y_{ab})}$ if the site-occupation by the Zn ions is ignored. The Swiss cheese prediction is shown by the solid curves in Fig. 7.5. At first, n_s decreases linearly with y_{ab}. As the areas from successive Zn substitutions overlap, the reduction saturates.

It is a simple matter to go the other way, and ascribe the reduction in the measured $\sigma(T \to 0)$ to the effect of a reduced mean-free path. In a model where the mean free path effect dominates, the reduced $\sigma(T \to 0)$ is fit to $1/(1 + \xi_{ab}/l)$ where l is determined by y_{ab} and ξ_{ab} is a fitting parameter for each point. In this case, the values of ξ_{ab} range from about 63 Åfor $La_{1.85}Sr_{0.15}Cu_{1-y}Zn_yO_4$, to 120 Åfor $YBa_2(Cu_{1-y}Zn_y)_3O_{6.63}$, and there is a strong correlation between l and ξ_{ab}. 120Åfor $YBa_2(Cu_{1-y}Zn_y)_3O_{6.63}$ is close to the value which Sonier *et al.* estimate as the radius estimated by Sonier *et al.*[18]. However, if we take this fit at face value it suggests that ξ_{ab} for the Y-based cuprate is at least twice as large as that for the La-based cuprate, which seems incorrect from the ratio of the T_C's.

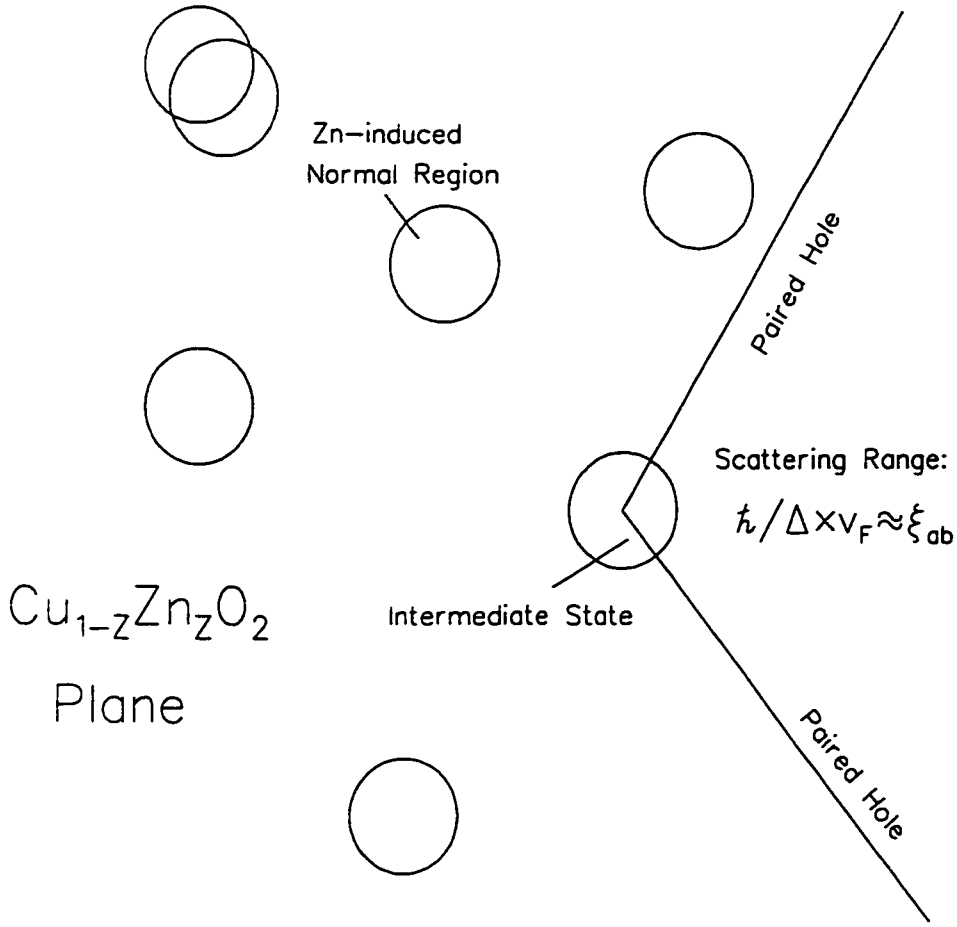

Figure 7.6 Schematic of the heuristic scattering picture.

7.5 A Quick-and-Dirty Pair-Breaking Picture

A simple interpretation of these results derives from a scattering picture of the reduction in n_s. The picture is summarized in Fig. 7.6. Suppose that Zn acts as a resonant scatterer at the Fermi level. The resonance implies a quasilocalized state near the Zn. From the uncertainty relationship $\delta E \delta t \sim \hbar$[7], the distance to which a broken Cooper pair will survive is approximately $\hbar/\Delta v_F \approx \xi_{ab}$, where v_F is the Fermi

velocity and Δ is the energy gap.

The s-wave resonant scattering cross section in 2 dimensions for $k = k_F$ is $\Sigma_s = 2/(\pi k_F)$. The assumption that every scattered pair is broken implies the rate equation at equilibrium:

$$n_s(y_{ab}) y_{ab} v_F \Sigma_s = (n_s(0) - n_s(y_{ab}))/\tau_l,$$

where $n_s(0)$ is the equilibrium number density $\tau_l \sim \hbar/\Delta$. In fact, the proper lifetime will be some average of this value over the Fermi surface; one may instead fit for a value of τ from the data. Solving for $n_s(y_{ab})/n_s(0)$ gives:

$$n_s(y_{ab})/n_s(0) = 1/(1 + \Sigma_s v_F y_{ab} \tau_l).$$

This expression becomes useful when the observed reduction in T_C is compared to that expected from pair-breaking scattering in the Abrikosov-Gor'kov formalism discussed below.

7.6 Localization Picture

The presence of the stripe instability in the cuprates suggests another picture based on the local pinning of the fluctuating charge stripes which have been inferred in the $La_{2-x}Sr_xCu_{1-y}Zn_yO_4$ system. This scheme is illustrated in Fig. 7.7. The pinning in this picture is due to the same effects which may be driving the holes to phase separate: a hole located next to a Zn^{++} ion must break fewer AF bonds, because the Zn has no moment[64]. The induced moments near the Zn^{++} site may be ascribed to the associated magnetic region of the (locally static) stripe phase.

Instead of reducing n_s via scattering, such a pinning would locally increase m^*. The effect would be indistinguishable from the scattering picture at most y_{ab}, except

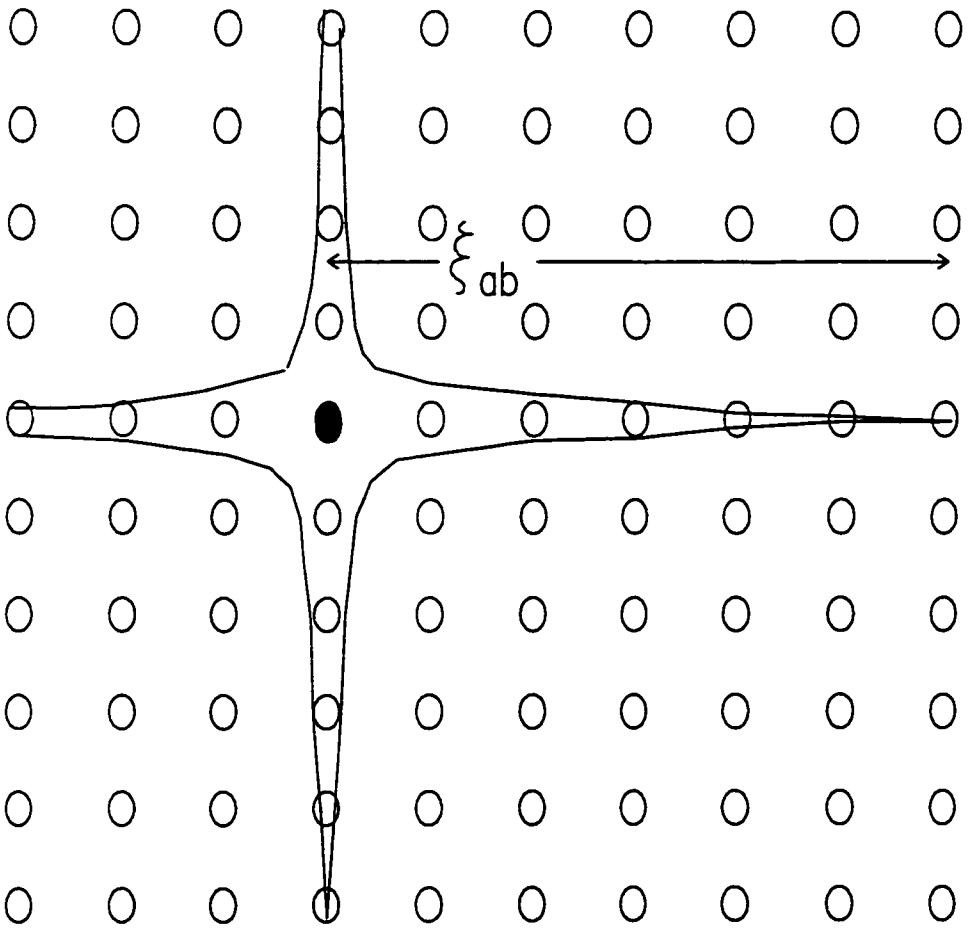

Figure 7.7 Schematic of the stripe-localization idea.

when the average stripe spacing is commensurate with the average linear impurity spacing. Interestingly, the reduction of n_s/m^* is enhanced for both $La_{2-x}Sr_xCu_{1-y}Zn_yO_4$ samples at $y_{ab} = 0.005$, where the linear impurity spacing $1/\sqrt{y_{ab}} \sim 14a$. This distance corresponds to between three and four times the spacing between the charge stripes. Hence the enhanced suppression of n_S/m^* at $y_{ab} = 0.005$ for both $x = 0.15$ and $x = 0.20$ yields some support for this pinning scenario.

7.7 $T_C(y_{ab})$

The foremost mystery of the Zn-substitution is its strong effect on T_C. Figure7.8 shows T_C as a function of y_{ab}, along with some predictions from the Abrikosov-Gorkov (AG)-type scattering theory for d-wave superconductors [75]. AG theory has been extended to the d-wave case for weak coupling ($\Delta = 0.88 k_B T_C(0)$)[76]. The extended theory yields an implicit equation for T_C as a function of the impurity scattering rate τ:

$$\ln(T_C(y_{ab})/T_C(0)) = \psi(1/2 + \alpha T_C(0)/(2\pi T_C(y_{ab}))) - \psi(1/2),$$

where ψ is the digamma function. The pair-breaking parameter $\alpha = 1/(\tau T_C(0))$, with τ now the scattering rate. Note that the quantity $\tau T_C(0)$ should be the inverse of $\Sigma_s v_F y_{ab} \tau_l$ in the simplified scattering picture presented above, e. g. the scattering rate multiplied by the lifetime of the scattered state. For consistency, $\tau T_C(0)$ should be determined from the n_s value at each value of y_{ab}. All of the samples measured clearly fall in the linear regime, for which

$$T_C(y_{ab})/T_C(0) \simeq 1 - \pi/4 \times \alpha.$$

Estimating $\Sigma_i v_F y_{ab} \tau_l$ from the measured reduction in σ and putting it into the linearized equation yields the estimates shown as the closed symbols in Fig. 7.8.

The "quick-and-dirty" theory predicts substantially lower $T_C(y_{ab})$ than those which are observed. Moreover, using the full theory with the theoretical impurity scattering rate (calculated from the measured density of states at the Fermi level [70, 71, 72]), and the bare value $\Delta(0) = 0.88 k_B T_C(0)$ also tends to underestimate $T_C(y_{ab})$, at least for the $La_{2-x}Sr_xCu_{1-y}Zn_yO_4$ series. Recently Tallon *et al.*[77] have attempted to modify the theory by using the stronger-coupling $\Delta \sim 1.65 k_B T_C(0)$, with better results in the small-y_{ab} (linear) regime. However, at higher values of y_{ab}, the expected downward curvature in $T_C(y_{ab})$ is absent. Furthermore, the simple substitution of the strong-coupling Δ in an equation derived within a weak-coupling approximation may not be justified because it ignores the possible renormalization of the scattering rate due to strong interparticle interactions [7, 78].

Another objection to the use of AG formalism, raised by Franz *et al.*[79], derives from the fact that Δ in the gap equation is taken as the average value: spatial variations of the order parameter are neglected. In materials with $\xi_{ab} < 1/\sqrt{(y_{ab})}$ at $T_C(y_{ab})$, such an averaging is inconsistent. In a direct lattice calculation which accounts for spatial variations of Δ, Franz *et al.* find that $T_C(y_{ab})$ is less suppressed. Furthermore, they find that $\Delta(y_{ab})$ and $T_C(y_{ab})$ have different temperature dependences. These results suggest that a correction to the AG formalism should yield a physical picture very similar in spirit to that seen in the Swiss cheese model, in that the superconducting order parameter is locally suppressed near the impurities.

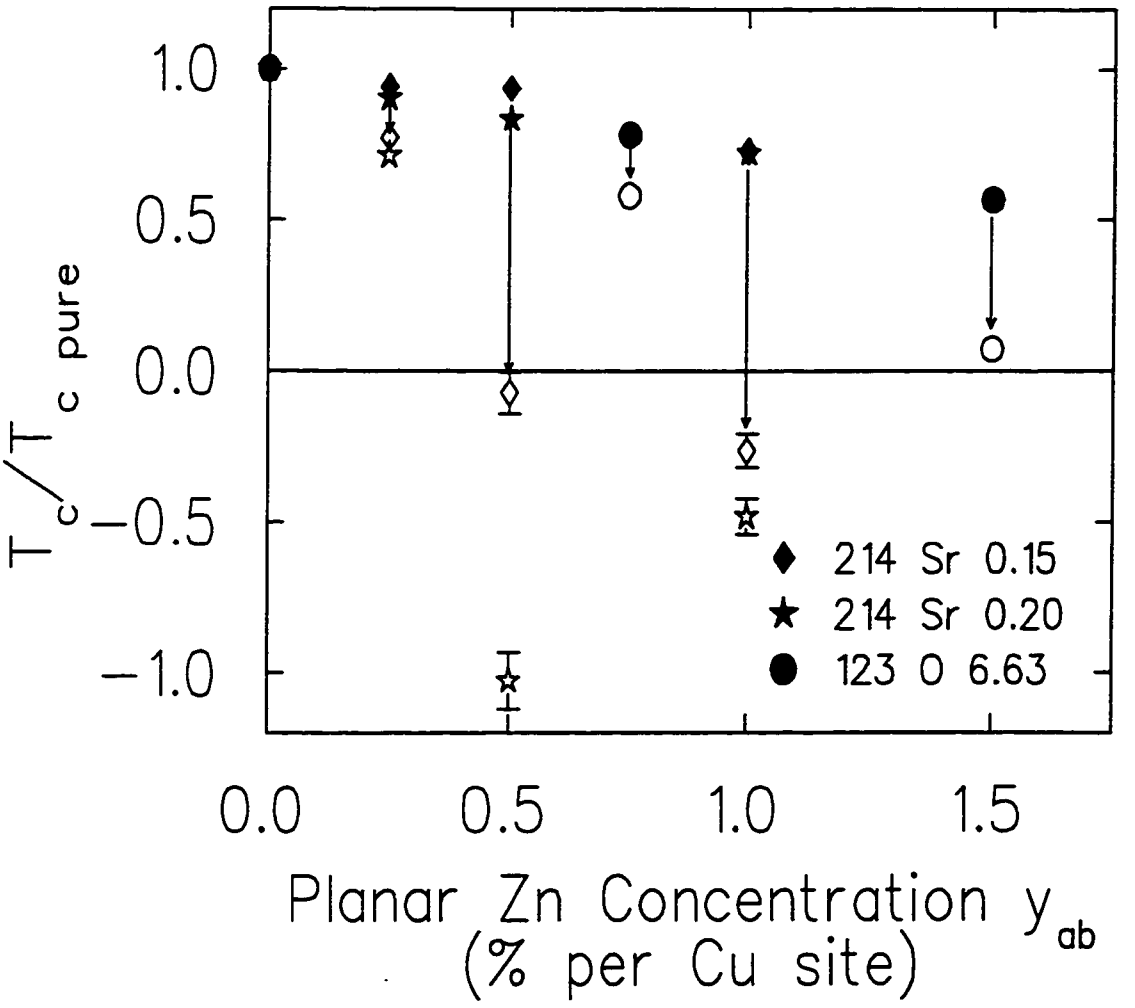

Figure 7.8 $T_C(y_{ab})$ normalized by $T_C(0)$. The closed symbols are the data; the open symbols are the estimate of the linearized AG theory with the parameter α determined from the estimates of $n_s/m^*(y_{ab})$.

7.8 General Conclusions on Zn-Substitution Effects

I have reported here some effects of Zn substitution in ceramic samples of La-based and Y-based cuprates. It has long been known that Zn substitution markedly reduces T_C in these materials. These measurements provided some of the first data on how the superconducting current is suppressed. However the interpretation is somewhat difficult due to the ambiguity in the coherence length for magnetic fields on the order of a few kilogauss.

The behavior of the normalized n_s/m^* and T_C characteristics as functions of y_{ab} suggest that in all of the samples, the superconductivity is suppressed by the same mechanism. However, in terms of the T_C-n_s type of diagram, underdoped and overdoped samples behave rather differently: the underdoped series tend to exhibit magnetic order as the superconductivity is suppressed, while the overdoped series showed no indication of electronic magnetic order even for $T_C \to 0$.

If the coherence length in the cuprates is indeed short even for small applied fields, one may draw some tentative conclusions based on the phenomenological Swiss cheese model for the local reduction in n_s. This model may be consistent with either a scattering model ($n_s \to 0$ locally) or a localization model ($m^* \to \infty$ locally). Within the Swiss cheese model, one finds a further result: the usual AG scattering theory for the suppression of T_C is inconsistent with the framework of the weak coupling theory within which it was derived. This conclusion is supported by more realistic calculations for the suppression of T_C in both the weak coupling and strong coupling regimes.

REFERENCES

[1] J. G. Bednorz and K. A. Muller. *Z. Phys.*, 64:189, 1986.

[2] L. R. Testardi et al. *Solid State Commun.*, 15:1, 1974.

[3] Donald M. Ginsberg. Introduction, history, and overview of high temperature superconductivity. In Donald M. Ginsberg, editor, *Physical Properties of High Temperature Superconductors I.* World Scientific, 1989.

[4] Alexandre M. Zagoskin. *Quantum Theory of Many-Body Systems*, chapter 4. Springer, 1998.

[5] L. N. Cooper. *Phys. Rev.*, 104:1189, 1956.

[6] P. G. DeGennes. *Superconductivity of Metals and Alloys*, chapter 5. Frontiers in Physics. W. A. Benjamin, Inc., 1966.

[7] Oleg Tchernyshyov. Private communication. 1997.

[8] P. G. DeGennes. *Superconductivity of Metals and Alloys*, chapter 4. Frontiers in Physics. W. A. Benjamin, Inc., 1966.

[9] J. M. Ziman. *Theory of Solids, Second Edition*, chapter 11. Cambridge University Press, 1972.

[10] R. P. Feynman. *Statistical Mechanics*, chapter 10. Frontiers in Physics. Addison-Wesley, 1972.

[11] D. R. Tilley and J. Tilley. *Superfluidity and Superconductivity*, chapter 6. Graduate Student Series in Physics. Institute of Physics Publishing, 1990.

[12] J. Bardeen. *Nobel Lecture*, pages 7–10, 1972.

[13] B. G. Batlogg et al. *Phys. Rev. Lett.*, 59:912, 1988.

[14] T. A. Faltjens et al. *Phys. Rev. Lett.*, 59:915, 1988.

[15] K. J. Leory et. al. *Phys. Rev. Lett.*, 59:1236, 1988.

[16] W. L. McMillan. *Phys. Rev.*, 167:331, 1968.

[17] D. A. Bonn et al. *Phys. Rev. B*. 50:4051. 1996.

[18] J. E. Sonier et al. *Phys. Rev Lett.*. 79:2875, 1997.

[19] Y. J. Uemura et al. *Phys. Rev. Lett.*, 62:2317, 1989.

[20] Y. J. Uemura et al. *Phys. Rev. Lett.*, 66:2665, 1991.

[21] Y. J. Uemura. *Nature (London)*, 364:605, 1993.

[22] AWAITING A TRANSLATION. *JSPS*, 1998.

[23] Y. J. Uemura. In *Proceedings of the Workshop on Polarons and Bipolarons in High-Tc Superconductors and Related Materials, 1994*, pages 453–60, Cambridge, United Kingdon, 1995. Cambridge University Press, Cambridge.

[24] Y. J. Uemura. In *Proceedings of the CCAST Symposium on High-Tc Superconductivity and the C60 Family, 1994*, pages 113–42, Beijing, 1995. Gordon and Breach, New York.

[25] Oleg Tchernyshyov. *Phys. Rev. B*. 1998.

[26] J. E. Sonier et al. *Phys. Rev. Lett.*. 79:1742, 1997.

[27] W. Barford and J. M. F. Gunn. *Physica C*, 156:515–22, 1988.

[28] D. R. Harshman et al. *Phys. Rev. Lett.*, 66:3313, 1991.

[29] P. G. DeGennes. *Superconductivity of Metals and Alloys*, chapter 1. Frontiers in Physics. W. A. Benjamin, Inc., 1966.

[30] E. H. Brandt. *Phys. Rev. B*, 37:2349, 1988.

[31] G. M. Luke. Private communication. 1998.

[32] J. H. Brewer. Private communication. 1998.

[33] Weidong Wu. *PhD Thesis*. PhD thesis, Columbia University, 1994.

[34] J. D. Axe. *Phys. Rev. Lett.*, 62:2751, 1989.

[35] G. M. Luke et al. *Physica C*, C185-9:185, 1991.

[36] K. Kumagai et al. *Hyp. Int.*, 86:473, 1994.

[37] G. M. Luke at al. *Hyp. Int.*, 105:113, 1997.

[38] F. Borsa et al. *Phys. Rev. B*, 52:7334, 1995.

[39] T. Nagano et al. *Phys. Rev. B*, 48:9689, 1993.

[40] M. K. Crawford et al. *Phys. Rev. B*, 44:7749, 1991.

[41] J. M. Tranquada et al. *Nature (London)*, 375:338, 1995.

[42] J. M. Tranquada et al. *Phys. Rev. B*, 54:7489, 1996.

[43] Y. Nakamura and S. Uchida. *Phys. Rev. B*, 46:5841, 1992.

[44] B. Büchner et al. *Phys. Rev. Lett.*, 73:1841, 1994.

[45] J. M. Tranquada. *Phys. Rev. Lett.*, 73:1003, 1994.

[46] M. v. Zimmerman et al. Hard-x-ray diffraction study of charge stripe order in la $_{1.48}$ nd $_{0.4}$ sr $_{0.12}$ cuo $_{4}$. Accepted for publication in Europhys. Lett.

[47] K. Levin et al. *Physica C*, C 235-240:71, 1994.

[48] S. Kivelson V. J. Emery and O. Zachar. cond-mat/9610094. LANL preprint archive, 1996.

[49] K. M. Kojima. *Phys. Rev. B*, 78:1787, 1997.

[50] A. Lappas et al. *Hyp. Int.*, 105:101, 1997.

[51] J. M. Tranquada et al. *Phys. Rev. Lett.*, 78:338, 1997.

[52] B. Hitti et al. *Hyp. Int.*, 63:287, 1990.

[53] J. M. Tranquada. Private communication. 1998.

[54] Y. J. Uemura et al. *Physica C*, 153-155:769, 1988.

[55] K. Yamada et al. *Phys. Rev. B*, 57:6165, 1998.

[56] Daniel Hone and A. H. Castro-Neto. *cond-mat/9701042*, 1997.

[57] A. H. Castro-Neto and Daniel Hone. *Phys. Rev. Lett*, 76:2165, 1996.

[58] K. M. Kojima et al. *Phys. Rev. Lett.*, 74:2812, 1995.

[59] Ian Affleck et al. *J. Phys. A*, 27:7313, 1994.

[60] D. Vaknin et al. *Phys. Rev. B*, 41:1926, 1990.

[61] A. Keren et al. *Phys. Rev. B*, 48:12926, 1993.

[62] S. Shamoto. *Phys. Rev. B*, 48:13817, 1993.

[63] J. E. Ostenson et al. *Phys. Rev. B*, 56:2820, 1997.

[64] A. H. Castro-Neto. From his talk in los angeles, 1998.

[65] Gang Xiao et al. *Phys. Rev. B*, 42:8752, 1990.

[66] H. Alloul et al. *Phys. Rev. Lett.*, 67:3140, 1991.

[67] A. V. Mahajan et al. *Phys. Rev. Lett.*, 72:3100, 1994.

[68] Y. Fukuzumi. *Phys. Rev. Lett.*, 76:684, 1996.

[69] W. N. Hardy et. al. *Phys. Rev. Lett.*, 70:3999, 1993.

[70] J. W. Loram et al. *Phys. Rev. B*, 71:1740, 1993.

[71] J. W. Loram. *Physica C*, 235C-240C:134, 1994.

[72] J. W. Loram et al. In *Proceedings of the 10th Annual HTSC Conference, 1996*, Houston, TX, 1997.

[73] Y. Ando et al. *Phys. Rev. Lett.*, 75:4662, 1995.

[74] B. Nachumi et al. *Phys. Rev. Lett.*, 77:5421, 1996.

[75] P. G. DeGennes. *Superconductivity of Metals and Alloys*, chapter 8. Frontiers in Physics. W. A. Benjamin, Inc., 1966.

[76] Y. Sun and K. Maki. *Phys. Rev. B*, 51:6059, 1995.

[77] J. L. Tallon et al. *Phys. Rev. Lett.*, 1998.

[78] B. Nachumi et al. *Phys. Rev. Lett.*, 1998.

[79] M. Franz et al. *Phys. Rev. B*, 54:R6897, 1996.

IMAGE EVALUATION TEST TARGET (QA-3)

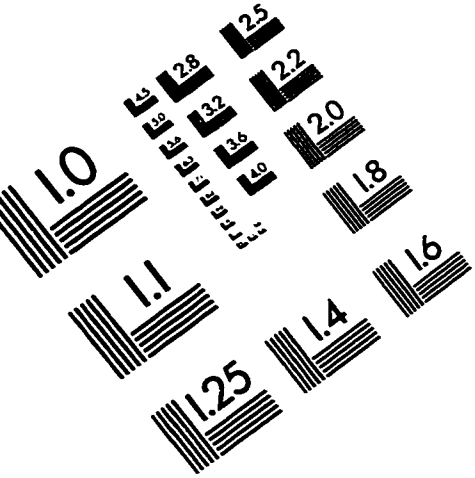

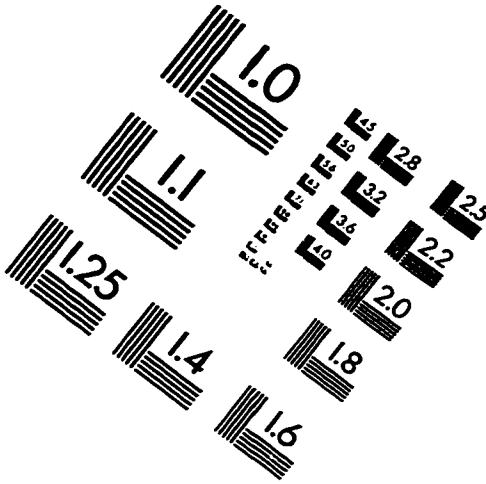

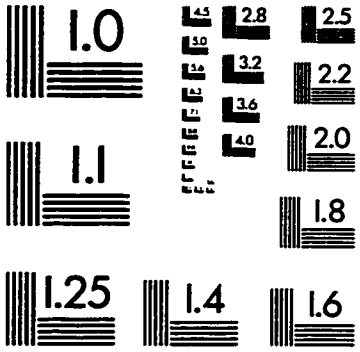

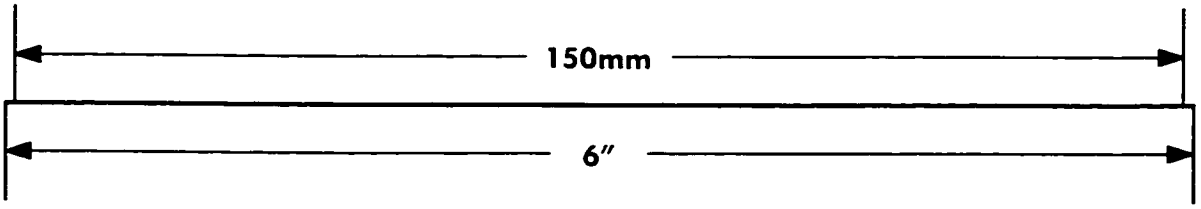

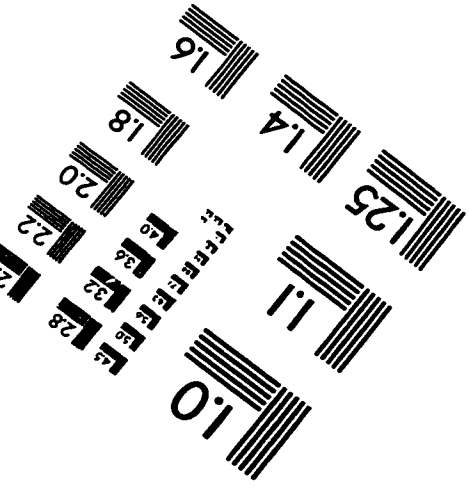

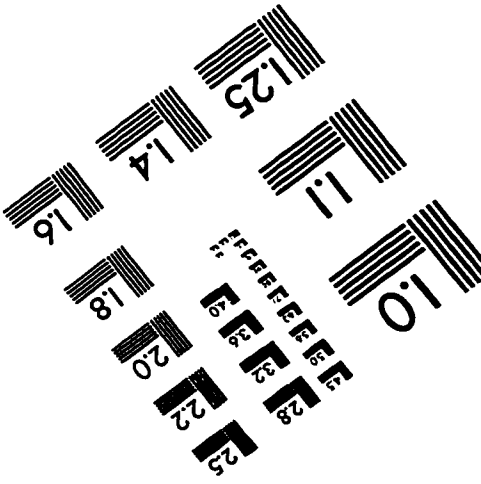

APPLIED IMAGE, Inc
1653 East Main Street
Rochester, NY 14609 USA
Phone: 716/482-0300
Fax: 716/288-5989